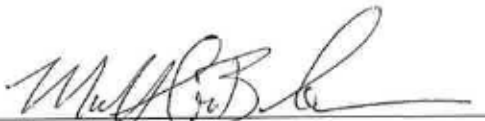


APPROVAL SHEET

Title of Thesis: Using Detailed Terrain Analysis to Understand Spatiotemporal
Patterns of Floodplain Hydraulics and Sediment Deposition

Name of Candidate: Zachary John Clifton
Master of Science, 2018

Thesis and Abstract Approved:



Dr. Matthew E. Baker
Professor
Geography and Environmental Systems

Date Approved: 11-30-18

ABSTRACT

Title of Document: USING DETAILED TERRAIN ANALYSIS
TO UNDERSTAND SPATIOTEMPORAL
PATTERNS OF FLOODPLAIN
HYDRAULICS AND SEDIMENT
DEPOSITON

Zachary John Clifton, Master of Science, 2018

Directed By: Dr. Matthew E. Baker
Geography and Environmental Systems

Sediment transport in rivers plays multiple key roles within every watershed. Fine sediments transported by rivers carry with them vital nutrients that are essential to riverine and estuarine life, when not in excess. Floodplain storage of these same fine sediments is of interest to parties attempting to mitigate downstream sediment and nutrient pollution. However, historic methodological and technological limitations have limited fine-scale studies of floodplain storage. This exploratory study, utilizing modern multi-temporal high-resolution topography and advanced geospatial analysis tools, sought to overcome these limitations and comprehensively assess floodplain sediment dynamics and the conditions governing them. Our findings suggest that in addition to geometric measures, flow conditions across a floodplain during the falling limb are strong predictors of floodplain-scale sedimentology. Further results suggest modern high-resolution topography is capable of adequately modeling fine-scale

sediment dynamics from single storms, accurately characterizing low-relief landforms, and providing detailed terrains for hydraulic models.

USING DETAILED TERRAIN ANALYSIS TO UNDERSTAND
SPATIOTEMPORAL PATTERNS OF FLOODPLAIN HYDRAULICS AND
SEDIMENT DEPOSITON

By

Zachary John Clifton

Thesis submitted to the Faculty of the Graduate School of the
University of Maryland, Baltimore County, in partial fulfillment
of the requirements for the degree of
Master of Science
2018

© Copyright by
Zachary John Clifton
2018

Dedication

To my grandmother Mimi.

Acknowledgements

This thesis would not have been accomplished without the help of my family, friends, and the greater UMBC community.

For the number of avenues this thesis ended up taking, I was extremely lucky to have arranged a committee as multitalented as mine. Special thanks to Matt Baker, Andy Miller, and Matt Fagan for all the support, for answering every oddball question I could throw at them, and for pulling me out of the weeds every time I got lost in them. Thanks also go to Robin Schmidbauer for her administrative assistance, and to Stu Schwartz and Brennan Smith of CUERE for all their training. Further thanks are due to my assistant Donovan Smith; lab and fieldwork were made much more enjoyable by your presence.

My family supported me all throughout my nearly eight years at UMBC, especially during graduate school. Thank you for giving me a warm place to stay and for all the love and support along the way.

If I were to thank all my friends here it'd take up more pages than my thesis itself. But in short, thanks are due to Sup Club, Namco, and the Smoke-Free community at large for all the laughs along the way. Final thanks are due to Baltimore's chapter of the Peoples Climate Movement for allowing me an avenue to help my local community in my spare time; I'm very grateful for all you've taught me.

Table of Contents

Dedication	ii
Acknowledgements	iii
Table of Contents	iv
List of Tables	vi
List of Figures	vii
Chapter 1: Introduction	1
Section 1: Overview	1
Section 2: Characterizing Sediment Deposition, Floodplain Topography, and Hydraulic Processes	3
<i>Subsection 1: Floodplain Sediment Deposition and Erosion</i>	5
<i>Subsection 2: Macro- and Micro-Topography</i>	9
<i>Subsection 3: Flood Hydraulics</i>	11
Section 3: Problem Statement and Approach	13
Section 4: Study Site	15
Chapter 2: Methods	23
Section 1: Quantifying and Mapping Post-Flooding Sediment Accretion	23
Section 2: Characterizing Floodplain Landforms	26
Section 3: Modeling Representative Flow Conditions on the Floodplain	28
Section 4: Quantifying Sediment Characteristics for the Study Floodplain	37
Section 5: Assessing the Relative Importance of Hydrogeomorphic, Topographic, and Geometric Conditions in Explaining Spatial Patterns of Floodplain Sediment Texture	44
Chapter 3: Results	52
Section 1: Quantifying and Mapping Post-Flooding Sediment Accretion	52
Section 2: Characterizing Floodplain Landforms	59
Section 3 Modeling Representative Flow Conditions on the Floodplain	61
<i>Subsection 1: Backfilling Conceptual Period</i>	62
<i>Subsection 2: Overbanking and Splaying Conceptual Periods</i>	64
<i>Subsection 3: Peak Flow Conceptual Period</i>	67
<i>Subsection 4: Earlier and Later Drainage Conceptual Periods</i>	70
Section 4: Quantifying Sediment Characteristics for the Study Floodplain	73
Section 5: Assessing the Relative Importance of Hydrogeomorphic, Topographic, and Geometric Conditions in Explaining Spatial Patterns of Floodplain Sediment Texture	80
<i>Subsection 1: Guiding Question #1- All Explanatory Variables</i>	81
<i>Subsection 2: Guiding Question #2 – Distance-related Explanatory Variables</i>	85
<i>Subsection 3: Guiding Question #3 – Flow-related Explanatory Variables</i>	88
<i>Subsection 4: Comparing Univariate and Multivariate Regression Tree Analyses</i>	91
Chapter 4: Discussion	94
Section 1: Quantifying and Mapping Post-Flooding Sediment Accretion	94
Section 2: Characterizing Floodplain Landforms	99
Section 3: Modeling Representative Flow Conditions on the Floodplain	101

Section 4: Assessing the Relative Importance of Hydrogeomorphic, Topographic, and Geometric Conditions in Explaining Spatial Patterns of Floodplain Sediment Texture	105
Chapter 5: Conclusions and Synthesis	109
Appendices	111
Bibliography	117

List of Tables

Chapter 2: Methodologies

Table 2.1: Various metadata associated with aerial LiDAR datasets utilized.

Table 2.2: Full list of explanatory variables, associated units, and conditions represented.

Table 2.3: Full list of regression tree designs and included explanatory variables.

Chapter 3: Results

Table 3.1: Full list of explanatory variables, their abbreviations, and conditions represented.

Table 3.2: Percent variation of floodplain sediment texture explained by each multivariate and univariate regression tree analysis.

Appendices

Table 5.1: HEC-RAS model times when flow-related variables were exported for use in regression analyses.

Table 5.2: Percent variation of floodplain sediment texture explained by exploratory univariate analyses of numeric explanatory variables.

List of Figures

Chapter 1: Introduction

Figure 1.1: Hillshade of the Lower Patapsco River floodplain, with study area. (inset): spatial location of study area relative to Maryland.

Figure 1.2: Study area depicted, with areas of presumed local effects highlighted.

Chapter 2: Methodologies

Figure 2.1: Extent of floodplain terrain imported in the HEC-RAS model.

Figure 2.2: Manning's N roughness coefficient values assigned to distinct regions of the Lower Patapsco floodplain according to vegetation conditions.

Figure 2.3: Sediment core sampling plan.

Chapter 3: Results

Figure 3.1: DEM of Difference generated by comparison to elevation error estimation from global reference points across county extent (the “regional” minLOD).

Figure 3.2: Intermediate DEM of Difference between localized and regional estimates of the minimum level of detection threshold ($\text{minLOD} = 0.2\text{m}$).

Figure 3.3: Intermediate DEM of Difference between localized and regional estimates of the minimum level of detection threshold ($\text{minLOD} = 0.1\text{m}$).

Figure 3.4: DEM of Difference generated by comparison to elevation error estimation from reference points within local extent (the “localized” minLOD).

Figure 3.5: Landform characterization results from filtered terrain.

Figures 3.6-3.11: Various flow velocities as simulated within the hydraulic flow model, in chronological order.

Figure 3.12: Sediment texture gradient across a floodplain transect depicted for the three sediment texture size classes.

Figure 3.13: Ternary diagram of floodplain sediment texture across sample sites.

Figure 3.14: Interpolation results of particle size distribution for percent clay.

Figure 3.15: Interpolation results of particle size distribution for percent silt.

Figure 3.16: Interpolation results of particle size distribution for percent sand.

Figure 3.17: Multivariate regression tree series generated from the all-inclusive explanatory variable set.

Figure 3.18: Sand variable importance plot generated from a *randomforest* regression tree algorithm.

Figure 3.19: Multivariate regression trees generated from the explanatory variable set that excluded distance-related variables.

Figure 3.20: Multivariate regression trees generated from the explanatory variable set that excluded flow-related variables.

Chapter 4: Discussion

Figure 4.1: Univariate regression tree predicting sand proportions in sediment samples across the study floodplain, generated from the explanatory variable set of only sediment accretion rates.

Figure 4.2: Sand variable importance plot generated from a *randomforest* regression tree algorithm.

Figure 4.3: Intermediate DEM of Difference between localized and regional estimates of the minimum level of detection threshold ($\text{minLOD} = 0.1\text{m}$).

Figure 4.4: Landform characterization of the upstream section using the “filtered” terrain dataset, highlighting ephemeral drainage networks.

Figure 4.5: Simulated flow velocities during the later conceptual period according to the hydraulic flow model.

Figure 4.6: Multivariate regression tree predicting sand proportions in sediment samples across the study floodplain, generated from the all-inclusive explanatory variable regression tree design set.

Figure 4.7: Ternary diagram of floodplain sediment deposits generated by Marriott (1992).

Figure 4.8: Ternary diagram of floodplain sediment texture across sample sites for this study.

Appendices

Figure 5.1: Correlation matrix of all explanatory variables used in regression analyses.

Figure 5.2: Silt variable importance plot generated from a *randomforest* regression tree algorithm.

Figure 5.3: Clay variable importance plot generated from a *randomforest* regression tree algorithm.

Figure 5.4: Landform characterization results from unfiltered terrain.

List of Illustrations

Chapter 1: Introduction

Image 1.1: Imagery of the Rt.1 culvert.

Image 1.2: Example of sand waveforms on the Lower Patapsco floodplain.

Image 1.3-1.7: Examples of the wide variety of vegetation density and composition found at the study area.

Chapter 2: Methodologies

Image 2.1: Soil sample collection at study area, facilitated by a hand shovel.

Image 2.2: After oven drying, soil samples were ground before particle size analysis.

Image 2.3: Various soil samples mid-particle size analysis.

Image 2.4: Close-up of a 1L volumetric cylinder mid-particle size analysis, with visible particle stratification.

Chapter 1: Introduction

Section 1: Overview

Sediment transport is a key function of nearly every river in every watershed on the planet. Coarse sediments ($>63\mu\text{m}$ in diameter) transported by rivers absorb kinetic energy imparted by flowing waters, preserving channel shape and creating ecologically important bed features when later deposited (Carling, 1987; Knighton, 2014). Similarly, fine sediments ($<63\mu\text{m}$ in diameter) transported by rivers carry with them vital nutrients such as phosphorus, nitrogen, and organic carbon that are essential to riverine, estuarine, and oceanic life (Howarth et al., 1991; Mueller, 1996; Fabricius, 2005). Anthropogenic activities throughout a watershed, however, may affect a river's ability to transport sediments.

Sediment transport is a key function of nearly every river in every watershed on the planet. Coarse sediments ($>63\mu\text{m}$ in diameter) transported by rivers absorb kinetic energy imparted by flowing waters, preserving channel shape and creating ecologically important bed features when later deposited (Carling, 1987; Knighton, 2014). Similarly, fine sediments ($<63\mu\text{m}$ in diameter) transported by rivers carry with them vital nutrients such as phosphorus, nitrogen, and organic carbon that are essential to riverine, estuarine, and oceanic life (Howarth et al., 1991; Mueller, 1996; Fabricius,

2005). Anthropogenic activities throughout a watershed, however, may affect a river's ability to transport sediments.

Anthropogenic activities influence both the amount of sediment produced in a watershed and how well sediments are retained on floodplains, another ecologically important function of rivers. Anthropogenic activities can promote excessive sediment runoff, which can have deleterious ecological effects on downstream water bodies (e.g. estuaries and coastal shelf ecosystems) upon delivery (Layzer, 2002; Gellis et. al., 2009). Further contemporary sediment storage research (e.g., Noe & Hupp, 2005) suggests that anthropogenic land use patterns may limit the hydrologic connectivity between river channels and floodplains. This shift in hydrologic connectivity has the potential to minimize sediment retention on floodplains, along with nutrients attached to fine sediment. Additional research suggests that mean lag times for sediments retained by floodplains during storm events range from decades to millennium (Pizzuto et al., 2014). Given such long lag times and the importance of both sediment transport and retention, further research into understanding physical processes that govern floodplain sediment storage patterns may allow managers to focus sediment retention management efforts more effectively. This study seeks to add to this line of research by attempting to address a fundamental research question:

How do interpretations of (or based on) contemporary high-resolution topographic data inform conceptualizations of floodplain sediment patterns?

To answer this question, this study will compare characterizations and quantifications of floodplain conditions presumed to affect sediment spatial patterns with the aid of contemporary high-resolution topographic data. Predictive models will be developed to assess the relative importance of various conditions in explaining spatial patterns of floodplain sediment characteristics, namely sediment texture. It is the intent of this study to update our current understanding of floodplain topography's interactions with flow as it pertains to floodplain sediment dynamics and retention.

Section 2: Characterizing Sediment Deposition, Floodplain Topography, and Hydraulic Processes

Floodplain sediments are not deposited evenly or at random, but as a function of floodwaters across the floodplain. Sediments in transit are deposited when floodwaters lack sufficient transport capacity, a function of predominantly shear stresses acting on a given particle and that particle's size. When shear stresses associated with floodwaters drop below a given threshold, the particle in question settles out of suspension (Knighton, 2014). As stresses exerted by floodwaters vary across a floodplain spatially and temporally, sediment deposits of varying particle size and depth are likewise deposited heterogeneously (Leopold et al., 1964; Gergel et al., 2002; Hupp et al., 2009). Over time, repeated sediment accretion can form topographic features commonly found on floodplains, such as levees.

Floodwaters and their associated sediment deposits create, destroy, and sculpt new micro-¹ and macro-topographic² features over both the short-term and long-term. Altered topographic patterns influence future depositional patterns by altering the complex spatiotemporal patterns of stresses exerted by floodwaters (Wolman & Miller, 1960; Asselman & Middelkoop, 1995; Song et al., 2014). Furthermore, complex patterns of flow stresses (and the consequent mosaic of sediment deposits) play a major role in determining riparian plant community structures. Like floodplain topography, floodplain vegetation's spatial organization, composition, and density influence future flooding events as a vegetative roughness condition (Harris, 1987; Sparks & Spink, 1998; Steiger and Gurnell, 2003; Unger & Muzika, 2008). Because of feedback loops that span multiple temporal scales, floodplain sediment dynamics are considered complex.

Given the potential complexity of floodplain sediment dynamics, it is important to consider how existing methods characterize [1] sediment deposition and erosion, [2] topographic conditions that modify flow processes, and [3] flow processes that govern sediment deposition. The following introduction will review how existing floodplain sediment research measures, models, and quantifies these variables.

¹ Topographic features <10m² in area.

² Topographic features >10m² in area.

Subsection 1: Floodplain Sediment Deposition and Erosion

Gellis et al. (2009) categorized various methodologies currently in use for measuring floodplain sediment deposition into three broad categories: [1] **field approaches**, i.e. *in situ* methods such as bank pins and feldspar clay pads; [2] **surrogate approaches**, which utilize indirect measurements of related variables such as geochemical tracer concentration to infer sediment flux rates; and [3] **modeling approaches**, which utilize (but are not limited to) empirically-derived data and/or general physical equations to estimate watershed-scale spatial fluxes of sediments. This review will focus on field and surrogate approaches, as modeling approaches typically feature empirical data collected by field and/or surrogate approaches and are primarily focused on much larger scales than this study's intent.

Field approaches directly measure sediment deposition or erosion rates at a site over time. Conventionally, bank pins and feldspar clay pads are deployed *en masse* along floodplain transects aligned perpendicular to a channel; pins and pads are then closely monitored for years to approximate local sediment dynamics. For example, Noe & Hupp (2009) characterized sediment accretion rates and associated nitrogen, carbon, and phosphorus concentrations for seven freshwater, non-tidal floodplains in the Chesapeake Bay watershed by deploying several floodplain transects spaced fifty to a hundred meters apart. Each transect featured four to six monitoring locations where a pad collected deposited sediments on average from 1996 to 2003. Accretion rates and associated nutrient concentrations collected over this period were then extrapolated for

the remaining floodplain area of each sampled river to estimate total sediment flux and storage conditions.

Surrogate approaches indirectly measure floodplain sediment dynamics by measuring variables related to sediment deposition or erosion. In many cases surrogate approaches are utilized (a) when a historical record of data is lacking, and/or (b) where an appropriate spatial resolution of sediment dynamics is too costly, dangerous, and/or impractical to field measure. Examples of surrogate approaches include dendrogeomorphology (Hupp & Morris, 1990), radioactive tracers (Pennock & De Jong, 1987), and monitoring changes in LiDAR-derived topography (Thompson & Croke, 2013). Ritchie and McHenry in their 1990 meta-analysis, for example, expounded on methodologies using a radioactive tracer (Cesium-137) from nuclear weapons testing to measure soil erosion and accumulation rates over the past (at the time of their review) twenty years. Studies cited by Ritchie and McHenry measured ^{137}Cs concentrations within vertical soil profiles at depositional sites across various floodplains. Knowing when measurable radioactive isotope concentrations would have appeared in the soil profile³, researchers were able to determine the average floodplain sediment deposition rate across several decades by measuring the depth of the deepest soil horizon containing ^{137}Cs concentrations.

While in some cases highly accurate at specific points along a transect, most field and surrogate methods for measuring patterns of sediment accumulation/erosion bring with

³Approximately 1954 (Kleiss, 1993)

them inherent assumptions about the spatial homogeneity of metrics measured. To elaborate, field and surrogate methodologies generally make two assumptions when sampling along transects:

- a) It is assumed that sediment accumulation or erosion rates measured at points along a transect are representative of rates *between* points along a transect.
- b) It is assumed that that sediment accumulation or erosion rates measured along transects are representative of rates *between* transects (i.e., longitudinally).

These assumptions become potentially unrealistic when coupled with the fact that for many studies, points along cross-sections are regularly spaced tens of meters apart and the distances between cross-sections further still. This was the case in Noe and Hupp (2009), where approximately seventy-two marker horizons were extrapolated to determine floodplain sediment accumulation rates across seven watersheds.

Many field and surrogate approaches also rely on data that must be regularly measured over the course of at least half a decade, then averaged to determine an annual rate (e.g. Noe & Hupp, 2009). However, many variables that determine sediment depositional rates vary seasonally (vegetative roughness conditions) or annually (total annual discharge); as such, the temporal assumption that sediment deposition and erosion rates remain static across years or decades is equally tenuous.

With recent advancements in geospatial technologies, high resolution topographic models, and powerful computers capable of processing such models, research into patterns of floodplain sediment accumulation may be able to overcome these shortcomings (Bishop et al., 2012). For example, high-resolution aerial LiDAR surveys appear to effectively mitigate assumptions regarding spatial homogeneity between elevation points. LiDAR systems collect tens to hundreds of millions of elevation points across a given surveyed terrain. A dense “point cloud” is then created in 3D space from said points, with horizontal resolutions as dense as multiple points/m². After conducting multiple LiDAR surveys over multi-year period, a DEM (Digital Elevation Model) of Difference may be generated; in contrast to *point*-based cross-sectional surveys, effectively an *areal* measurement of topographic change.

A recent example is showcased in Thompson & Croke’s 2013 paper on the hydrogeomorphic effects of a major flood in Lockyer Valley, southeast Queensland. Utilizing multi-temporal one-meter cell resolution LiDAR surveys, Thompson & Croke generated a DEM of Difference to estimate a sediment budget for both confined and unconfined valley reaches affected by the flood. When combined with their landform classification assessment and hydraulic flow model of the flood, Thompson & Croke’s work represents a comprehensive assessment of both direct and indirect measurements of sediment accumulation and the underlying conditions governing them.

Subsection 2: Macro- and Micro-Topography

Given the risks inherent to collecting flow measurements such as velocity, depth, and bed shear stress during a flooding event, historically many researchers relied on what was theorized to be surrogates for floodplain hydraulic conditions. This generally took the form of qualitative assessments of local topographic features (Bishop et al., 2012). Mapping macro- and micro-topographic landforms, their effects on flow routing, and their consequent role in determining hydrogeomorphic conditions and riparian vegetative composition have been discussed at length (Hupp, 1982; Unger & Muzika, 2008; Gergel et al., 2002; Bishop et al., 2012; Song et al., 2014; Song et al., 2017). To summarize, floodplain topography is a direct result of flow processes acting on a floodplain during a flooding event, depositing or eroding sediments stored as topography; over time new topography is created or sculpted, thus influencing future flow routing during floods (and future depositional/erosional patterns). Ergo, a firm quantitative understanding of interactions between flow processes and the spatial arrangement of floodplain topography is highly desired.

While originally reliant on qualitative interpretations of landscape photography or quantitative but spatially-limited manual field surveys (e.g. Marston et al., 1995) for mapping flow-altering landforms, recent technological advances have allowed for more advanced geospatial analyses. Buoyed by modern high-resolution topographic models and computers capable of performing advanced calculations on large detailed datasets,

recent research towards generating more quantitative topography classifiers has spawned several avenues of approach (Bishop et al., 2012).

A major goal in modern geospatial analysis research is developing an automated methodology for quantifying and/or classifying characteristics of a terrain. This methodology must be (a) replicable through time, (b) replicable across various spatial scales, reliefs, and orientations, and (c) require minimal user input. With a methodology that satisfies these three conditions, researchers have the potential to quantitatively link floodplain topographic spatial patterns directly to flow processes. For example, Yokoyama et al. (2002) have developed entirely new measures of topography such as “openness” in pursuit of this goal.

Openness, as defined by Yokoyama et al., was termed “an angular measure of the relation between surface relief and horizontal distance”; essentially, a measure of topography based off a terrain’s line of sight. A point’s “openness” values are indicative of the dominance or enclosure of a location relative to another on a topographic plane. Two forms of openness were presented by Yokoyama et al., “positive” and “negative” openness. Positive openness was calculated as the mean zenith angle calculated along all cardinal headings that was unobstructed by the terrain itself in a self-adapting neighborhood window; this metric was positively correlated with presence of concave landforms, such as valley features. Negative openness was calculated identically to positive openness, but utilizing the mean *nadir* angle of the terrain’s surface; in contrast, negative openness was positively correlated with the

presence of convex landforms, such as ridges. Others, such as Jasiewicz and Stepinski (2013), took Yokoyama et al.'s openness metric further, seeking to utilize computer-aided pattern recognition and openness to identify geomorphologic phenotypes.

Subsection 3: Flood Hydraulics

As stated earlier, historically many researchers relied on geospatial analyses of topography as surrogates for floodplain hydraulic conditions during flooding. Technological advancements, however, have allowed researchers to transition from approximating flood conditions from hydrologically-sculpted landforms to directly modeling flow hydraulics during high-flow events. Initially constrained due to computational or methodological limitations, many historical studies were restricted to smaller study areas, less-representative terrain models, or computationally simpler hydraulic models. These included one-dimensional flow modeling, where flow was routed through surveyed channel cross-sections (Woltemade & Potter, 1994), and steady-flow models, where input discharge remained constant (Gergel et al., 2002). More computationally-advanced modeling efforts, such as two-dimensional (flow was routed over a mesh/grid-based surface) or unsteady-flow (discharge changed over the course of the model) models, were spatially limited (e.g., Miller, 1994; Snead & Maidment, 2000). This is not to state that the results of studies utilizing earlier hydraulic modeling programs were incorrect or unrealistic, rather that computational limitations restricted the range of scenarios that could be realistically modeled (and thus studied).

Computational limitations of older hydraulic flow models brought with them inherent assumptions about how flow behaved across reach-scale areas. Many older hydraulic flow models relied on terrain models derived from channel cross-sectional surveys (e.g., Woltemade & Potter, 1994; Carson, 2006). As such, the same assumptions made earlier regarding studying sediment dynamics with channel cross-sections apply here: (a) that the area between points *along* a transect is topographically homogenous, and (b) that the area *between* transects is topographically homogenous. When coupled with the fact that for some studies elevation points along and between cross-sectional surveys are spaced out tens to hundreds of meters apart (e.g., Carson, 2006), the assumption of topographic homogeneity is potentially invalid. This may not be an issue for larger, watershed scale studies. But for studies interested in fine-scale flow patterns across floodplains as they related to sediment retention, hydraulic models should account for topographic heterogeneity at finer scales than older topographic modeling efforts such as cross-sections can capture.

With the aid of high-resolution floodplain topography, advanced modeling programs, and powerful computers for processing such models, there is high potential to directly link modeled flow conditions on the floodplain to spatial sediment patterns. Carson demonstrated the validity of this approach in his 2006 study, where he linked historic alluvial deposits along a mountainous Utah stream to modeled flow conditions on modeled prehistoric topography. While Carson (2006) was restricted to 1D hydraulic modeling due to the nature of their study, other contemporary studies have regularly

demonstrated the ability of modern hydraulic modeling programs to utilize high-resolution topography. For example, Ernst et al. (2010) successfully created a 2D steady-state hydraulic model utilizing high-resolution terrain data (one-meter by one-meter cell resolution) to develop flood risk assessments at an individual-building scale. Future studies focused on flow conditions presumed to govern floodplain sediment pattern should consider utilizing both high-resolution floodplain topography datasets and advanced hydraulic modeling programs.

Section 3: Problem Statement and Approach

Understanding sediment storage spatial patterns is a critical research need for floodplains. Previous research (Noe & Hupp, 2009) suggested sediment storage associated with Coastal Plain floodplains draining Piedmont rivers is critical for understanding sediment inputs into the Chesapeake Bay. Consequently, such Coastal Plain floodplains were also found to store large quantities of nutrients (Noe & Hupp, 2005). As such nutrients are most commonly correlated with fine-grained sediments such as silts and clays, sediment texture is regularly used to study sediment storage and its associated nutrient composition. However, estimates such as Noe & Hupp's may be limited by their reliance on relatively imprecise techniques. Other studies focused on topography resulting from patterns of sediment deposition, such as Scown et al. (2015), struggled to characterize topography in an automated, interpretable manner across spatial scales. Still others, such as Carson (2006), were computationally and methodologically limited to simplistic terrain representations when modeling hydraulic

processes related to sediment dynamics. Furthermore, while some studies integrated parts of the approaches discussed (Marriott, 1992; Carson, 2006), to this study's knowledge no study has attempted to compare these various approaches in one comprehensive study. Former research into sediment dynamics was limited not just methodologically, but technologically to coarse approximations of sediment dynamics and its governing processes.

Modern researchers, however, now have access to high-resolution multi-temporal LiDAR surveys of Coastal Plain floodplains and computers capable of analyzing said topography. 2D, unsteady-flow hydraulic modeling, when paired with analyses of high-resolution floodplain topography and their underlying sedimentology, has the potential to systemically update our current conceptualizations of sediment dynamics on Coastal Plain floodplains. This study seeks to address a fundamental **research question**:

How do interpretations of (or based on) contemporary high-resolution topographic data inform conceptualizations of floodplain sediment patterns?

As an illustrative example, this study will seek to answer the above question by applying high-resolution topography to characterize floodplain conditions using a range of approaches employed in characterizing floodplain sediment deposition. Specifically, this study will aim to satisfy these three **research objectives** by completing the following tasks:

- 1. Characterize and quantify [A] sediment accretion patterns, [B] topographic conditions, [C] flow conditions representative of a major storm event on a Coastal Plain floodplain, and [D] spatial patterns of sediment texture.**
- 2. Compare the results of the characterizations and quantifications of floodplain conditions at the study site to each other, as well as to the existing literature's conceptualization of conditions to be expected at the site.**
- 3. Assess the relative importance of sediment accretion rates, topographic landforms, and hydrodynamic conditions in explaining patterns of floodplain sediment texture at the study site.**

Section 4: Study Site

The Patapsco River runs for 39 miles before emptying into the Baltimore Harbor. It drains an approximately 312 mi² watershed located in Central Maryland and is a humid subtropical climate that receives on average approximately 41 inches of precipitation annually (MD Dept. of the Environment, 2018; US Climate Data, 2018). Precipitation occurs year-round. According to National Land Cover Dataset (Homer et al., 2015), the watershed is 32.49% developed, 34.88% forested, 27.01% agricultural, and 5.62% other. The Patapsco is a relatively narrow, minor river for most of its length, featuring infrequent and narrow alluvial floodplains (Hack, 1982; Terrain 360, 2018). The river's

last ~8 miles feature regular, relatively wide (~1/3 mile in width) floodplains constrained by urban and suburban development. Silt loams of the Codorus, Hatboro, and Elsinboro series are associated with floodplains along the lower Patapsco and range from poorly- to well-drained (Soil Survey Staff, National Resources Conservation Service, 2018).

The Patapsco crosses between the Piedmont and Coastal Plain physiographic provinces between Elkridge, MD and Ellicott City, MD. Colloquially referred to as “The Fall Zone”, this border features a sharp decrease in the river’s longitudinal gradient as it transitions from the topographically variable Piedmont to the relatively flat Coastal Plain (Hack, 1982). Recent Mid-Atlantic studies of the Coastal Plain province have documented relatively large sediment retention rates occurring on local floodplains, “represent[ing] the interception of large amounts of material that otherwise could have been exported downstream [to the Chesapeake Bay]” (Noe & Hupp, 2009). Further studies have documented historical patterns of fluvial aggradation in the form of legacy sediment deposits (Hupp et al., 2013).

While historically its sharp longitudinal gradient made the Patapsco River Valley valuable for generating hydropower, this area remains nationally recognized as recently as summer 2018 for its extreme vulnerability to major flood events (Sharp, 2001; Halverson, 2018). Following recent major storms (Tropical Storm Lee in 2011, and the Ellicott City floods of 2016 & 2018), field observations of the study site exhibit a wide range of hydrogeomorphic and topographic conditions. This is theorized to be a direct

result of a major widening of the river valley and a sharp reduction in longitudinal profile as the river exits the Fall Zone (Hack, 1982; Figure 1.1). Due to the hydrogeomorphic and topographic conditions documented above, the Patapsco River Valley's transition out of the Fall Zone into the Coastal Plain is an ideal study site for illustrating the impacts described by Noe and Hupp.

Given the Patapsco's role as a political boundary between Howard and Baltimore counties, incidentally two overlapping aerial LiDAR surveys were collected of the study site; one in March 2011 by Howard County (pre-Tropical Storm Lee) and one in May 2015 by Baltimore County (post-Tropical Storm Lee), at 2-meter and 1-meter cell resolutions respectively.

This study will specifically focus on two sections of the lower Patapsco floodplain downstream of US I-95 and upstream of US I-195, approximately one mile downstream of the USGS Elkridge stream gage station. In addition to aforementioned valley-scale effects, a large covered culvert bisects the study area into two sections (hereafter referred to as the upstream and downstream sections). Further local effects include for the downstream floodplain section a detention pond, a former oil pipeline dirt road, and a first-order tributary bisecting the floodplain. For the upstream floodplain section, a large power-line cut spans the floodplain. A small drainage tributary is also found on the south-easternmost tip of the upstream floodplain section (Figure 1.2).

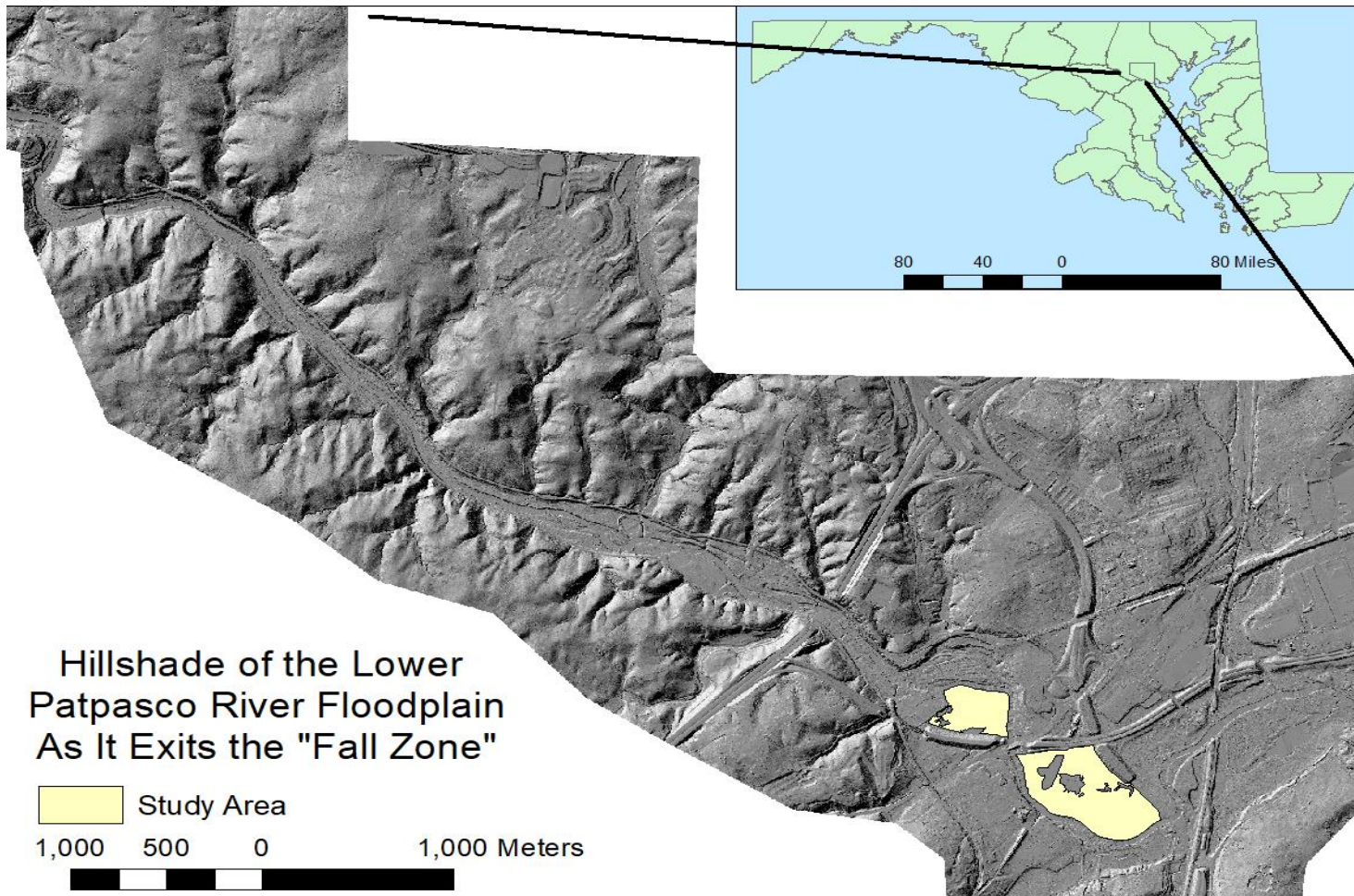


*Figure 1.1:
Hillshade of the
Lower Patapsco
River floodplain,
with study area
highlighted in
beige. (inset):
spatial location of
study area
relative to
Maryland.*

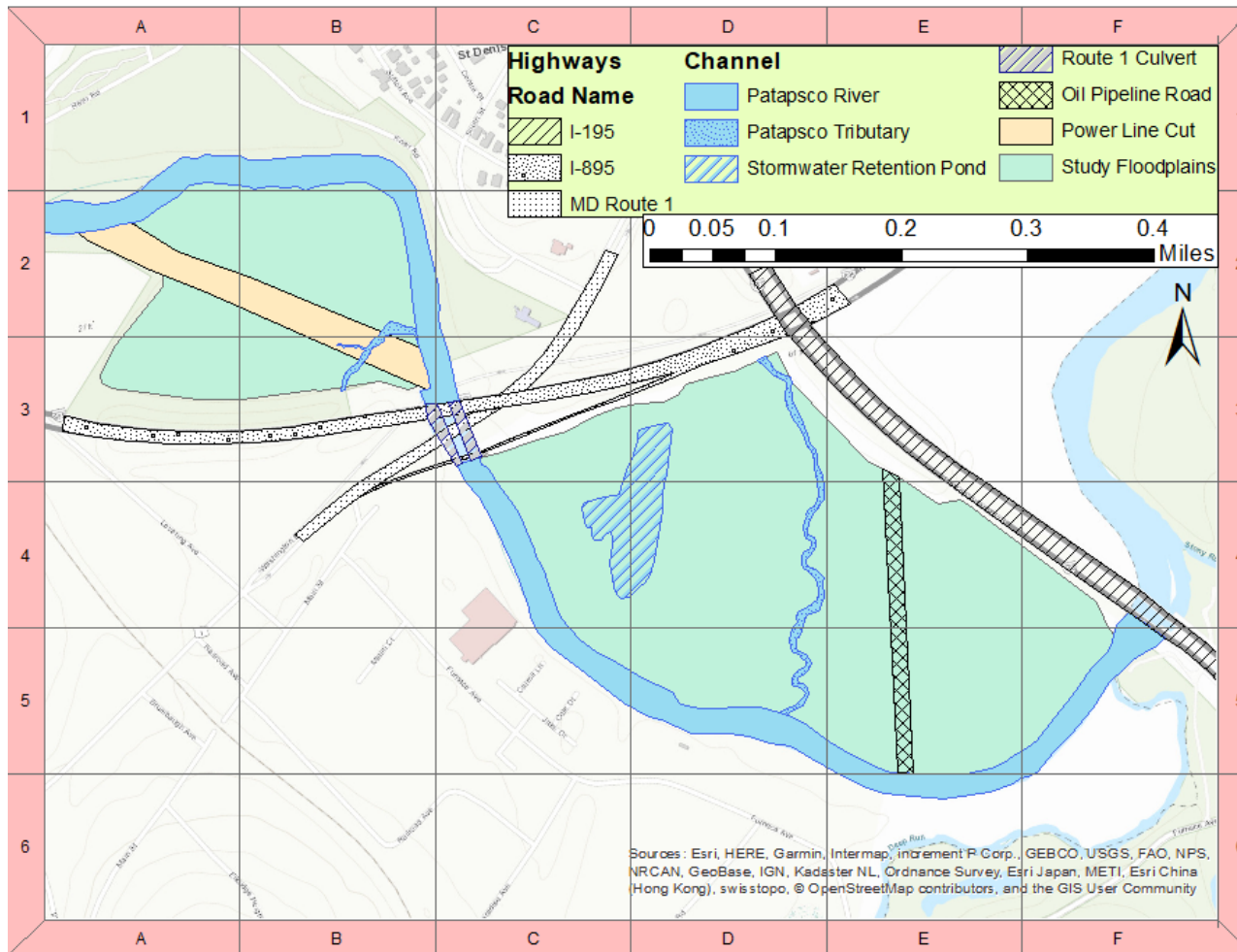


Figure 1.2: Study area depicted, with areas of presumed local effects highlighted. The Lower Patapsco flows from northwest to southeast at this scale. The western floodplain section (grid cells A2, B2, A3, & B3) was designated the upstream section, and the eastern floodplain (grid cells C3-C5, D3-D5, E4, E5, F4, & F5) was designated the “downstream” section.



Image 1.1: [Facing upstream] The Route 1 culvert that bisects the study area into two sections is split into two arches. Sediment regularly collects underneath the arches, to be later flushed out by high velocity flow during storm events. Credit for images: Zach Clifton

Following Tropical Storm Lee and both Ellicott City floods (2016 and 2018), predominantly-sand depositional waveforms from flooding were visible on both study floodplain sections (Image 1.3). These waveforms were found in areas adjacent to the main channel's banks, along with large debris from previous storm events and Tropical Storm Lee. Texture-by-feel observations of surficial soil characteristics suggested that the area encompasses a transition between primarily coarse ($>63\mu\text{m}$) to primarily fine ($<63\mu\text{m}$) sediments. Further observations document a wide vegetative range of varying "hydraulic roughness", from dense *Phragmites* in regularly flooded backswamps, to open irregularly-flooded meadows, to mature floodplain forests. Taken comprehensively, these observations suggest a wide range of depositional, topographic, and hydrogeomorphic regimes are found on the Lower Patapsco floodplain.



Image 1.2: Example of the sand waveforms found on the Lower Patapsco River floodplain after a major flood event.

Image Credit: Zach Clifton



*Image 1.3, 1.4, 1.5, 1.6, & 1.7, from
top left to bottom right:
examples of the wide variety of
vegetation density and composition
found at the study area.*

Credit for Images: Zach Clifton

Chapter 2: Methods

This chapter (and the subsequent Results chapter) are organized as follows. The methods outlined in Section 1 are intended to satisfy research objective 1A by quantifying sediment accretion rates for the study floodplain. The methods outlined in Section 2 are intended to satisfy research objective 1B by characterizing floodplain landforms for the study floodplain. The methods outlined in Section 3 are intended to satisfy research objective 1C by modeling flow conditions across the study floodplain. The methods outlined in Section 4 are intended to satisfy research objective 1D by characterizing spatial patterns of floodplain sediment texture for the study floodplain. The results of Section 1-4 will be later compared, satisfying research objective 2. Finally, Section 5 outlines the predictive models developed to assess the relative importance of each condition quantified/characterized by Sections 1-3 towards explaining spatial patterns of sediment texture on the study floodplain.

Section 1: Quantifying and Mapping Post-Flooding Sediment Accretion

Sediment accretion resulting from Tropical Storm Lee was quantified and mapped for the study floodplain by differencing multi-temporal aerial LiDAR-derived topography surveyed before and after Tropical Storm Lee. Classified aerial LiDAR point clouds and metadata for the Lower Patapsco were downloaded from MD's iMAP website servers (MD iMAP, 2016). LiDAR classification and post-processing were undertaken prior to this study by commercial vendors for each county. LiDAR-derived bare-earth

DEMs were generated within ArcMap for each survey year's dataset; cell resolution was determined based on iMAP-provided metadata. A two-meter cell resolution was established based on a reported point spacing of 1.4 meters for the 2011 Howard County dataset. Likewise, a one-meter cell resolution was established based on a reported point spacing of 0.7 meters for the 2015 Baltimore County dataset. DEMs from 2011 and 2015 were subtracted from each other in ArcMap (2015 -2011) to generate a two-meter cell resolution DEM of Difference (DoD) for the study area.

Two quantifications of a minimum level of detection threshold (minLOD , i.e. the smallest detectable elevation change distinguishable from random point cloud noise) for the DEM of Difference. Defined as the "regional" minLOD and the "localized" minLOD , they were intended to bookend change detection thresholds between a very conservative estimate (i.e., regional minLOD) and an optimistic but likely-unrealistic estimate (i.e., localized minLOD). Two additional change detection thresholds between these bookends were also utilized to compare intermediary estimates of topographic change.

The regional minLOD utilized the county-wide vertical accuracy RMSEs (Root Mean Square Errors) provided by LiDAR metadata to quantify surface representation uncertainty in the DoD. The 2011 survey reported a vertical RMSE of 18.5cm, whereas a RMSE of 6.79cm was reported for the 2015 survey. RMSEs were interpreted to quantify the surface representation uncertainty of each dataset, utilizing the same

methodology⁴ as Wheaton et al. (2010) and Thompson & Croke (2013). RMSEs were also assumed to be the same for both positive and negative uncertainty in representing terrain. The regional minLOD was obtained by squaring, summing, then calculating the square root of both RMSEs. Propagated uncertainty was then approximated assuming infinite degrees of freedom, leading to a 95% confidence interval of approximately $\pm 0.386\text{m}$.

To quantify surface representation uncertainty with the localized minLOD , presumed areas of negligible elevation change between 2011 and 2015 were identified. For this study, roads such as I-195 and I-95 were selected. A total of 270 points were randomly generated within areas of negligible change. Difference in elevation between the two LiDAR surveys was recorded at each point, and the standard deviation, RMSE, and the average difference in elevation were calculated. Mean elevational change was -0.0273m , consistent with an interpretation of zero directional bias. The calculated RMSE (0.0128m), multiplied by the critical student's t value at a 95% significance level (for 269 degrees of freedom, $t=1.969$), resulted in a localized confidence interval of 0.0252m .

⁴ Adapted from Taylor's (1997) modified error estimation equation; this methodology is also referred to as probabilistic thresholding by a user-defined threshold in the literature.

Table 2.1: Various metadata associated with the aerial LiDAR datasets utilized.

	2011	2015
County surveyed	Howard County	Baltimore County
Date(s) Collected	03/27/2011 - 03/28/2011	05/06/2014 - 05/07/14
Date Published	06/08/2011	April 2015
Nominal Point Spacing	1.4 pts/m ²	0.7 pts/ m ²
Cell Resolution	2 meters	1 meter
LiDAR instrument used for collection	Leica ALS50	Reigle 680i

Section 2: Characterizing Floodplain Landforms

Floodplain topographic patterns such as ridges, flats, and depressions for the study floodplain were classified utilizing the same methodology as Stepinski & Jasiewicz (2011) and Jasiewicz & Stepinski (2013), where topography was classified into geomorphologic phenotypes (colloquially termed “geomorphons”). As defined by Jasiewicz and Stepinski, a geomorphon is a “specific spatial arrangement of elevation values in a selected region of a DEM [Digital Elevation Model].”. Analogous to

“textons” as defined by Julesz (1981), a geomorphon in essence is a “fundamental micro-structure of a landscape” (Jasiewicz and Stepinski, 2013).

Geomorphons are orientation-independent and limited to a set of only 498 different arrangements because of their basis on local arrangements of elevational values. As values of neighboring DEM cells are classified according to whether (relative to the central cell) they represent an increase in elevation, a decrease in elevation, or experience no change in elevation, geomorphons are also relief-independent. Geomorphon classifications include common landforms such as ridges, valleys, hollows, or spurs, and are calculated via “a neighborhood with size and shape that self-adapts to the local topography” (Jasiewicz and Stepinski, 2013) comparable to Yokoyama et al.’s self-adaptive neighborhood window. Instead of utilizing measures of surface geometry as other studies have done (e.g. Scown et al., 2015), geomorphons are analogous to interpretive landform mapping done by experienced landform geographers. By utilizing technologically-aided pattern recognition and openness, however, an element of technological objectivity is introduced, while maintaining the adaptive ability previously displayed by human geographers to recognize important flow-altering landforms.

Prior to characterizing landforms, however, minor topographic modifications were needed. Given the documented “noisiness” of aerial LiDAR when modeling topography in riparian vegetated areas (e.g. Hutton & Brazier, 2012), a filtered version of the one-meter cell resolution 2015 DEM was proposed. This filtered version was

generated by inputting the 2015 DEM into the ArcGIS function *Filter* with “low pass” selected. Through this function a filtered DEM was generated by calculating the mean elevation within a three-meter by three-meter moving neighborhood window for each cell. The Filtered terrain was imported into GRASS GIS, and the GRASS extension *r.geomorphon* was then run with the following parameters: outer search radius of thirty meters, inner search radius of zero meters, a 1 degree flatness threshold, and a zero meter flatness distance. These parameters were deemed acceptable based on field observations of floodplain topography on the study area and an interest in documenting both macro- and micro-topography. *R.geomorphon* results for the unfiltered version of the 2015 terrain may be found in the Appendices section (5.4).

Section 3: Modeling Representative Flow Conditions on the Floodplain

To model hydrodynamic flow conditions representative of a major storm event on the lower Patapsco floodplain, a 2D unsteady-flow hydraulic model of floodplain hydrodynamic conditions was generated with HEC-RAS version 5.0 (USACE [1], 2016). The Hydrologic Engineering Center’s River Analysis System, more commonly referred to as HEC-RAS, was and remains one of the most oft-applied programs for modeling flow hydraulics. Others such as MIKE11, iRIC, RMA2, and TUFLOW have also seen regular use (Miller 1994; Woltemade & Potter, 1994; Snead & Maidment, 2000; Thompson & Croke, 2013; Shokory et al., 2016), however HEC-RAS’s compatibility with high-resolution topographic data, incorporation of the “GDAL” geospatial library, user accessibility, and cost made it the optimal choice for this study.

To generate a 2D unsteady-flow model, HEC-RAS solves for flow momentum vectors across a user-defined computational subgrid with either full Saint Venant equations (i.e. shallow water equations derived from Navier-Stokes equations) or a simplified version termed the Diffusive Wave Approximation of the Shallow Water (DSW) equations. By assuming the horizontal length scale is much larger than the vertical length scale (i.e. shallow flow), the DSW equations assume that pressure is effectively hydrostatic, and that gravity and friction associated with underlying topography are the dominant terms in the momentum equations. This allows the vertical velocity, vertical derivative, unsteady, advection, Coriolis, and viscous terms when solving the Navier-Stokes equations to be disregarded, reducing computational times in the process (USACE [2], 2016). Exploratory analyses utilizing the Saint Venant equations and the DSW equations revealed no identifiable differences in model outputs between the two equation series, so DSW equations were used.

To further reduce computational times, HEC-RAS utilizes the subgrid bathymetric approach whereby a user-defined subgrid coarser in resolution than the underlying topography contains fine-scale information about said underlying topography. This information can then be factored out as a series of parameters representing multiple local slope-volume integrals representative of the underlying topography. This allows HEC-RAS to preserve information about higher-resolution topographic details while solving for flow momentum conservation for flow entering, flowing through, and exiting coarser subgrid cells (USACE [2], 2016). Given a one-meter cell resolution

bare earth DEM generated from Baltimore County's 2015 LiDAR survey, a 4.27m by 4.27m subgrid was chosen to streamline processing times while still preserving fine-scale topographic information.

While the DEM was generated following the same procedure detailed in section 1 of this chapter, some DEM modifications were made to better represent real-world topographic and bathymetric conditions. Channel bathymetry for the Patapsco main channel was altered to reflect approximate channel depth using eleven Maryland Geological Survey channel cross-sections collected in May of 2016. Cross-sectional channel profiles were interpolated longitudinally using GeoRAS, an ArcGIS toolbox for geospatial data manipulation in HEC-RAS. Additionally, two open-faced parallel channels, surrounded by artificially elevated terrain, were created to mimic the constraining effects on flow theorized to occur at the Rt. 1 culvert. Finally, to mitigate any possibility of the downstream boundary erroneously influencing flood dynamics, floodplain topography within 1 mile downstream of the study area was included (Figure 2.1).

Tropical Storm Lee discharge data collected by the USGS Elkridge stream gage were downloaded from Sept. 5th, 2011 to Sept. 11th and imported into HEC-RAS as the inflow hydrograph boundary condition. Given the short distance and a lack of major tributary inputs between the gage site and the study area this was deemed acceptable (Figure 2.1). Average in-channel slope along ten longitudinal profiles were extracted from 2015 LiDAR data along the upstream study site boundary, and input as the "EG

Slope for Distributing Flow Along BC Line” parameter. A short “warm-up” period (~1 day) of roughly steady-flow conditions was included in the discharge dataset to ensure that the channel was equilibrated to steady-state flow before flooding occurred. Downstream boundary conditions were designated by the “normal depth” setting, calculated by averaging in-channel slope along ten longitudinal profiles extracted from 2015 LiDAR data. From this a friction slope of 0.02 was input. Given the high resolution of LiDAR dataset used and computational limitations with such, a computational mesh grid with 10m cells was deemed justified.

Tropical Storm Lee occurred in 2011, four years before the 2015 Baltimore County LiDAR survey was flown, thus an argument can be made that this model is chronologically illogical. However, the intent of this study is not to model hydraulic flow processes on the lower Patapsco floodplain specific to that caused by Tropical Storm Lee; instead, the intent is to model hydrodynamic flow processes *representative* of possible flow conditions on the floodplain. Therefore, chronology doesn’t need to be preserved for this model if both topographic and hydrodynamic conditions are representative of possible conditions on the floodplain. A similar argument can be made that Tropical Storm Lee is an extreme storm event for the area with an annual exceedance probability of approximately <4% (Suro et al., 2015). However, given [1] the irregularity of overbanking events on the lower Patapsco floodplain due to highly incised channels, [2] the number of recent extreme storm events with similar hydrographs that also caused overbank flooding on the Lower Patapsco floodplain, and [3] the possibility of fluvial disequilibrium in the Chesapeake Bay watershed due to

changing land use patterns since European colonial settlement and climate change (Matonse & Frei, 2013; Kochel et al., 2016), Tropical Storm Lee was deemed an acceptable hydrologic event for this study.

Based on a qualitative survey of vegetation composition and density across the study area, an approximated dataset of spatial Manning's N roughness values was input into HEC-RAS to estimate floodplain vegetative roughness. Manning's roughness coefficient values for the dataset were derived from Phillips & Tadayon's report on Manning's roughness coefficient values for channels and floodplains (2006). A map of assigned Manning's N values can be found in Figure 2.2.

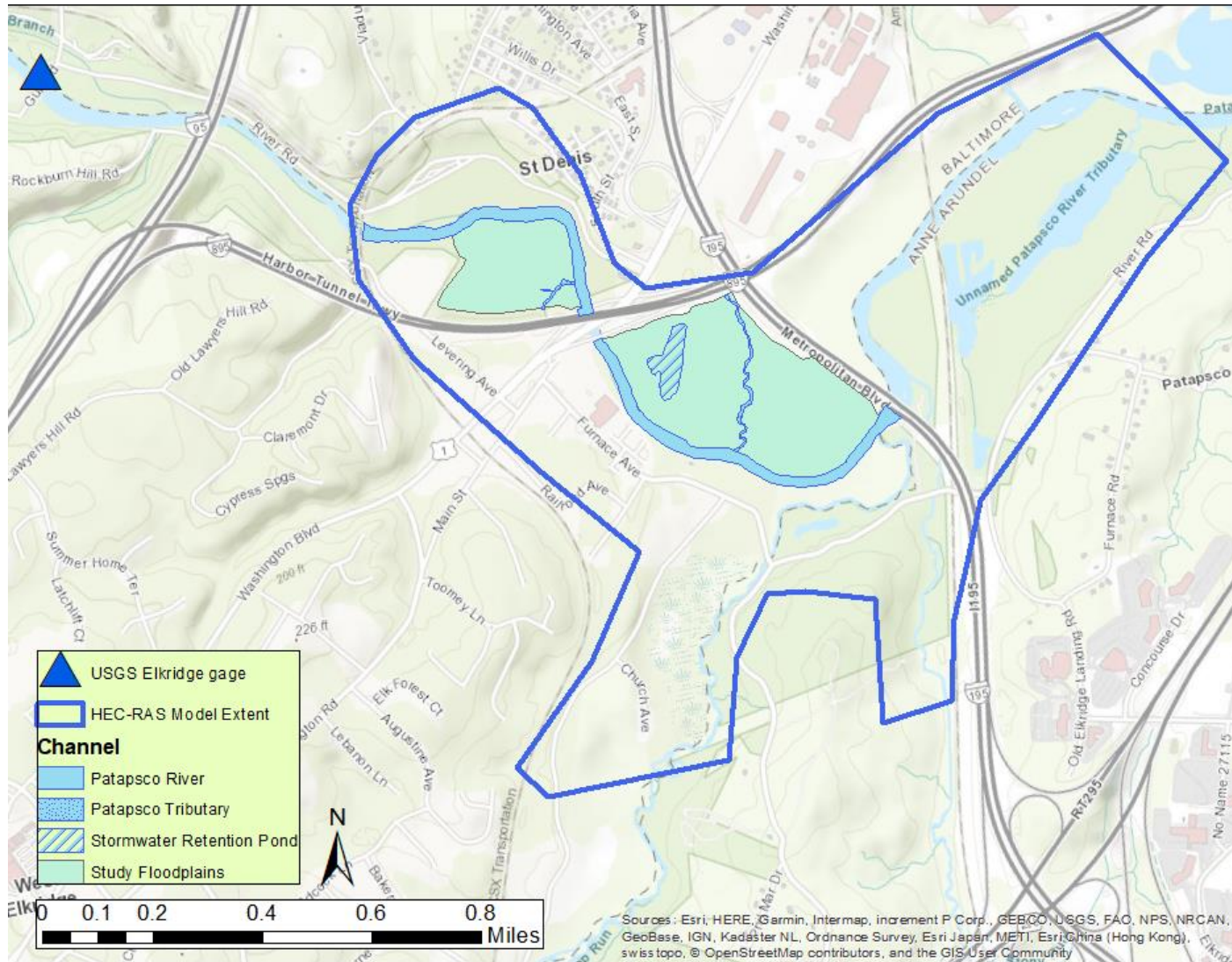
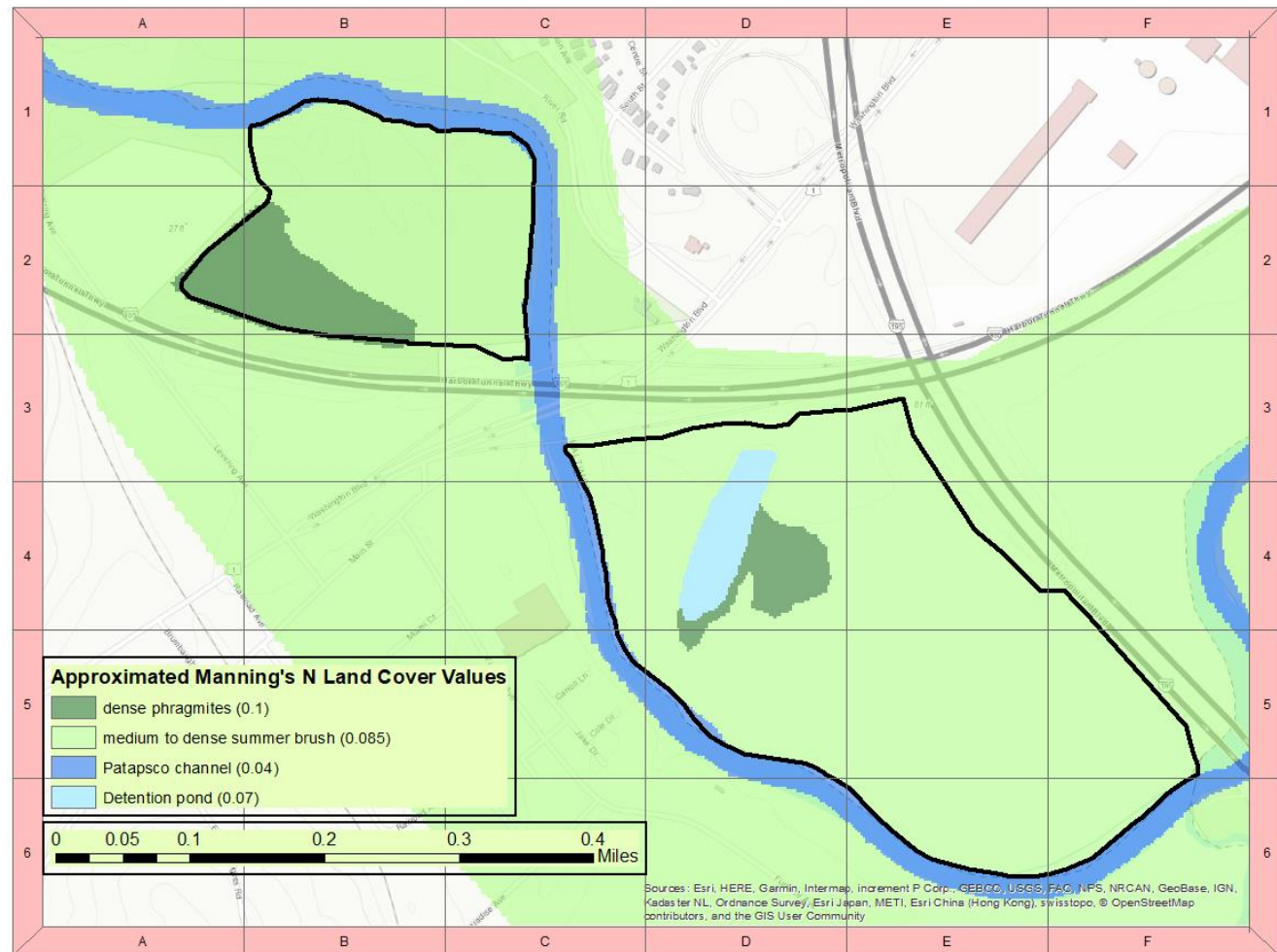


Figure 2.1: Extent Map (in blue) of floodplain terrain input into the 2D HEC-RAS model. Also shown is the USGS Elkridge stream gage (as a blue triangle), ~1 mile upstream of the study area.

Figure 2.2: Map of the spatial distribution of Manning's *N* roughness coefficient values of the study area. Values were approximated based on field observations of vegetation conditions at various locations across the study area.



Following model processing, six conceptual periods in an archetypal hydrograph (i.e., not a specific storm's hydrograph, but a generalized storm hydrograph) were defined. These periods were based on the hypothesized importance of major phase-shifts in flow velocity magnitudes, inundation extents, and/or flow routing over an archetypal storm's course. Given the relationship defined in the literature regarding flow processes as they pertain to floodplain sediment patterns (Leopold et al., 1964; Marriott, 1992; Gergel et al., 2002; Carson, 2006; Hupp et al., 2009), conceptual periods selected for each represent an alternative hypothesis about which periods are important for explaining floodplain sediment spatial patterns. Conceptual periods were defined as such:

- Initial Overbanking: When in-channel flow overtops the levees immediately adjacent to the main channel.
- Initial Backfilling: When in-channel flow is impeded by valley constraints, including artificial constraints such as culverts, and backfills onto the floodplain.
- Splaying: When in-channel flow overtopping a channel levee spills out onto the interior floodplain, but prior to peak inundation.
- Peak Flow: When most of the floodplain is inundated and mean velocities are near or at their fastest.
- (Earlier) Drainage Period: Given the relatively longer falling limb of the archetypal hydrograph, two sub-periods during the drainage period were selected to model changing flow conditions.
- (Later) Drainage Period: See above annotation.

Rasters representing modeled flow velocity and bed shear stress⁵ during each conceptual period were extracted from HEC-RAS and imported into ArcGIS. The exact timing within the hydraulic model to extract flow metric rasters representing a given conceptual period was visually determined based on inundation extent and flow velocities. A noticeable difference in timings of flow patterns and inundation extents was identified between the two study sections; this suggested a significantly different hydrologic regime between the two sections in timing of the conceptual periods. As such, exact timings of conceptual periods differed between study floodplain sections. In total 10 different exact timings of conceptual periods were selected to examine.⁶

⁵ Shear stress is calculated by HEC-RAS as $\tau = \gamma * R * S$, where τ = shear stress calculated for each subgrid face, then interpolated between faces, γ = the specific weight of water, R = hydraulic radius, and S = slope.

⁶ One exact timing was shared for both sites (Initial Overbanking), and the downstream section saw no backfilling so an exact timing was not selected. For the exact times selected, see Table 5.1 in the Appendices section.

Section 4: Quantifying Sediment Characteristics for the Study Floodplain

Sediment texture, i.e. the relative proportion of particles of varying sizes by weight, can be used to understand spatial patterns of floodplain sediment storage, and associated nutrient storage. Thus, to assess floodplain sediment characteristics for the lower Patapsco, sediment texture was measured across the study area. Spatial patterns of sediment accretion and flow conditions, determined from the topographic differencing analysis and hydraulic modeling results, in addition to field observations, were utilized to select and stratify soil core sampling sites. Multiple parameters from these analyses were used to guide placement. Emphasis on site selection was placed on (a) capturing a wide range of sites and (b) covering a variety of factors, including: distinct spatiotemporal shifts in flow velocities (direction and/or magnitude); depositional patterns; distance from where flow models predicted significant overbanking events; distance from the main channel; and field observations of local topographic features and vegetation composition. Eight sampling sites within the study area were selected. A total of nine sediment core samples were collected across three replicates at each site for a total of 72 sediment core samples (Figure 2.3).

At each of three representative locations for each site, three sediment cores were collected in a radial pattern at random distances between zero and thirty meters. A sample was collected at 0°, 120°, and 240° according to a handheld compass. Samples were collected vertically of the first 6 inches of soil with 1” by 6” steel tubes; each

sample location was marked by a handheld GPS unit⁷ and a spray paint identifier/orange construction flag. Sample tubes were sealed with rubber end caps, and labelled with a site number, scan number, sample number (1,2, or 3, where 1=0°, 2=120°, and 3=240°), and the distance from the central measuring point to the sample in meters.

⁷ A Garmin 60CSx.

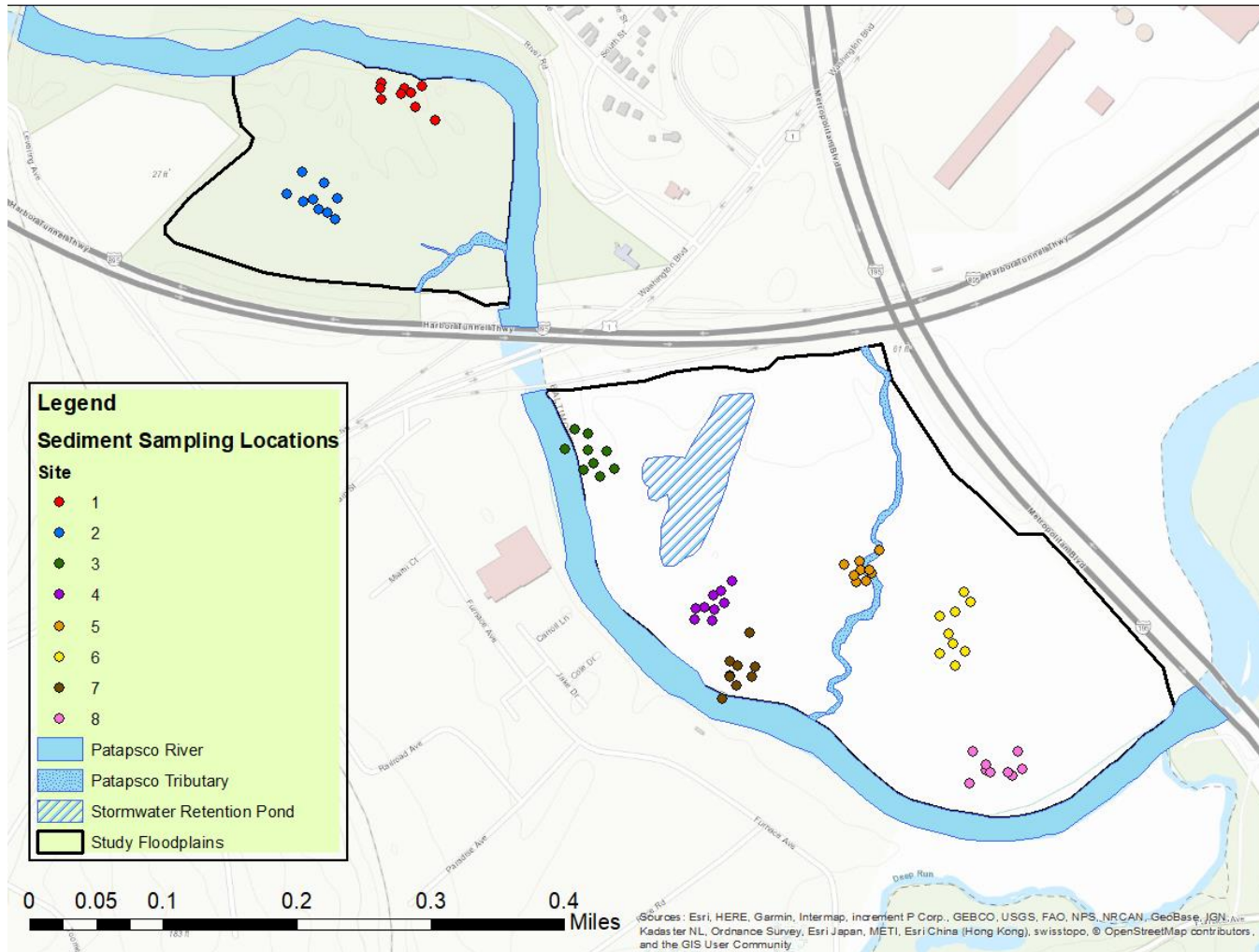


Figure 2.3: Sediment core sampling plan; cores were later analyzed for particle size distribution.

After collection, soil core samples were brought back to UMBC for logging and particle size analysis via the Bouyoucos hydrometer method (Bouyoucos, 1951; Poppe et al., 2000; Schwartz & Smith, 2016). This method was selected due to prior experience, available lab resources, and ease of implementation. The hydrometer method relies primarily on Stokes' Law:

$$F_d = 6\pi\eta rv$$

Where F_d = the frictional force exerted on a given particle moving through a fluid, η = the dynamic viscosity of the fluid, r = the radius of a given particle, and v is the flow velocity relative to a given particle. Assuming spherical, smooth particles of a uniform density flowing laminarily through a fluid of a constant density and viscosity, Stokes' Law is used here to determine sedimentation rates of particles varying in size. While this method can be used to distinguish more than three soil particle size classes proportions, only the major three (sand, silt, and clay) were selected for this study.

The hydrometer method relies on mechanical and/or chemical means to disassemble soil aggregates into discrete particles before particle size analysis. Particle size distribution was assessed with a slightly modified version of the hydrometer method (graciously provided by Dr. Stu Schwartz at UMBC's Center for Urban Environmental Research and Education) involving both mechanical and chemical means for aggregate separation. Soil samples were oven dried, then lightly ground with both ceramic and

rubber-tipped pestles to break up predominantly clay-based aggregates without breaking up larger particles (such as gravel or brick fragments).

Approximately 200 mL of deionized water and 100 mL of 5% sodium hexametaphosphate solution (a chemical deflocculating agent) and were then added to the sample. The sample solution was agitated with an industrial mixing machine to ensure complete deflocculation of soil particles. The solution was then transferred to a 1L volumetric glass cylinder, where the remaining volume was filled to 1L with deionized water. A control cylinder was also created, consisting of 100mL of the 5% sodium hexametaphosphate solution and 900 mL of deionized water. The specific gravity of the control cylinder was then measured with an ASTM-152H hydrometer and recorded, as was both the control and test cylinders' temperatures.

The test cylinder was closed with a rubber stopper and inverted several times (≥ 20) to ensure that all particles were in suspension. A stopwatch was started, and the cylinder was quickly placed vertically on a flat surface. After removing the rubber stopper, 2-3 drops of amyl alcohol were added to disperse bubbles and a hydrometer was immediately inserted into the solution. Specific gravity readings of the solution were measured and recorded at fifteen seconds, thirty seconds, forty seconds, one minute, two minutes, one hour, two hours, any time between 4 hours and 6 hours, and any time between 23 and 26 hours. Measurement times were selected to develop a regression curve of which soil size classes were settling out of suspension, allowing for later calculation of particle size class proportions within the soil core sample. Temperature

of both the test and control cylinders were also recorded for each time interval, excluding any time intervals within the first 2 minutes. The control cylinder's specific gravity is also recorded for these same time intervals.

After 24 hours the experiment results were used to calculate specific proportions of three particle size classes, controlling for temperature. To visualize the soil textural data graphically, a ternary plot of particle size results for all samples was generated with “ggtern”, (Hamilton, 2017) a graphical package within R. Soil textural data was also visualized spatially with a Kriging interpolation for each particle size class analyzed for.



Images 2.1-2.4 (from top left to bottom right)

Image 2.1: Soil sample collection at study area, facilitated by a hand shovel (left).

Image 2.2: After oven drying, soil samples were ground before particle size analysis.

Image 2.3: Various soil samples mid-particle size analysis.

Image 2.4: Close-up of a 1L volumetric cylinder mid-particle size analysis; particle size stratification at the cylinder base reflects the varying deposition rates expected with various particle sizes.

Section 5: Assessing the Relative Importance of Hydrogeomorphic, Topographic, and Geometric Conditions in Explaining Spatial Patterns of Floodplain Sediment Texture

To demonstrate high-resolution topography's utility in relating floodplain conditions presumed to govern floodplain sediment characteristics at a single study site⁸, a multivariate analysis was conducted. The intention of this multivariate analysis was to quantitatively represent a series of hydrogeomorphic, topographic, and geometric conditions on the floodplain, and to assess their relative ability to explain spatial patterns in floodplain sediment texture. In that pursuit, a classification and regression tree (CART) analysis was determined to be the most appropriate mode of statistical analysis.

CART analyses, specifically regression trees, have several benefits when compared to alternative multivariate statistical analyses. When working with datasets where several variables act in complex, nonlinear fashions (e.g., sediment dynamics), global statistical models like multivariate linear or polynomial regressions can be difficult to construct and later interpret. Regression tree analysis results, however, are relatively easy to explain graphically (Gareth et al., 2017). Furthermore, many variables understood to be associated with spatial patterns of floodplain sediments are believed to covary. For example, it is commonly understood that stream power varies with longitudinal distance downstream (Sparks & Spink, 1998; Barker et al., 2009), affecting sediment erosion and deposition patterns; this violates the assumptions of

⁸ the third research objective outlined in section 3 of the introductory chapter

many multivariate statistical analyses, such as principle component analysis. Still others only allow for either categorical or numerical data, or struggle with large datasets. CART analyses, on the other hand, are capable of handling large datasets of both numerical and categorical data and are robust against collinearity. To do so, a regression tree analysis recursively partitions the full dataset into smaller, more manageable regions.

Each zone of partitioning is referred to as a “nodal split”, where a single explanatory variable (e.g., flow velocity at peak flow) divides the full dataset into two sub-datasets (e.g., group A $> 2\text{ft/s}$ & group B $\leq 2\text{ft/s}$). The dataset (or sub-dataset) being split are referred to as “parent nodes”, and the two split sub-datasets are referred to as “child nodes”. The explanatory variable selected for each nodal split is the variable that most reduces the sum of internal variance of the two individual child nodes relative to the internal variance of the parent node (i.e. which nodal split divides the parent node in such a way that two distinct child nodes emerge with minimal overlap?) (Loh, 2011; Neuman & Cohen, 2014). Eventually, the internal variance of the parent node is too small to be reduced by nodal splitting; this process repeats across all child nodes, visualized graphically as a hierarchical regression “tree”.

A regression tree analysis requires two sets of variables: an explanatory variable set, and a response variable set. For this study, the explanatory variable set consisted of hydrogeomorphic, topographic, and geometric variables representing hydrogeomorphic, topographic, and geometric conditions found on the floodplain

presumed to influence floodplain sediment characteristics. A full list of the variables included in the explanatory variable list can be found in Table 2.2. Data associated with each of these variables were extracted from the results of the topographic differencing analysis, hydraulic model, and landform characterization analysis at the same pixel from which soil samples were collected. Two geometric variables, termed “distance from the main channel” and “longitudinal distance downstream”, were also included given their previous use in the literature when explaining spatial patterns of sediment texture (Osterkamp & Hupp, 1985; Asselman & Middelkoop, 1995; Barker et al., 2009). Distance from the main channel was defined as the Euclidean distance from the Patapsco’s main channel and calculated with ArcGIS’s *Euclidean Distance* function. Longitudinal distance downstream was defined as the Euclidean distance from an arbitrary point in the Patapsco’s main channel immediately upstream of the study area and calculated with ArcGIS’s *Euclidean Distance* function. Finally, the response variable set was composed of sediment texture proportions being predicted for (% sand, % silt, or % clay).

Table 2.2: Full list of explanatory variables representing hydrogeomorphic, topographic, and geometric conditions found on the floodplain presumed to influence floodplain sediment characteristics, including units.

Input (Explanatory) Variables	Variable Units	Condition Represented
Change in elevation between 2011 and 2015	Meters	Sediment accretion rates
Flow Velocity during the Initial Backfilling Period	Ft/sec	Flow conditions during the Initial Backfilling Period
Flow Velocity during the Initial Overbanking Period	Ft/sec	Flow conditions during the Initial Overbanking Period
Flow Velocity during the Splaying Period	Ft/sec	Flow conditions during the Splaying Period
Flow Velocity during the Peak Flow Period	Ft/sec	Flow conditions during the Peak Flow Period
Flow Velocity during the Earlier Drainage Period	Ft/sec	Flow conditions during the Earlier Drainage Period
Flow Velocity during the Later Drainage Period	Ft/sec	Flow conditions during the Later Drainage Period
Shear Stress during the Initial Backfilling Period	lb/ft ²	Flow conditions during the Initial Backfilling Period
Shear Stress during the Initial Overbanking Period	lb/ft ²	Flow conditions during the Initial Overbanking Period
Shear Stress during the Splaying Period	lb/ft ²	Flow conditions during the Splaying Period
Shear Stress during the Peak Flow Period	lb/ft ²	Flow conditions during the Peak Flow Period
Shear Stress during the Earlier Drainage Period	lb/ft ²	Flow conditions during the Earlier Drainage Period
Shear Stress during the Later Drainage Period	lb/ft ²	Flow conditions during the Later Drainage Period
Landform classification from unfiltered floodplain terrain	N/A	Local topographic conditions on the floodplain
Landform classification from unfiltered floodplain terrain ⁹	N/A	
Distance from the Patapsco's main channel	Meters	Geometric conditions on the floodplain
Longitudinal distance downstream	Meters	

⁹ Both unfiltered and filtered *r.geomorphon* outputs were included in regression analyses as a precautionary measure, in the event that there were predictive differences between characterizations.

This study generated several regression trees via the R package *rpart* to further assess the relative ability of hydrogeomorphic, topographic, and geometric conditions on the floodplain towards explaining floodplain sediment texture patterns. Several regression tree designs were utilized, each excluding certain explanatory variables from the full explanatory variable set detailed in Table 2.2. This was designed to distinguish relatively important variables that influence soil texture on broader, entire-floodplain scales from variables that might be more important at finer, sub-floodplain scales. A **series of exploratory questions** intended to guide regression tree design and satisfy research objective 3 from the Introduction chapter were proposed:

- 1. Provided all explanatory variables are included in the analysis, what variables are selected for during regression tree generation? Are the same variables used for regression tree generation across all particle size classes, or do they vary?**
- 2. Given the relationship established in the literature relating longitudinal distance downstream and distance from the main channel to floodplain sediment texture (Hupp, 1982; Osterkamp & Hupp, 1984; Hupp & Osterkamp, 1985; Barker et al., 2009), to what degree can sediment texture spatial patterns be explained when excluding distance-related explanatory variables? With *only* distance-related explanatory variables?**
- 3. Given the relationship established in the literature relating hydrodynamic conditions (i.e. variables related to flow) to floodplain sediment texture (Leopold et al., 1964; Asselman & Middelkoop, 1995; Gergel et al., 2002;**

Hupp et al., 2009; Song et al., 2014), to what degree can sediment texture spatial patterns be explained when excluding flow-related explanatory variables? With *only* flow-related explanatory variables?

- 4. Given the relationship established within the literature relating landforms to floodplain sediment texture (Hupp & Osterkamp, 1985; Gurnell et al., 2012), to what degree can sediment texture spatial patterns be explained when excluding landform-related explanatory variables?**

Following an exploratory analysis of univariate relationships between each explanatory variable and sediment texture class proportions¹⁰, twelve regression tree designs were finally utilized, each excluding a different set of explanatory variables. A detailed list of these regression tree designs along with the series of variables included for each design can be found in Table 2.3. As each sediment texture class (sand, silt, and clay) required a separate regression tree, twelve times three equals thirty-six regression trees in total were generated.

Multivariate regression tree analysis results were later compared to those generated by a “random forest algorithm”. Utilizing machine learning, a random forest algorithm generates hundreds of different regression trees from observations randomly sampled from a larger dataset of observations. The algorithm then averages the number of times individual explanatory variables were selected for over hundreds of generated trees;

¹⁰ Further information on this exploratory analysis, including a table defining the type of univariate relationship established with each numerical explanatory variable and the strength of said relationship, can be found in the Appendices as Table 5.2.

this allows for (a) an assessment of the relative importance of each variable, and (b) a measure of overfitting. Finally, to non-parametrically assess possible correlations among explanatory variables used for the multivariate regression tree analysis, a matrix of Spearman's rho rank correlation coefficients was generated (found in the Appendices chapter, Figure 5.1).

Table 2.3 (next page): All regression tree designs utilized in the regression tree analysis, as well as the explanatory variable set used for regression tree generation for that design. The color scheme design is intended to explain which regression tree designs are related to addressing a given exploratory question. These are as follow: Red = exploratory question #1; Yellow = exploratory question #2; Green = exploratory question #3; Blue= exploratory question #4; Orange = univariate regression trees intended to elucidate further information regarding strong univariate relationships identified in the exploratory univariate analysis between each exploratory variable and sediment texture class proportions.

Table 2.3:

Regression Tree Design	Explanatory Variables Included for Analysis
ALL VARIABLES	Sediment accretion rates; flow conditions (both velocity and shear stress) for all 6 conceptual periods; unfiltered and filtered landform classifications; distance from the main channel; longitudinal distance downstream.
NO DISTANCE-RELATED VARIABLES	Sediment accretion rates; flow conditions (both velocity and shear stress) for all 6 conceptual periods; unfiltered and filtered landform classifications.
ONLY DISTANCE-RELATED VARIABLES	Distance from the main channel; longitudinal distance downstream.
NO FLOW-RELATED VARIABLES	Sediment accretion rates; unfiltered and filtered landform classifications; distance from the main channel; longitudinal distance downstream.
ONLY FLOW-RELATED VARIABLES	Flow conditions (both velocity and shear stress) for all 6 conceptual periods.
NO LANDFORMS	Sediment accretion rates; flow conditions (both velocity and shear stress) for all 6 conceptual periods; distance from the main channel; longitudinal distance downstream.
ONLY SPLAYING VELOCITY	Flow velocity during the splaying conceptual period.
ONLY (Earlier) DRAINAGE VELOCITY	Flow velocity during the earlier drainage conceptual period.
ONLY (Later) DRAINAGE VELOCITY	Flow velocity during the later drainage conceptual period.
ONLY DISTANCE DOWNSTREAM	Longitudinal distance downstream.
ONLY CHANGE IN ELEVATION	Sediment accretion rates.
ONLY DISTANCE FROM CHANNEL	Distance from the main channel.

Chapter 3: Results

Section 1: Quantifying and Mapping Post-Flooding Sediment Accretion

Major differences were identified in the extent and degree of detected sediment accretion and erosion from Tropical Storm Lee between regional and localized minLODs . The regional minLOD DEM of Difference (DoD) was dominated by areas where no reliable sediment accretion or erosion was detected (Figure 3.1, following pages). As the minimum level of detection threshold (minLOD) was increased, however, more areas of reliable sediment accretion or erosion were detected (Figures 3.2 and 3.3, following pages). This culminated in the localized minLOD DoD, where areas of reliable sediment accretion or erosion were found nearly everywhere (Figure 3.4, next page). Across all DEMs of Difference, major sediment deposits ($>0.38\text{m}$ in depth) were detected nearby levees adjacent to the Patapsco's main stem; at lower minLOD thresholds, minor deposits were generally also found adjacent to the Patapsco's main stem, as well as further inland.

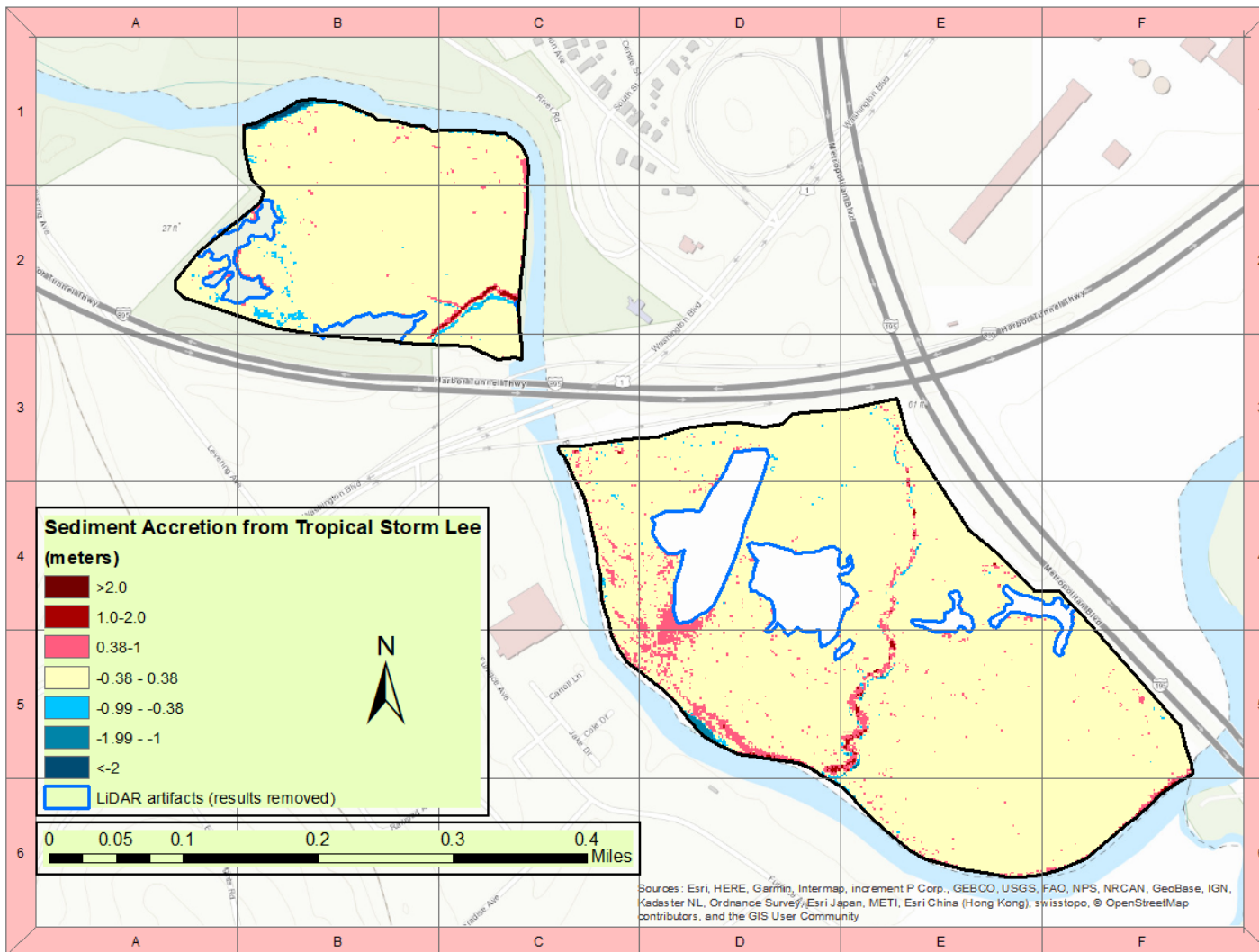


Figure 3.1: Spatial estimates of sediment accretion rates from Tropical Storm Lee, as determined from the 2015-2011 DoD classified from global reference points across county extent (the regional minLOD described in section 1 of the Methods chapter). minLOD was equal to 0.38m.

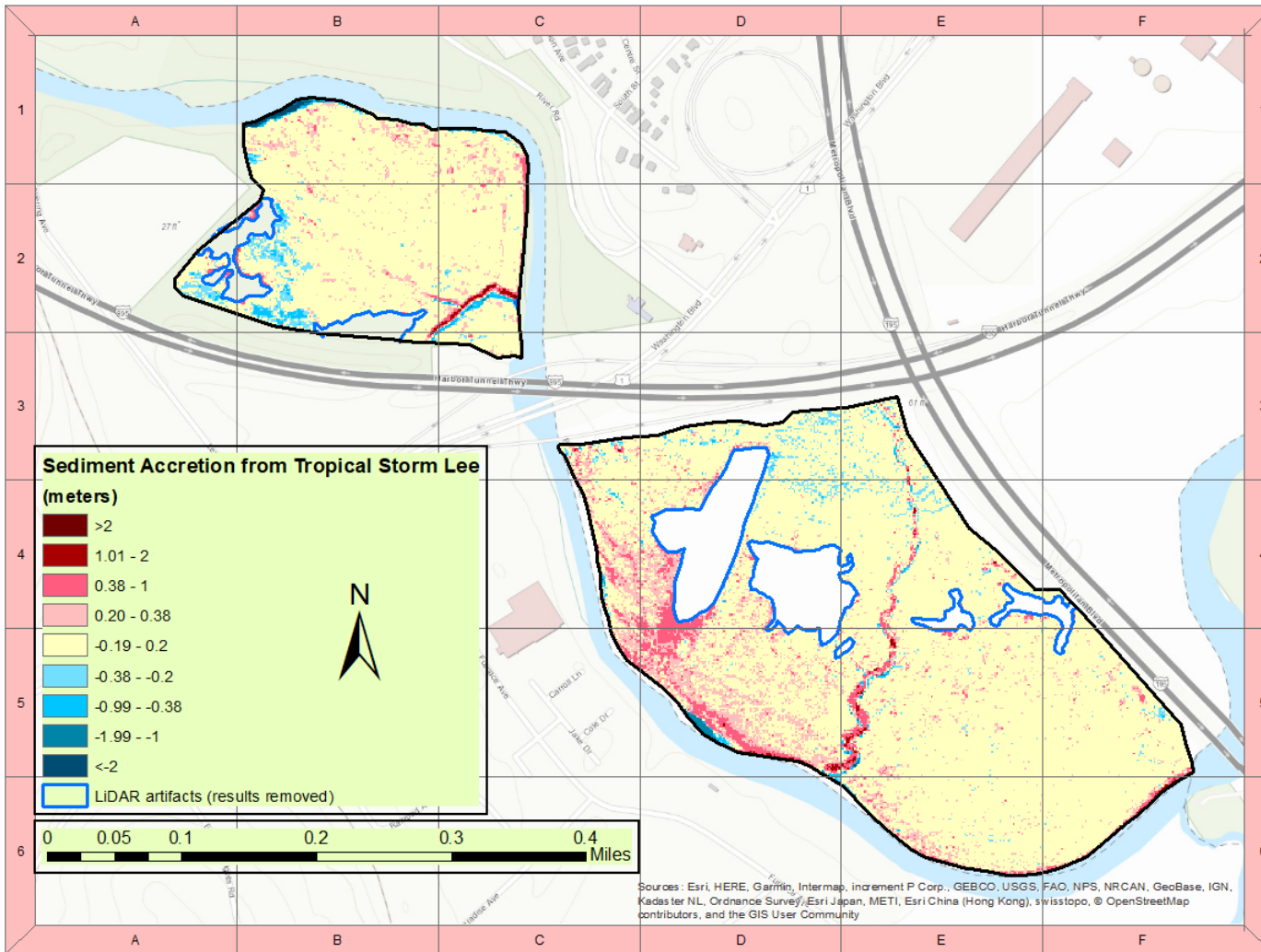


Figure 3.2: Spatial estimates of sediment accretion rates from Tropical Storm Lee, as determined from the 2015-2011 DoD (one of two intermediary thresholds between the localized and regional minLODs described in section 1 of the Methods chapter). minLOD was equal to 0.2m.

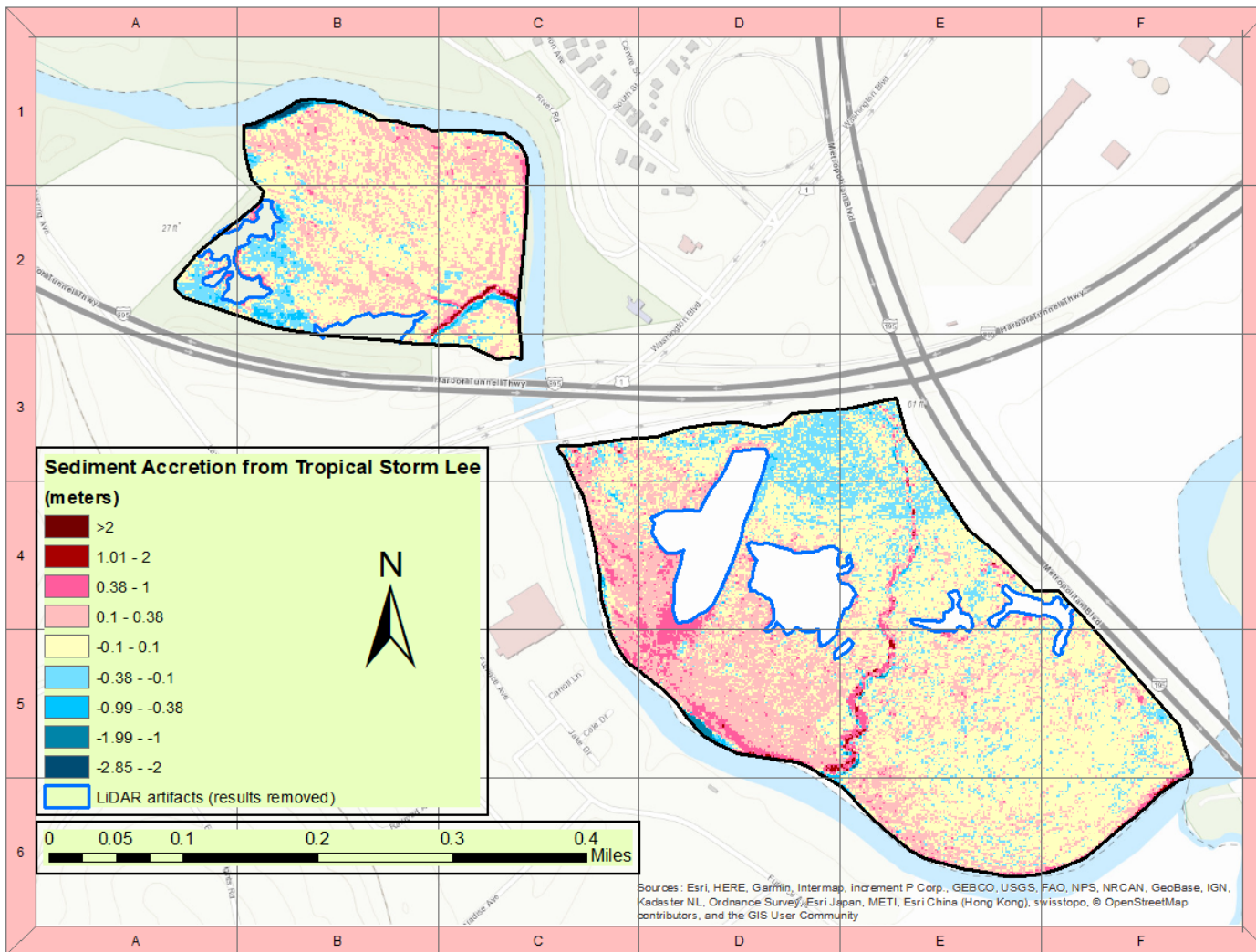


Figure 3.3: Spatial estimates of sediment accretion rates from Tropical Storm Lee, as determined from the 2015-2011 DoD (one of two intermediary thresholds between the localized and regional minLODs described in section 1 of the Methods chapter). minLOD was equal to 0.1m.

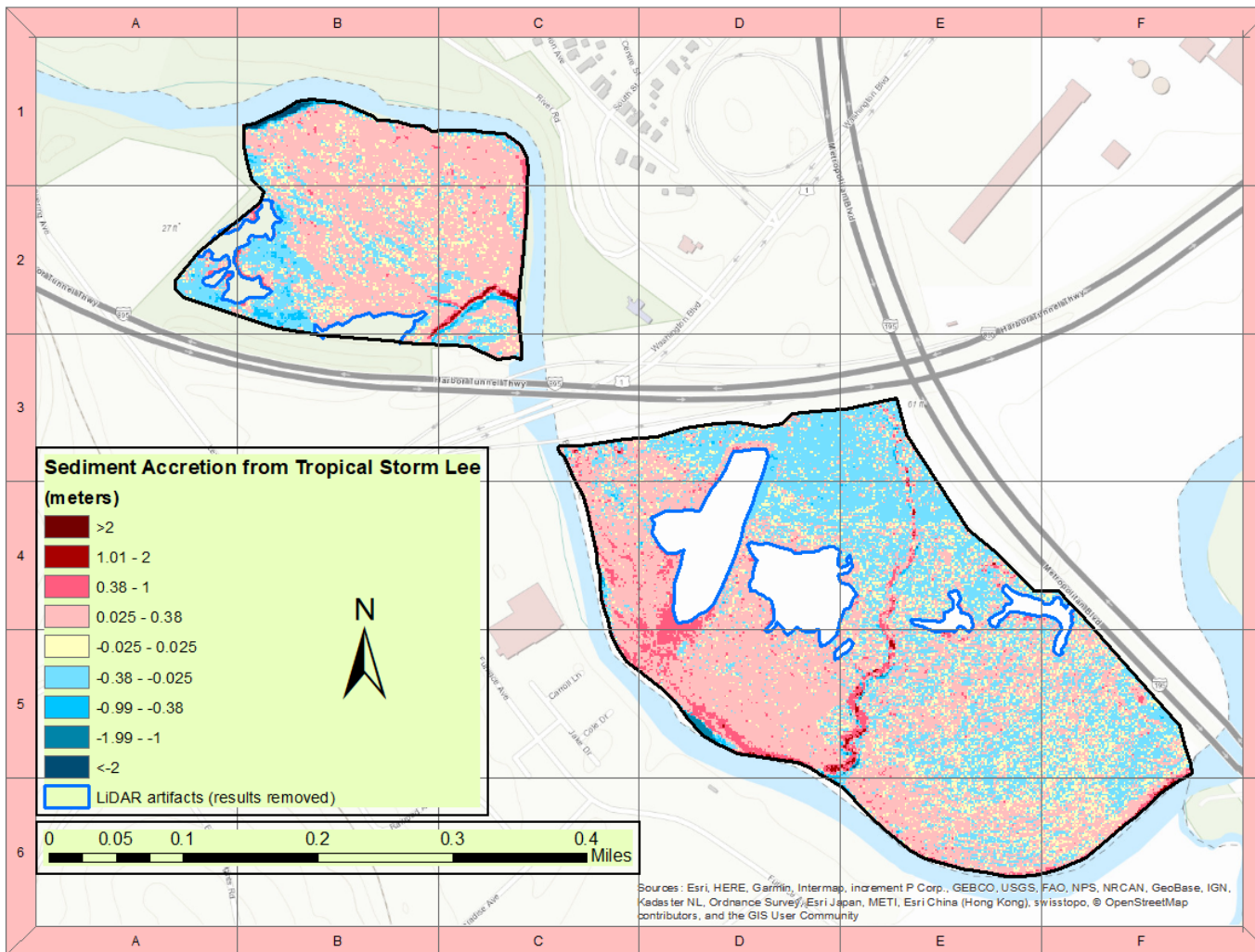


Figure 3.4: Spatial estimates of sediment accretion rates from Tropical Storm Lee, as determined from the 2015-2011 DEM of Difference (DoD) classified from reference points within local extent (the localized minLOD described in section 1 of the Methods chapter). minLOD was equal to 0.025m.

Most sediment deposition detected under the regional minLOD (Figure 3.4) was located adjacent to channel banks, primarily along tributaries intersecting the study area (e.g., grid cells C2, E4, E5) and along the Patapsco's main channel. Further deposits under the regional minLOD were detected immediately downstream of the Rt.1 culvert (grid cell C4), where large sand deposits had been observed during field visits after Tropical Storm Lee. Similarly, large deposits were detected in the DoD along the southern edge of the detention pond (grid cells D4 and D5). While all sediment deposition detected under the regional minLOD was major ($>0.38\text{m}$ in depth), areas of detected deposition were relatively rare.

In contrast, the decreased minLOD threshold under the localized minLOD allowed for both major deposits detected under the regional minLOD to be detected, as well as subtler deposits (Figure 3.1). Many of these same subtler deposits were also detected by the two intermediary minLOD DoDs (Figures 3.2 & 3.3; $\text{minLODs} = 0.1\text{m}$ & 0.2m , respectively), whose minLODs fell between the localized and regional minLODs (0.025m & 0.38m , respectively). Most of the upstream section showed widespread minor deposits ($0.025\text{-}0.38\text{ m}$ in depth), with sparse major deposits ($>0.38\text{ m}$ in depth) clustered around levees along the main stem (e.g., grid cells B1 & C1). Small, noncontiguous areas of no detected deposition or erosion ($-0.025\text{m} - 0.025\text{m}$) were concentrated in the upstream section's floodplain interior (grid cell B2). The distribution of these patches appeared to be stochastic at fine scales ($<50\text{m}^2$).

Under the localized minLOD (Figure 3.1), two distinct patterns emerged relative to the bisecting tributary in the downstream section (found in grid cells E4 & E5). West of the tributary, major deposits ($>0.38\text{m}$ in depth) were identified adjacent to the main channel's banks (grid cell C4) and clustered south of the detention pond (grid cells D4 & D5). Minor deposits (2.5-38cm) were virtually uniform west of the tributary, apart from small patches of minor erosion immediately adjacent to the Patapsco. East of the tributary (grid cells E4, E5, E6, F5, & F6), however, depositional zones were less uniform. Areas of minor deposition were concentrated closer to the main channel (grid cells E6 & F6), however very few major deposits ($>38\text{cm}$) were found near the channel. Within the floodplain interior west of the tributary (grid cells E4 & E5), areas of minor deposition, minor erosion, and areas of no reliably detected change appeared to be stochastically arranged. This mirrored the organizational pattern observed in the interior of the upstream floodplain section (grid cell B2).

Paradoxically, major change ($>38\text{cm}$ of deposition or erosion) was detected within floodplain interiors¹¹ for all DEMs of Difference (grid cells B2, E4, & E5), regardless of minLOD . However, upon examination of LiDAR point clouds and subsequent DEMs it was apparent that artifacts in the point cloud itself led to an unreliable estimate of floodplain topography. As topographic change was utilized as a surrogate for sediment accretion or erosion occurring on the floodplain for this study, this was an issue. This effect was hypothesized to be caused by standing water on the floodplain, as identified in field inspections such as that depicted in Image 1.4. Given the stated difficulty in the

¹¹ Identified as "LiDAR artifacts (results removed)" in figures 3.1 through 3.4.

literature regarding mitigating LiDAR-scattering on water surfaces (Hilldale & Raff, 2008), these subsections were removed from consideration for this study and all subsequent analyses.

Section 2: Characterizing Floodplain Landforms

Distinct macro- and micro-topographic landforms were identified in the *geomorphon*-characterized terrain at both floodplain sections. A chain of convex macro-topographic features (“summits”, “ridges”, and “shoulders”) was identified adjacent to the Patapsco’s main channel, as well as tributaries intersecting the two floodplain sections (Figure 3.5, following page). Visually these convex macro-topographic features appear to correspond generally with many areas that featured major sediment deposition from Tropical Storm Lee, as identified in the previous section (Figures 3.1-3.4).

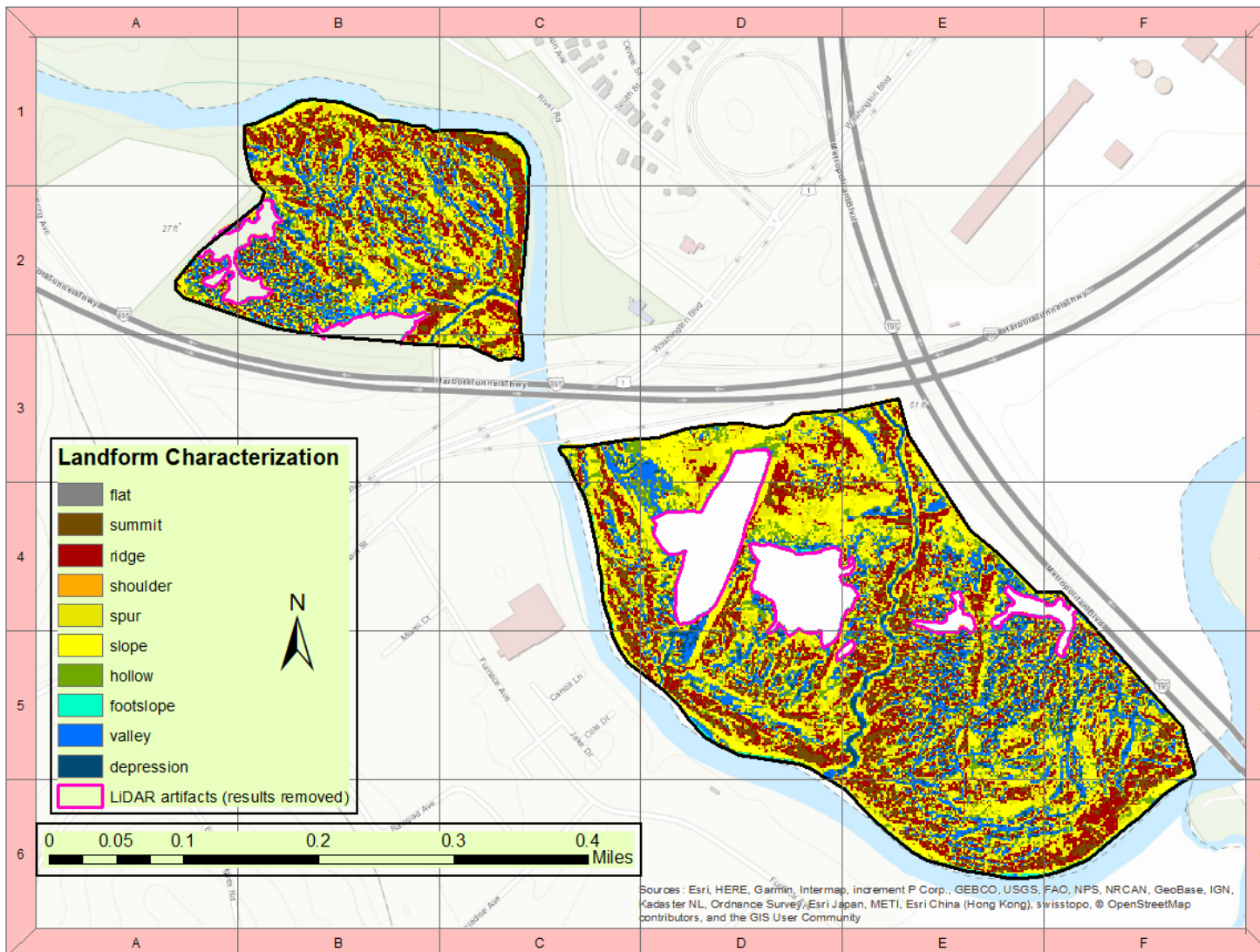


Figure 3.5:
 Landform
 Characterization
 results from
 filtered terrain.

Additionally, a network of concave topographic features (“hollows”, “footslopes”, “valleys”, and “depressions”) was immediately apparent within the interior of the upstream section (Figure 3.5, grid cell B2). This network connected broad-scale convex topographic features along the northern floodplain edge (grid cells B1 & C1) to the backswamp (grid cell B2) and small tributary of the southwestern portion (grid cell C2). The downstream section also featured a distinct network of concave topographic features resembling those observed in the upstream floodplain section’s interior. These networks of concave topographic features were most prevalent east of the bisecting tributary (grid cells E4, E5, E6, F5, & F6), and to a lesser degree west of the bisecting tributary, immediately downstream of the Route 1 culvert (grid cell C4). Finally, convex macro-topography was identified alongside the bisecting tributary (found in grid cells E4 & E5), the pipeline road (found in grid cells E4 & E5), and a rectangular ridge feature to the east of the detention pond (found in grid cell D5). This last feature is presumed to be a previously unidentified former building foundation. Further concave macro-topographic features were identified intersecting with convex features making up the dirt road and building foundation.

Section 3 Modeling Representative Flow Conditions on the Floodplain

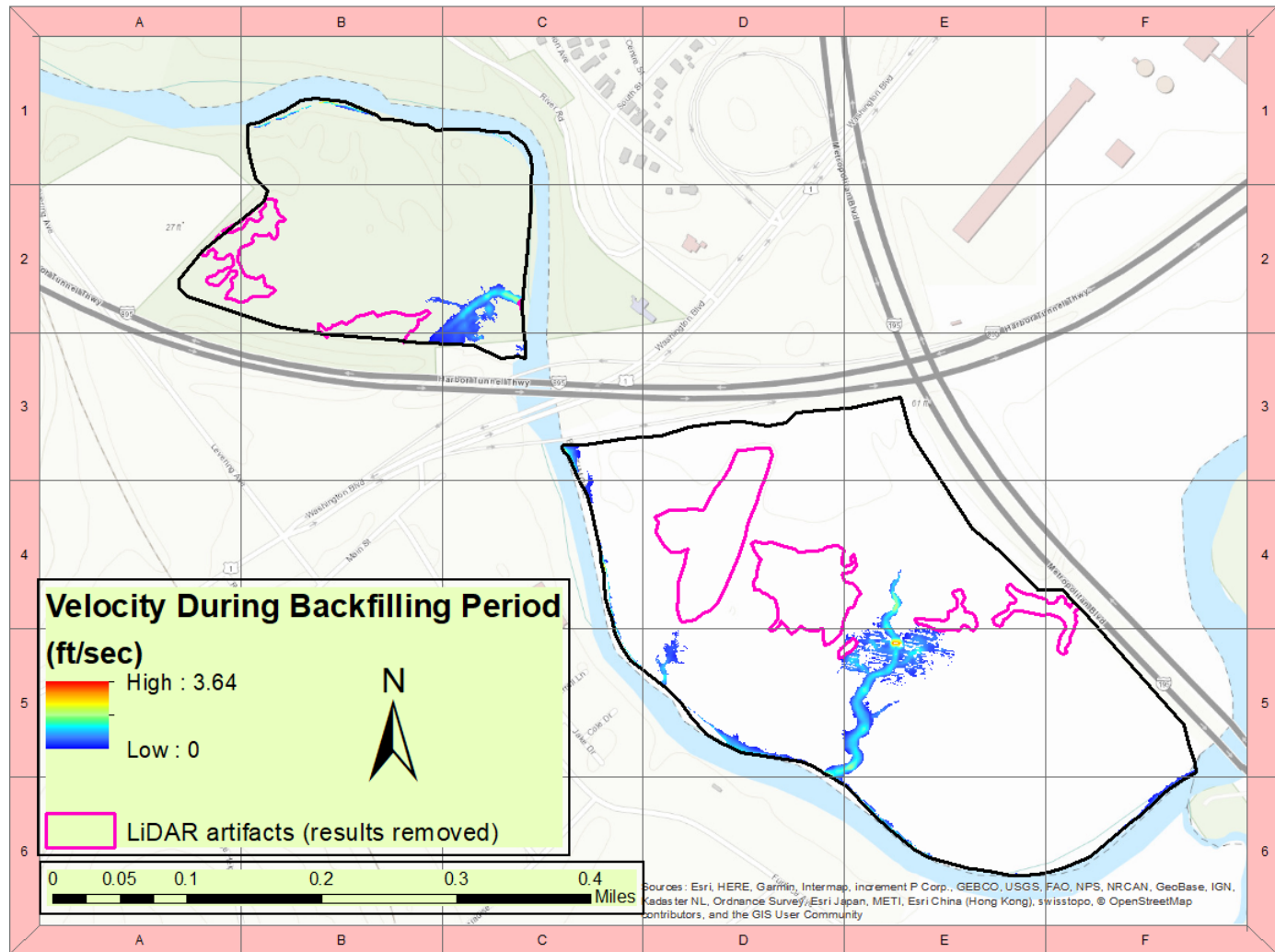
General Note: This section is divided into four sub-sections based on the conceptual periods discussed in section 3 of the methods chapter. This was to allow for interpretative analysis of the flow model’s “narrative” a la Nicholas & Walling (1998) and is organized to minimize the amount of relevant information left out.

Interpretations of overbanking and splaying conceptual periods, as well as the two drainage periods, were combined for sake of clarity. Refer to Figures 3.6-3.11 for all modeled flood extents and flow velocity diagrams for each conceptual period.

Subsection 1: Backfilling Conceptual Period

According to the hydraulic flow model, initial points of entry by floodwaters for both upstream and downstream sections occurred immediately adjacent to tributaries intersecting each floodplain (Figure 3.6, grid cells C2 & E5). Modeled flow directions indicated that floodwaters traveled up the tributaries to where tributary banks could be overtopped, then spread out in all directions. Shortly after these backfilling events (<15 simulated minutes), flow directly from the main channel was observed to overbank levees adjacent to the Patapsco's main channel through a series of localized overbanking events. These events were first observed immediately downstream of the Rt. 1 culvert and south of the detention pond on the downstream section (grid cells C3 & D5), with similar events in the upstream section occurring along the north bank shortly afterward (grid cells B1).

Figure 3.6: Simulated flow velocities during the backfilling conceptual period. Initial backfilling occurs primarily through flooding events centered around drainage tributaries (cells C2 & E5). Minor overbanking events are also observed immediately downstream of the Rt. 1 culvert and due south of the detention pond (cells C3 & D5, however these are extremely localized and not indicative of a larger trend yet).



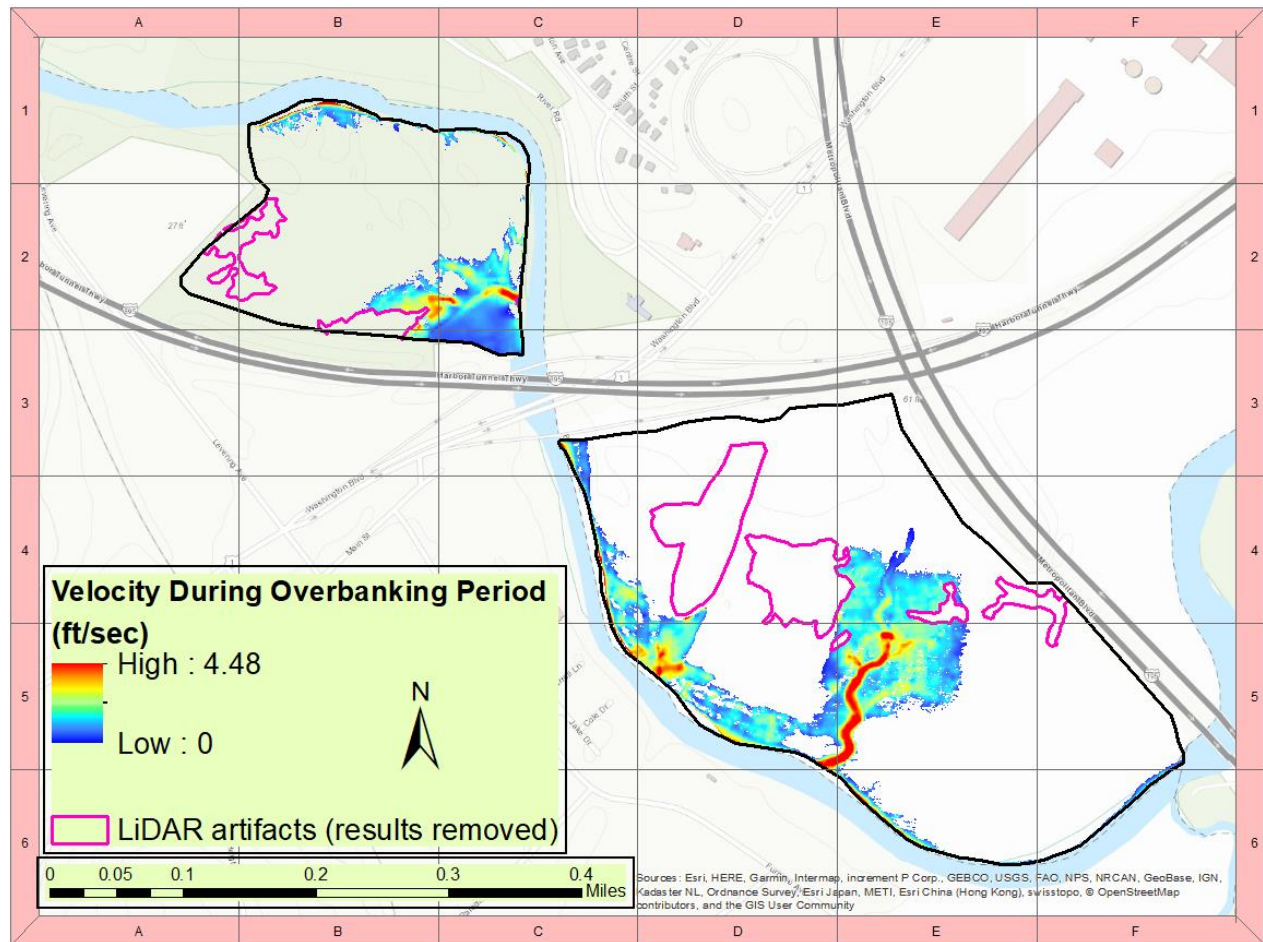
Subsection 2: Overbanking and Splaying Conceptual Periods

As localized overbanking events described in the first subsection were observed to spread into the floodplain interior (Figure 3.7, grid cells E4 & E5), further overbanking events occurred along almost all the main channel's levees (Figure 3.8, e.g. B1 & D5). Floodwaters during this conceptual period generally travelled southeast but with local variations.

In addition to observed variations in flow directionality at this period, there were noticeable local variations in flow velocity. Visual inspection of velocities in HEC-RAS documented local variations in velocity of at least two orders of magnitude. Upon observation of underlying topography for areas of high velocities, the majority were centered on "transitional areas" where flow on the floodplain was being routed through concave features bordered by relatively higher convex features¹². Areas where this phenomenon was observed in the model included the eastern edges and select interior areas of the upstream section (Figure 3.8, grid cell B1). This phenomenon was also observed in the downstream section around the detention pond's southern banks (grid cell D5), and in the concave features bisecting the building foundation's footprint and the dirt road's (footprint = grid cell D5; dirt road = grid cells E4 & E5).

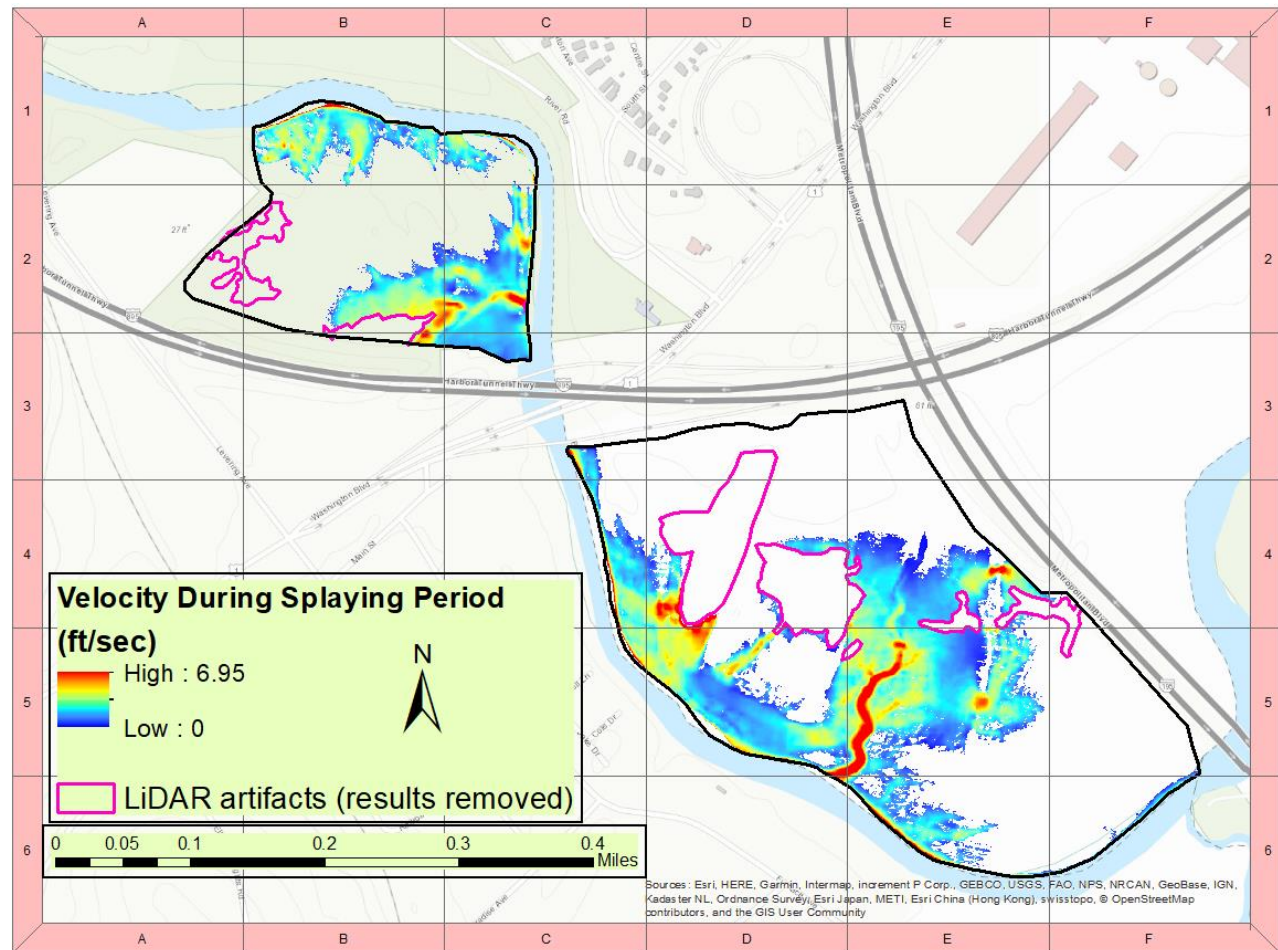
¹² Between half a foot to four feet in elevational difference from the bottommost point of the concave feature to the highest point on the convex feature perpendicular to flow direction.

Figure 3.7: Simulated flow velocities during the overbanking conceptual period. Overtopping of levee features starts occurring during this period, as evidenced by simulated flows entering the floodplain at various points. This may be observed along the northern banks of the upstream section (cell B1), as well as where previous minor overbanking occurred in the previous conceptual period (cells C3 &



D5). As observed later in the simulation, overbanking events occur where floodwaters at peak flow primarily enter the floodplain.

Figure 3.8: Simulated flow velocities during the splaying conceptual period. Floodwaters begin spreading further into the floodplain beyond the previously documented simulated extents. Note the influence of micro- and macro-topography on flow routing, particularly apparent on the northern banks of the upstream floodplain (cell B2) and east of the downstream section's bisecting tributary (cell



E4 & E5). A rapid decrease in velocity as floodwaters travel away from the main channel is observable, exceptions being flow concentrations as a response to topography.

Subsection 3: Peak Flow Conceptual Period

Approximately three hours after the first floodwaters entered the floodplain, peak flow extent and velocity were observed in the hydraulic model. Unlike earlier conceptual periods, variation in local flow velocity and directionality have since disappeared; local variations were replaced by a southeasterly directional trend with minor variations. Minor directional variations appear to be a result of broad-scale topographic features. In contrast to the importance of microtopography guiding flows during earlier conceptual periods (e.g., Figure 3.8 grid cells B1 & D5), these larger features rarely shift flow direction more than fifteen degrees off their general southeasterly heading.

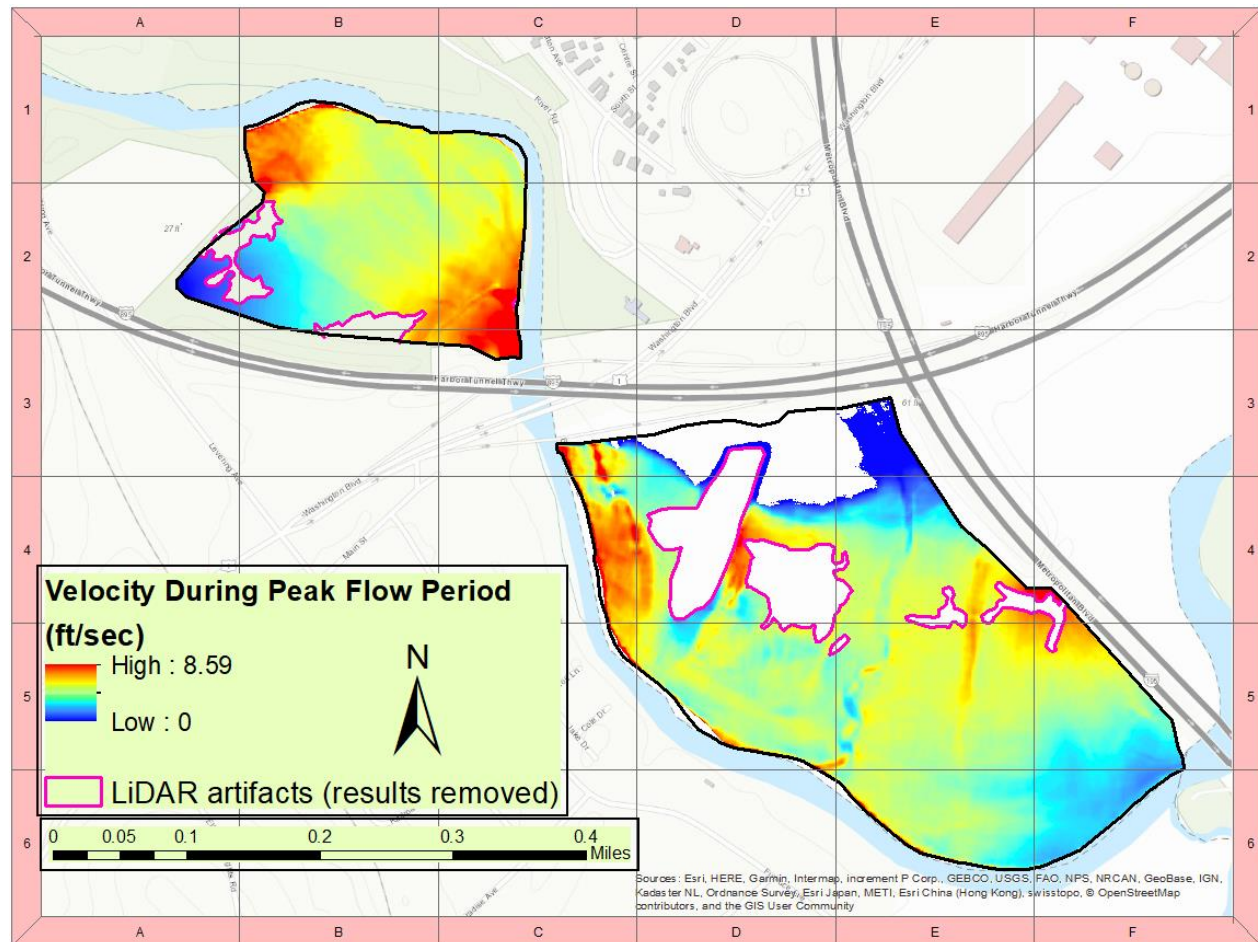
The range of flow velocities observed on the floodplain at peak flow increased compared to earlier periods. Velocities immediately next to the main channel were modeled as high as eight ft/s, particularly so immediately downstream of the Rt. 1 culvert (Figure 3.9, grid cell C3). Velocities near the outermost edges of the flood's simulated extent were virtually zero ft/s (grid cells B2, C3, & E3).

Relatively higher velocities continued to be reported within the convex features described earlier during the splaying period (grid cells B1, D5, E4, & E5). Higher velocities were also identified higher up along the ridges lining these convex features, suggesting that at higher water depths the concentrating effect of local microtopography was muted. This phenomenon was also observed to occur in new areas, notably across the upstream section's interior (Figure 3.9, grid cell B2) and among the

drainage channels associated with some of the more southern levees of the downstream section (grid cell E6).

Finally, a general increase in flow velocity on the downstream section as floodwaters approached and rounded the I-195 embankment was noted (grid cell F5). This appeared to be the result of a gradual flow constriction across the downstream section as the embankment constricted the extent to which floodwaters could spread perpendicular to the main channel.

Figure 3.9: Simulated velocities during the peak flow conceptual period. While micro-topography no longer has a distinct role in influencing flow routing, macro-topographic features still influence the distribution of relatively higher velocities and flow concentrations. “Streaks” of relatively higher velocities are apparent in the upstream section’s interior (e.g. cell B2). The highest simulated flow velocities reported were found immediately downstream of the Rt. 1 culvert (cell C3); the lowest were found in the southwestern portion of the upstream section (cells A2 & B2), where floodwaters appear to be virtually stagnant.



Subsection 4: Earlier and Later Drainage Conceptual Periods

Floodwaters began to drain away a full day after initially entering the floodplain; notably the upstream section began to drain a few hours prior to the downstream section. Furthermore, the downstream section took much longer to drain than the upstream section, likely a result of its larger area and a less distinct topographic gradient. As both sections drained, flow directionality was observed to become more random at fine scales, suggesting the noted influence that microtopography had on fine-scale flow dynamics had returned.

Figures 3.10: Simulated flow velocities during the earlier drainage conceptual period. The description of observed phenomena for this figure is also applicable to Figure 3.11 (following page). Micro-topography again plays a major role in determining drainage routes alongside macro-topographic features. This is apparent in both earlier and later drainage periods in the upstream section, particularly along the northern edge (cell B1). This same phenomenon is observed in the downstream section, where local topographic constraints on flow are visible immediately south of the dirt road (cell E6) and within the building foundation's footprint (cell D5).

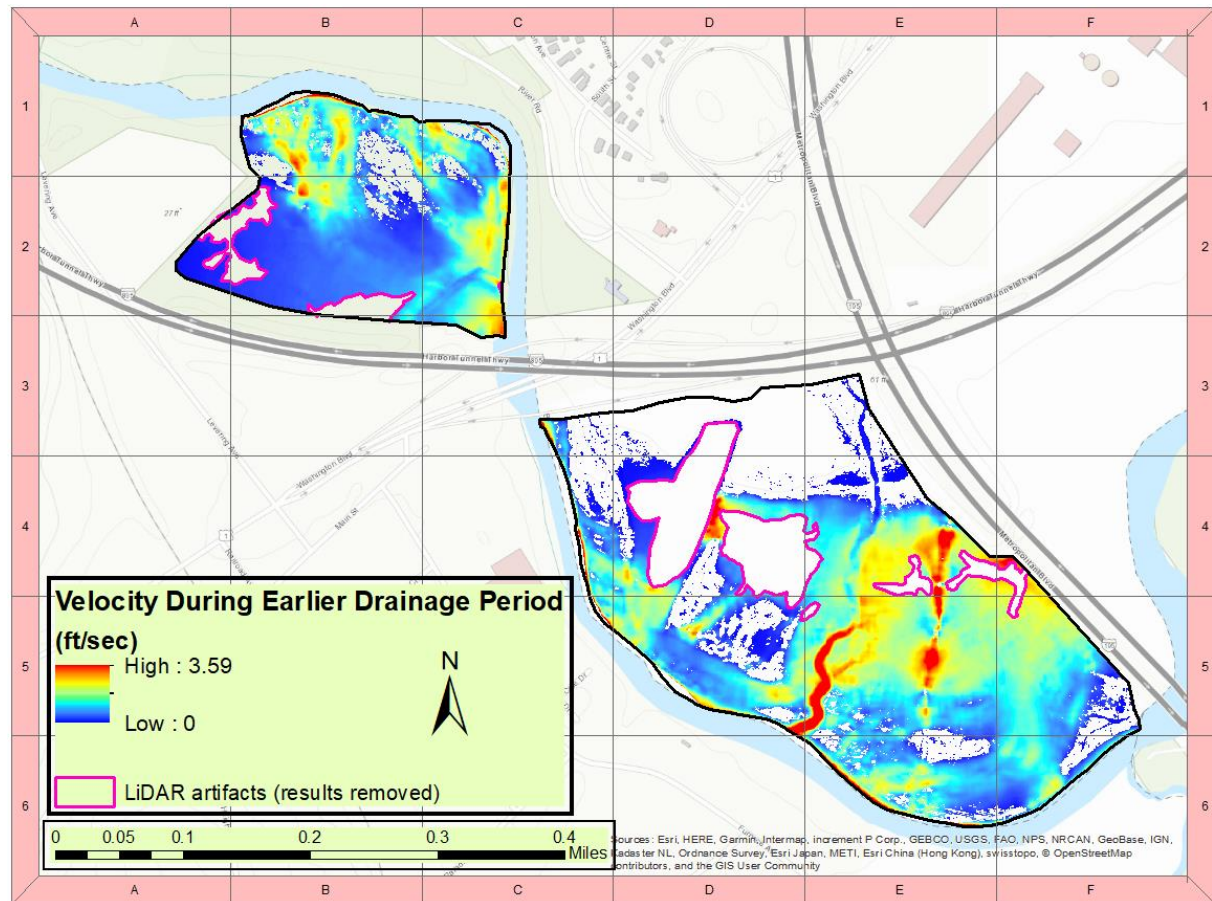
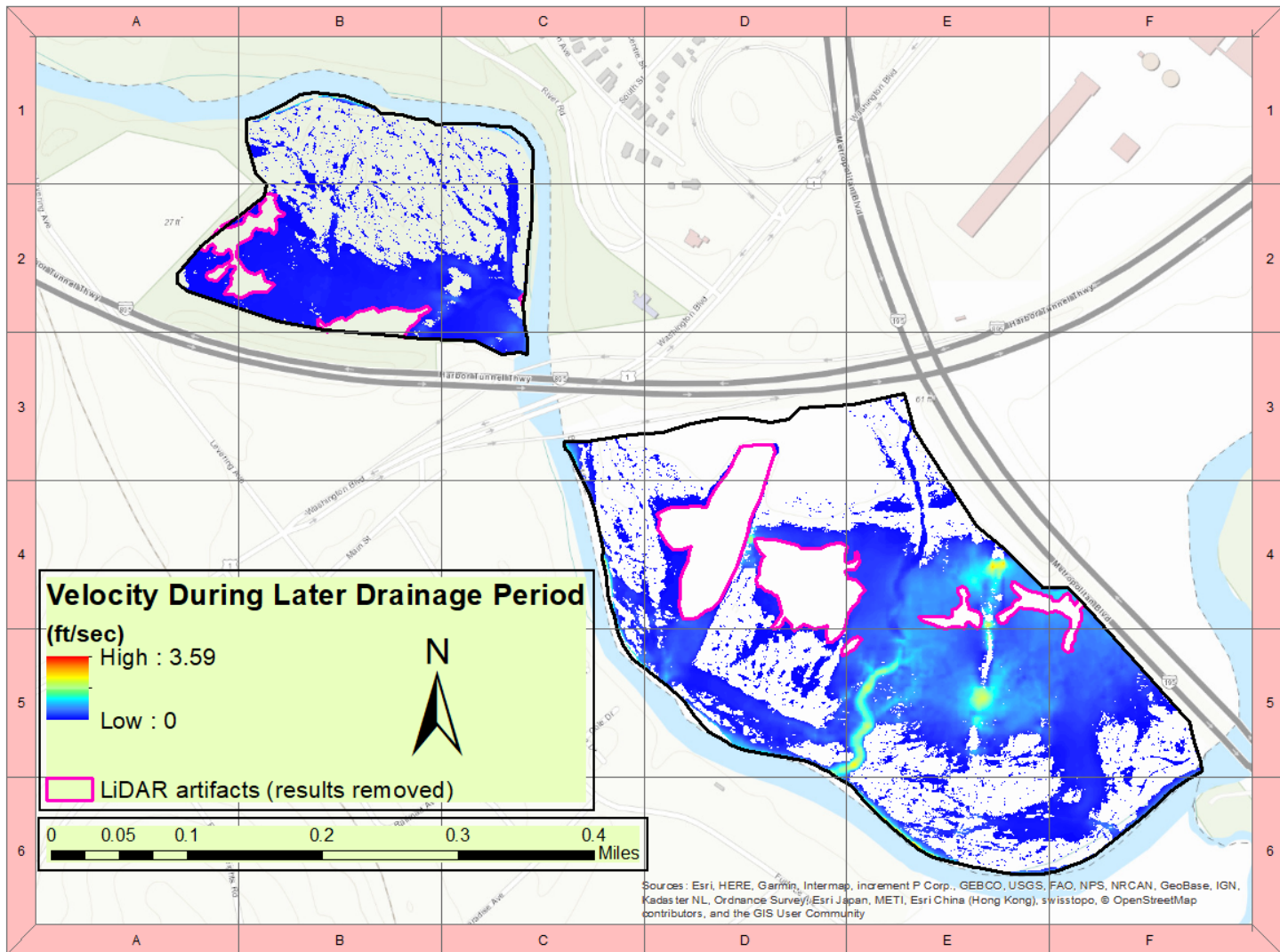


Figure 3.11:
 Simulated flow
 velocities during
 the later drainage
 conceptual period.
 For full description
 of observed
 phenomena, see
 Figure 3.10
 description.

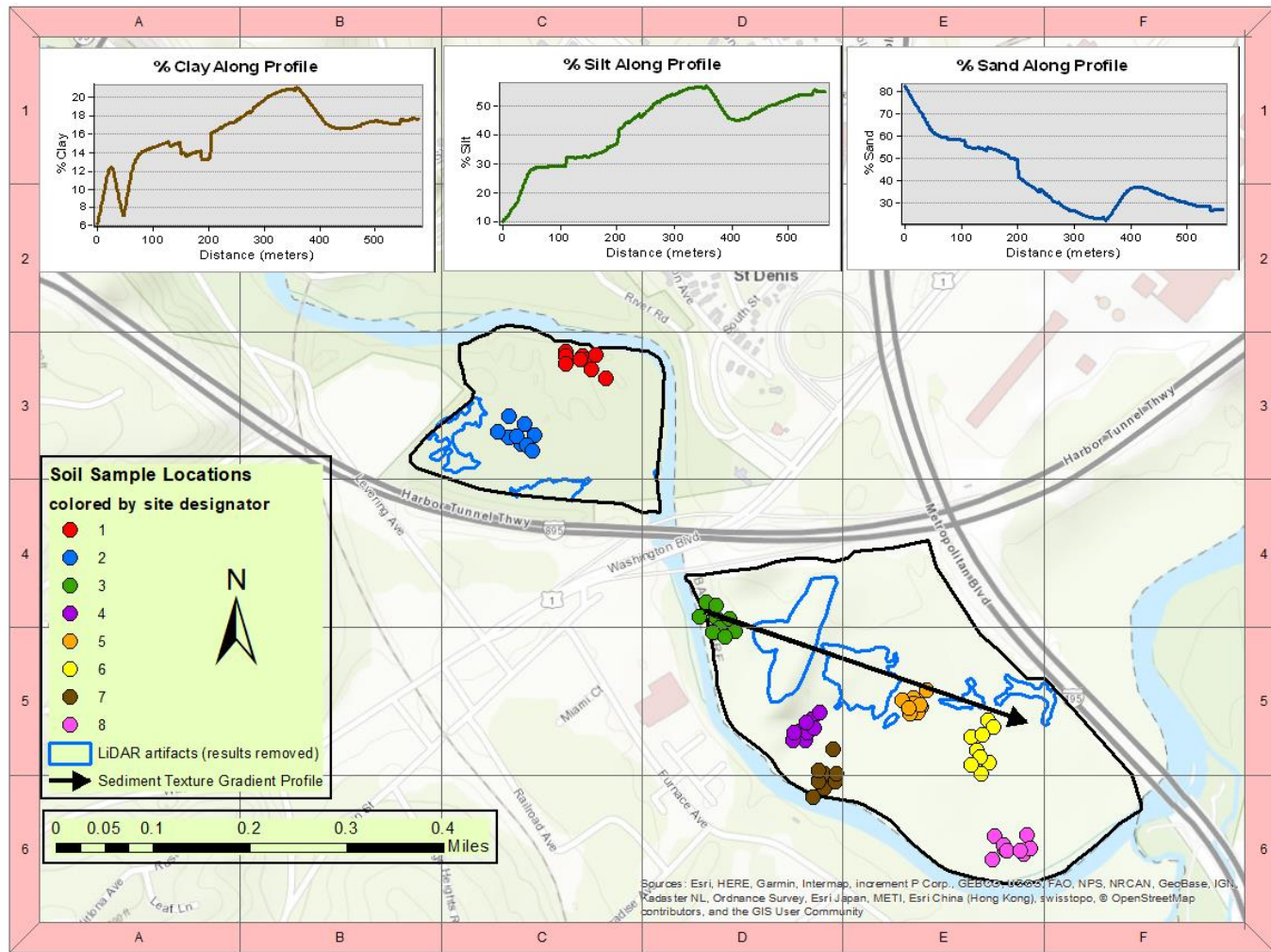


Section 4: Quantifying Sediment Characteristics for the Study Floodplain

The sediment sampling campaign and subsequent particle size analysis identified distinct spatial trends in sediment texture across both floodplain sections. Spatially interpolated sediment texture results depicted a general fining gradient as one travelled inland for both floodplain sections. Coarse sand particles were found in their highest proportions closest to the Patapsco's main channel and shrank in proportion as one moved away from the channel (figure 3.12, on following page). A similar but reversed trend was observed for finer particle proportions, such as silts and clays.

Likewise, a similar fining gradient was observed as one travelled downstream, i.e. coarse sand particles were found in higher proportions upstream relative to downstream. However, unlike the previously described gradient, this gradient was most pronounced for the downstream floodplain section. Again, a similar but reversed trend was observed for finer particle proportions, such as silts and clays (figure 3.12, specifically the plots depicting sediment size class proportions along the transect).

Figure 3.12: Graphical representation of the sediment texture gradients shared across the three particle size classes. The floodplain gradient depicted in the three plots lies across the downstream section as a black arrow-transect and runs from the Rt. 1 culvert (cell D4) to the I-195 embankment (cell E5)



The gradients observed in the spatially interpolated results were later corroborated by ternary plot results (Figure 3.13, below). Inter-site particle size distribution trends were very pronounced in the ternary plot of samples. The overall gradient observed in the ternary plot for both sections centered on a distinct sand to silt transition, especially given the lack of major variation in clay concentrations between sites. Notably there was a minor increase in clay concentrations as silt concentrations increase, alongside a decrease in clay concentrations as sand concentrations increase. Sampling sites closest to the main channel (e.g., site 3) generally featured higher sand concentrations within the ternary plot; Site 8 is an exemption to this trend. Despite its proximity to the channel, its particle size distribution compares to that of Sites 5 and 6.

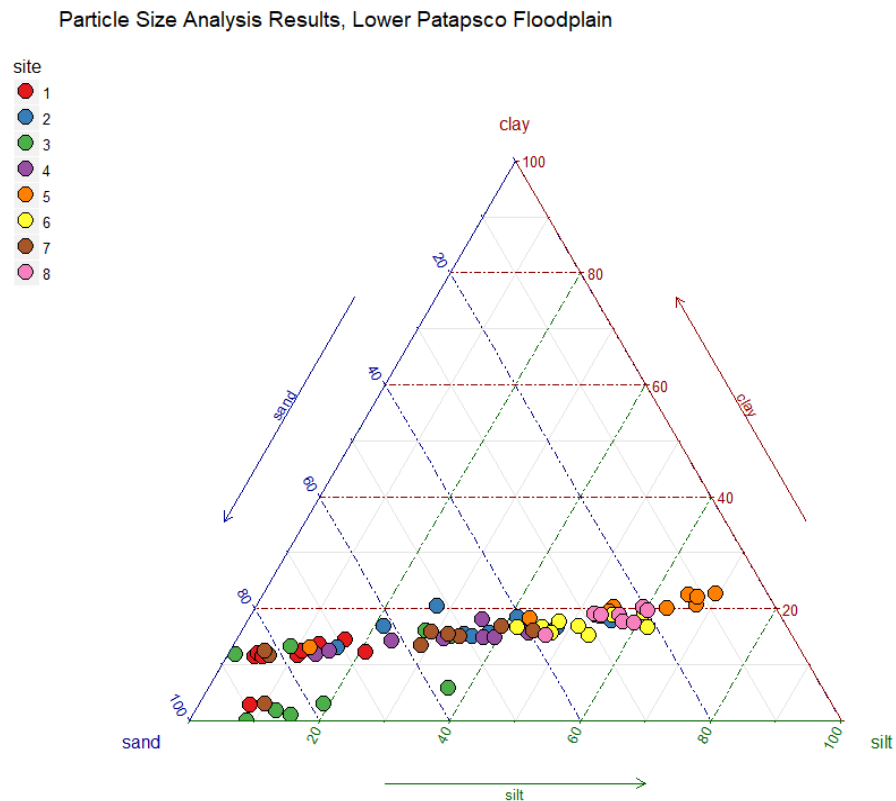


Figure 3.13: Ternary diagram of floodplain sediment texture across sites.

Of the overall gradients observed, the silt and sand sediment texture gradients for the upstream section were the most extreme, ranging from approximately 3%-55% and 89%-26% respectively as one traveled inland (figures 3.15 & 3.16, respectively). Mimicking the upstream section, silt and sand gradients were again the most extreme gradients downstream, reporting ranges of 1%-70% and 91%-7% respectively along comparable spatial orientations. In contrast, the clay gradients for the upstream and downstream sections were much narrower, ranging from 2%-20% and ~0%-22% respectively (figure 3.14).

Figure 3.14:
 Interpolation results
 of particle size
 distribution for
 percent clay.

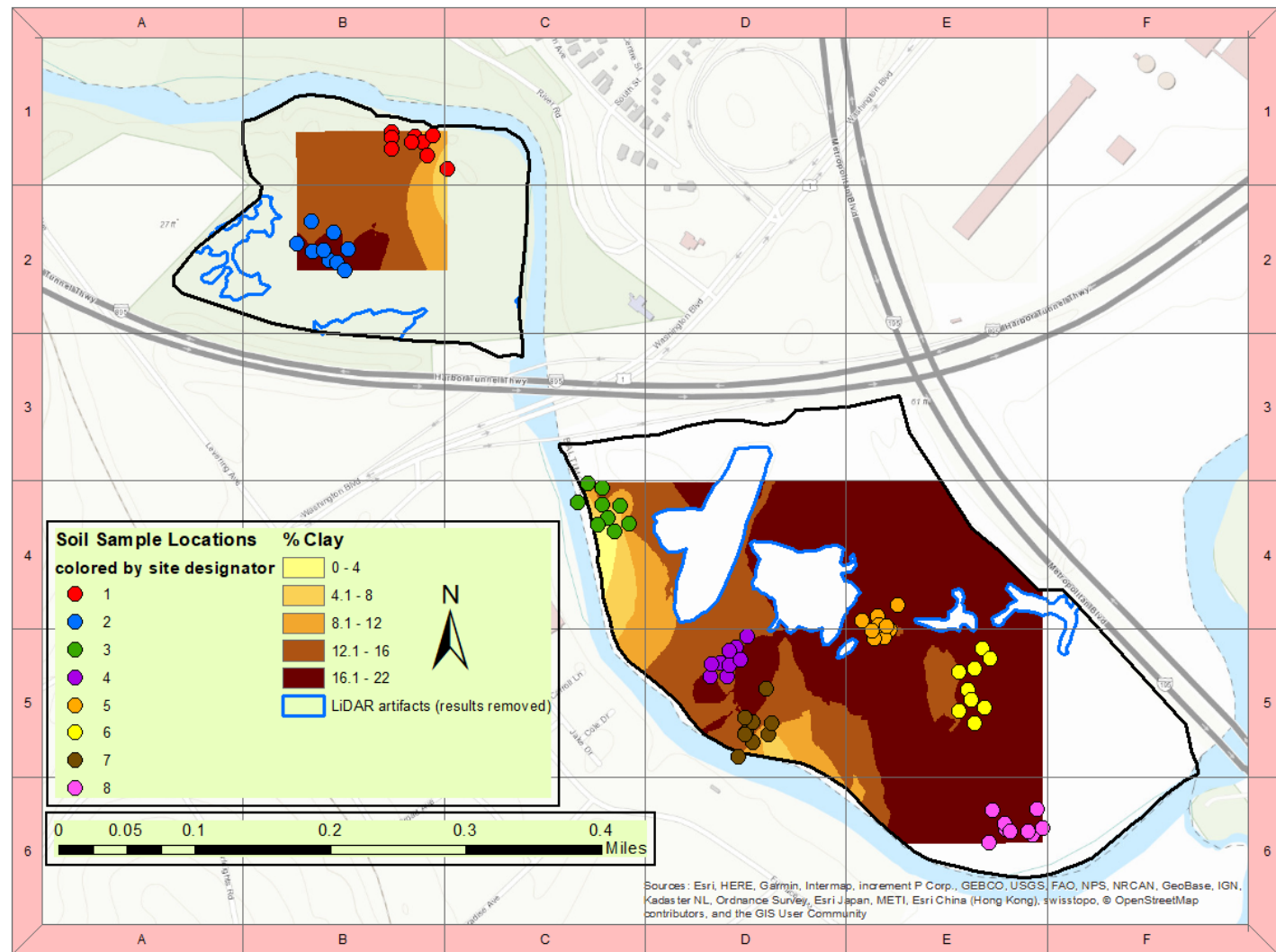


Figure 3.15:
 Interpolation results of
 particle size distribution
 for percent silt.

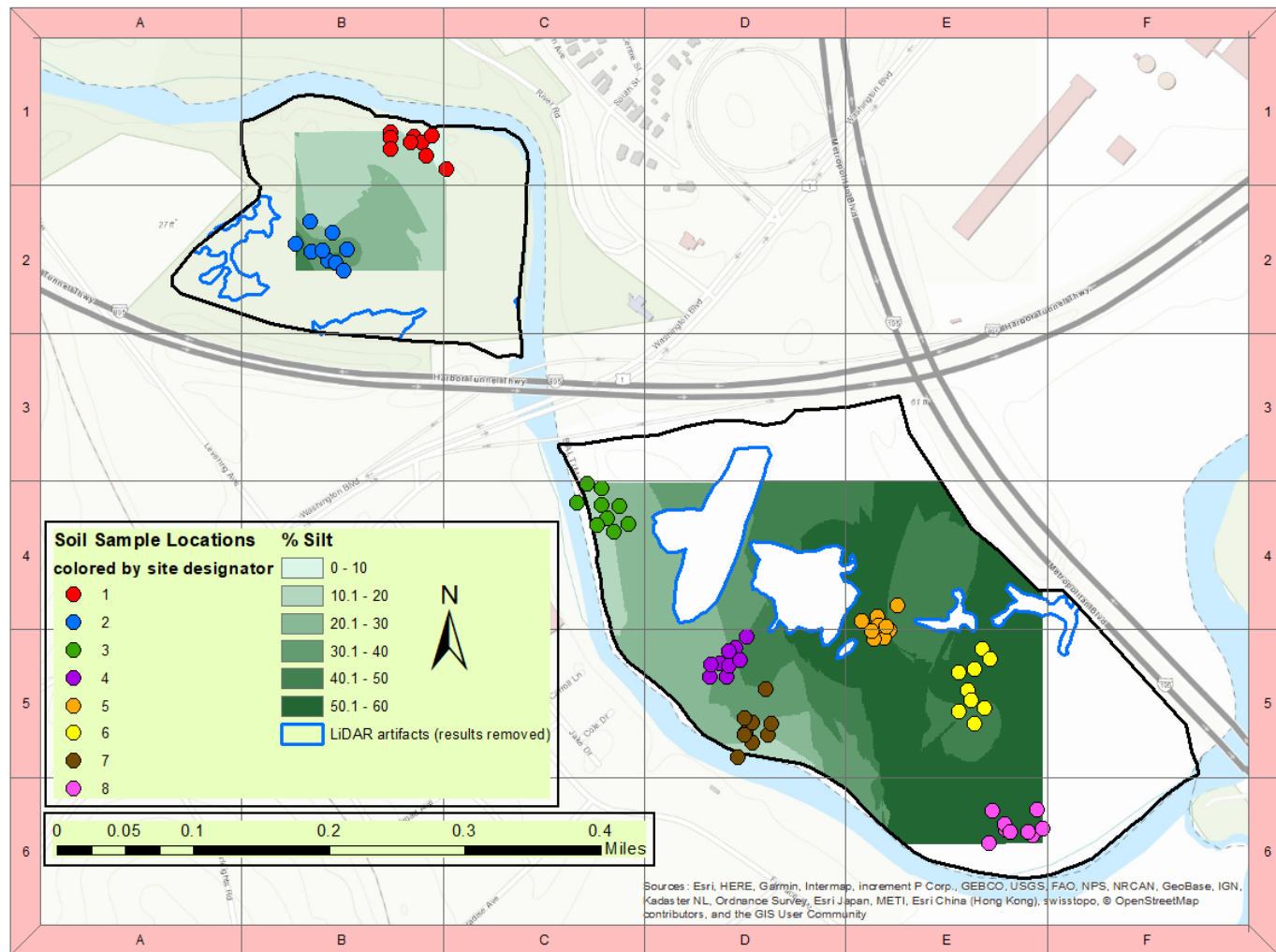
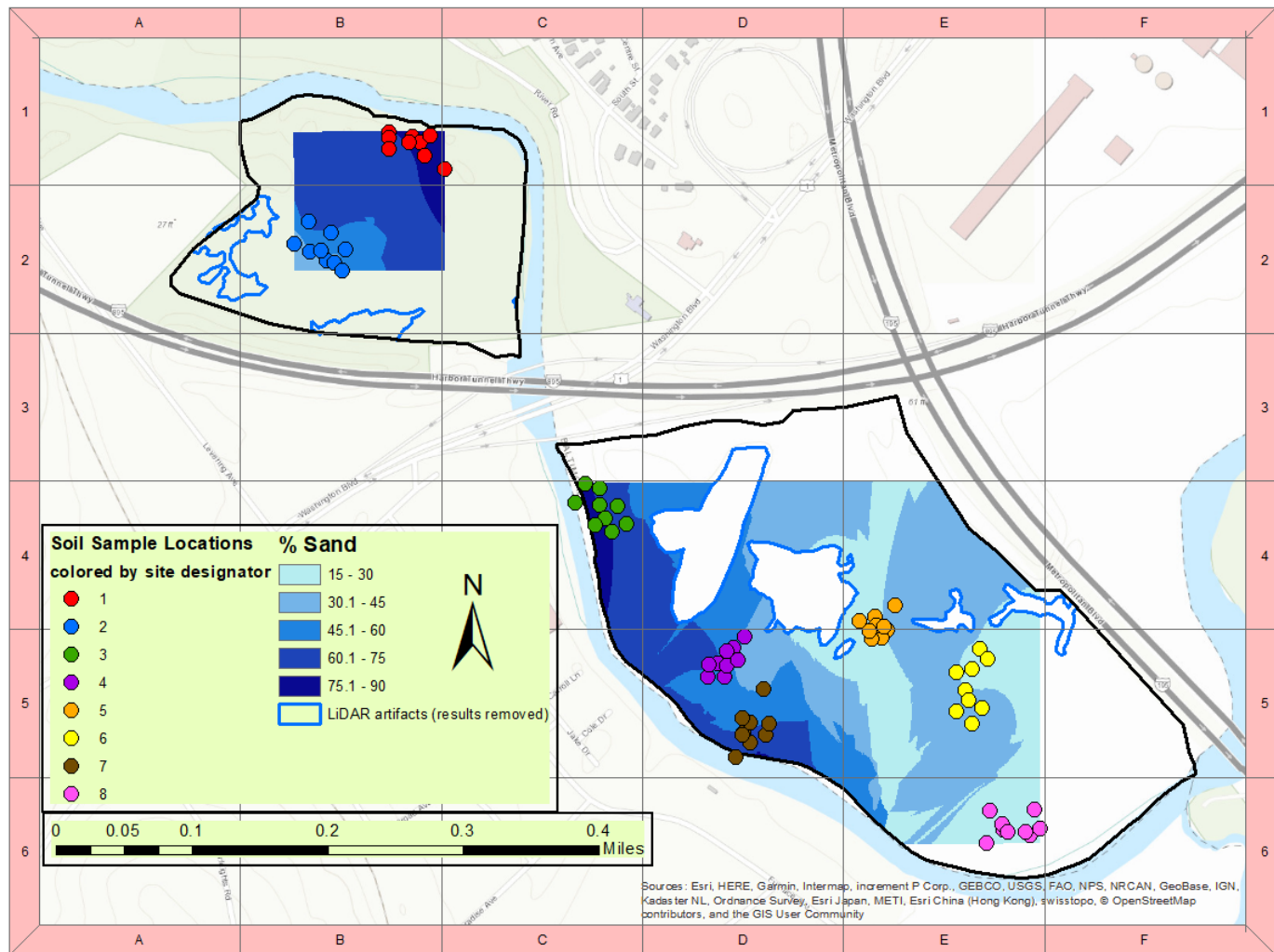


Figure 3.16:
 Interpolation results of
 particle size distribution
 for percent sand.



Section 5: Assessing the Relative Importance of Hydrogeomorphic, Topographic, and Geometric Conditions in Explaining Spatial Patterns of Floodplain Sediment Texture

To read a regression tree: The primary node of a regression tree is the first branching path; for the regression tree explaining the spatial variation in the clay proportion of a sediment sample in Figure 3.17, for example, this would be distance from the Patapsco's main channel. Nodes are then named as they descend from this primary nodal split, the following two nodes on the next level are referred to as "secondary nodes", the next level down "tertiary nodes", etc. The row of colored values at the bottom of the regression tree are the proportional values of a given sediment size class expected with the above conditions defined at each nodal level. For example, to return to the clay regression tree, the darkest orange circle at the bottom reads 20. This means that for a sediment sample collected from a location satisfying the defined conditions:

- distance from the Patapsco's main channel $\geq 129\text{m}$ [**the primary node**]
- velocity during the later drainage period $\geq 0.005\text{ft/s}$ [**the secondary node**]
- AND velocity during the overbanking period $\geq 0.65\text{ft/s}$ [**the tertiary node**]

We would expect that sample to be ~20% clay.

Subsection 1: Guiding Question #1- All Explanatory Variables

Provided all explanatory variables are included in the analysis, what variables are selected for during regression tree generation? Are the same variables used for regression tree generation across all particle size classes, or do they vary?

When all explanatory variables were included during regression tree analysis, 59% to 69% of all variation in sediment texture spatial patterns was explained (Figure 3.17, following page). Distance from the main channel and velocity during the earlier drainage period were the predominant explanatory variables at the primary node. Other explanatory variables selected for at secondary and tertiary nodes included longitudinal distance downstream, as well as velocity and shear stress during the splaying period. Regression trees generated utilizing this all-inclusive explanatory variable set explained the most variation. As regression trees generated utilizing the explanatory variable set that omitted landforms was nearly identical to this set, the fourth guiding question concerning landforms' role in explaining sediment variation was considered effectively answered by this regression tree set.

Of regression trees generated utilizing the all-inclusive explanatory variable set, sand distribution was marginally more explainable than silt distribution (69.21% vs 68.73%). Sand distribution was consistently the most predictable particle size class across all regression trees, however at times silt distribution was virtually as predictable or slightly more. Clay distribution was consistently the least predictable across nearly all regression trees.

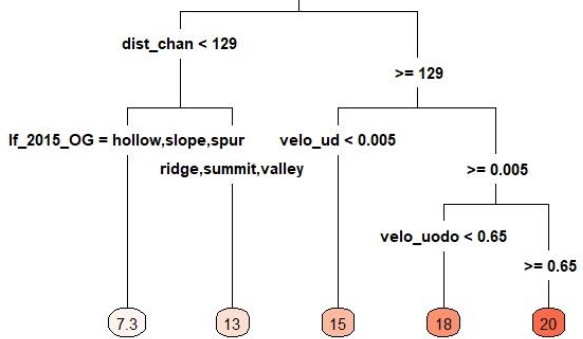
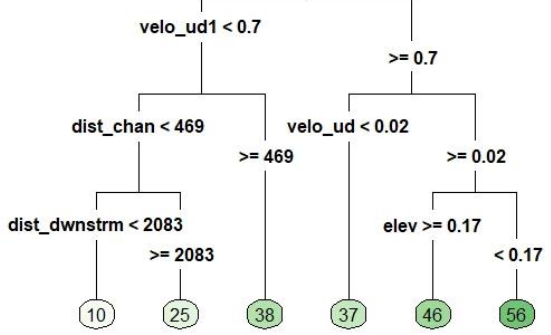
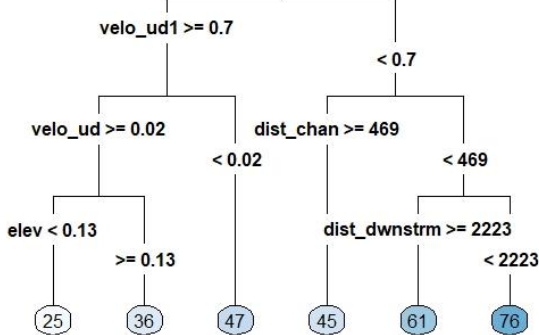
Particle Size Class	Regression Tree
<p style="text-align: center;">Clay</p> <p style="text-align: center;">$R^2=0.5895$</p>	
<p style="text-align: center;">Silt</p> <p style="text-align: center;">$R^2=0.6873$</p>	
<p style="text-align: center;">Sand</p> <p style="text-align: center;">$R^2=0.6921$</p>	

Figure 3.17: Regression trees generated from the all-inclusive explanatory variable regression tree design set. For explanations on what variable each abbreviation references, refer to Table 3.1 (following page).

Table 3.1: Full list of explanatory variables, their abbreviations, and conditions represented.

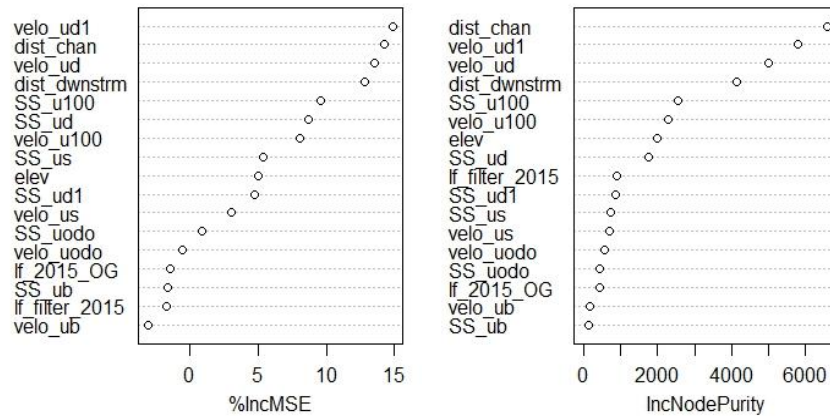
Input (Explanatory) Variables	Variable Abbreviation	Condition Represented
Change in elevation between 2011 and 2015	elev	Sediment accretion rates
Flow Velocity during the Initial Backfilling Period	velo_ub	Flow conditions during the Initial Backfilling Period
Flow Velocity during the Initial Overbanking Period	velo_uodo	Flow conditions during the Initial Overbanking Period
Flow Velocity during the Splaying Period	velo_us	Flow conditions during the Splaying Period
Flow Velocity during the Peak Flow Period	velo_u100	Flow conditions during the Peak Flow Period
Flow Velocity during the Earlier Drainage Period	velo_ud1	Flow conditions during the Earlier Drainage Period
Flow Velocity during the Later Drainage Period	velo_ud	Flow conditions during the Later Drainage Period
Shear Stress during the Initial Backfilling Period	SS_ub	Flow conditions during the Initial Backfilling Period
Shear Stress during the Initial Overbanking Period	SS_uodo	Flow conditions during the Initial Overbanking Period
Shear Stress during the Splaying Period	SS_us	Flow conditions during the Splaying Period
Shear Stress during the Peak Flow Period	SS_u100	Flow conditions during the Peak Flow Period
Shear Stress during the Earlier Drainage Period	SS_ud1	Flow conditions during the Earlier Drainage Period
Shear Stress during the Later Drainage Period	SS_ud	Flow conditions during the Later Drainage Period
Landform classification from unfiltered floodplain terrain	lf_2015_OG	Local topographic conditions on the floodplain
Landform classification from unfiltered floodplain terrain	lf_filter_2015	
Distance from the Patapsco's main channel	dist_chan	Geometric conditions on the floodplain
Longitudinal distance downstream	dist_dwnstrm	

Similar results were found when compared to those produced by the *randomforest* algorithm. Distance from the main channel and velocity during the earlier drainage period were consistently reported as the most significant variables in variable importance plots (Figure 3.18 below shows the variable importance plot for explaining sand variation; variable importance plots for clay and silt variation can be found in the appendices as Figures 5.2 & 5.3). However, flow conditions during the splaying period were less utilized when compared to their relative importance at secondary and tertiary nodes produced during the multivariate regression tree analysis. Instead, flow conditions during peak flow and the later drainage period were relatively more important. A decrease in percent variation explained was noted across all sediment texture classes (47%-57% as opposed to 59%-69%); sand was again consistently the most predictable particle size class and clay the least.

Figure 3.18:

Variable Importance Plot, Sand

Sand variable
importance plot
generated from
a randomforest
regression tree
algorithm.



Subsection 2: Guiding Question #2 – Distance-related Explanatory Variables

Given the relationship established in the literature relating longitudinal distance downstream and distance from the main channel to floodplain sediment texture, to what degree can sediment texture spatial patterns be explained when excluding distance-related explanatory variables? With only distance-related explanatory variables?

When all explanatory variables except distance-related variables were included, regression tree analysis explained 55%-65% of all particle size distribution variation (Figure 3.19, following page). Regression trees of sand particle size explained the most variation (65%), while the clay particle size trees explained the least (55%). Flow-related explanatory variables dominated across all nodes. Velocity during the earlier drainage period was featured as the primary node across all particle size classes for this series of regression trees. Notably, the primary nodal split partitioning the full dataset utilized the same value for velocity across all particle size classes (0.7ft/s). Velocity during peak flow and velocity during the later drainage period were selected for at the secondary node. Unlike the primary node, values used at the secondary nodal split to partition the dataset were not the same across all particle size classes.

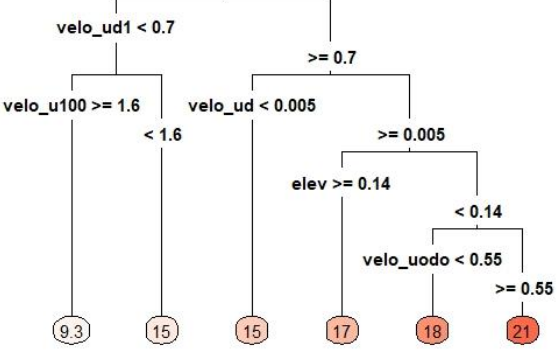
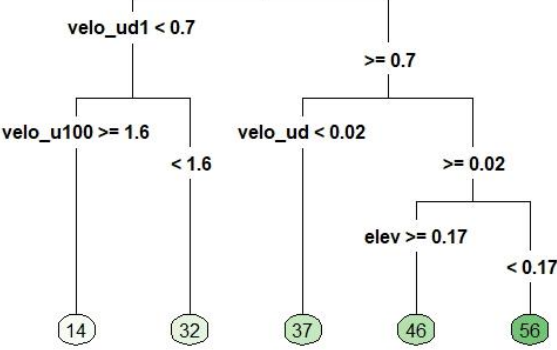
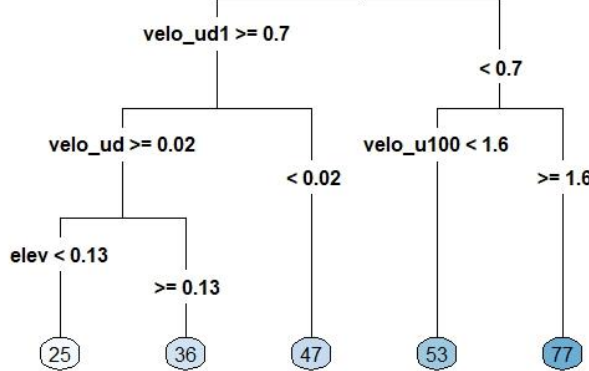
Particle Size Class	Regression Tree
Clay $R^2=0.5531$	
Silt $R^2=0.6332$	
Sand $R^2=0.6534$	

Figure 3.19: Regression trees generated from the explanatory variable set that excluded distance-related variables. For explanations on what variable each abbreviation references, refer to Table 3.1.

The decrease in variation explained between all-inclusive regression trees and those generated when excluding distance-related explanatory variables was on average 5%. As such, it appeared that distance-related explanatory variables weren't necessary for explaining sediment texture spatial patterns. However, this is not to state that distance-related explanatory variables were unimportant or vestigial; merely that other explanatory variables were equally capable of explaining similar amounts of variation. When only distance-related explanatory variables were included in the explanatory variable set (Table 3.2, at the end of the Results chapter), regression tree analysis explained 54%-64% of all variation. The decrease in variation explained between all-inclusive regression trees and regression trees that included only distance-related variables was on average ~5%. As such, regression trees generated *solely* from distance-related variables still explained a large degree of variation in sediment texture spatial patterns.

Subsection 3: Guiding Question #3 – Flow-related Explanatory Variables

Given the relationship established in the literature relating hydrodynamic conditions (i.e. variables related to flow) to floodplain soil texture, to what degree can sediment texture spatial patterns be explained when excluding flow-related explanatory variables? With only flow-related explanatory variables?

When all explanatory variables except flow-related variables were included, 60% to 62% of all variation in particle size distribution was explained by regression tree analysis (Figure 3.20, following page). Distance from the main channel was selected for at the primary node of all regression trees, however distance-related and landform-related explanatory variables were evenly split across all remaining nodes. Notably, the primary nodal split partitioned the dataset with the same value across all particle size classes (129 meters). Regression trees of this series predicting clay and sand distribution were virtually tied for explaining the most variation.

Particle Size Class	Regression Tree
<p style="text-align: center;">Clay</p> <p style="text-align: center;">$R^2=0.61875$</p>	
<p style="text-align: center;">Silt</p> <p style="text-align: center;">$R^2=0.6026$</p>	
<p style="text-align: center;">Sand</p> <p style="text-align: center;">$R^2=0.6131$</p>	

Figure 3.20: Regression trees generated from the explanatory variable set that excluded flow-related variables. For explanations on what variable each abbreviation references, refer to Table 3.1.

Like the relative importance of distance-related explanatory variables, flow-related variables were not necessary for generating a good predictive assessment of particle size distribution. The difference in variation explained between all-inclusive regression trees and regression trees that omitted flow-related variables was on average 10%. Again, this is not to state that flow-related explanatory variables were unimportant or vestigial; merely that other explanatory variables were equally capable of explaining similar amounts of variation. When solely including flow-related explanatory variables (Table 3.2, at the end of the Results chapter), 56% to 64% of all variation in particle size distribution was explained; this was an average decrease of 5% when compared to regression trees generated from the all-inclusive explanatory variable set. When only flow-related explanatory variables were included, notably no flow-related variables for either backfilling or overbanking periods were selected for at any nodes.

Subsection 4: Comparing Univariate and Multivariate Regression Tree Analyses

Several flow-related variables were identified as strong predictors during exploratory univariate linear and logarithmic regressions (see Table 5.2 for more information), and were regularly selected for at primary nodes during the above multivariate analyses. However, many of these same flow-related variables failed to explain similarly large amounts of variation in univariate regression trees (Table 3.2, at the end of the Results chapter). For example, a logarithmic regression relating velocity during the splaying period to sediment texture classes explained on average 87% of variation in sediment texture spatial distribution at the study site (Table 5.2 in the Appendices chapter). In contrast, a univariate regression tree utilizing velocity during the splaying period as its sole explanatory variable explained only on average 16% of variation (Table 3.2). Not all flow-related variables that explained large amounts of variation during the exploratory regression analyses exhibited extreme differences; however, almost all explained less variation when singled out for univariate regression tree analysis.

In contrast, non-flow-related variables¹³ that explained large amounts of variation during exploratory univariate linear and logarithmic regressions (see Table 5.2 for more information) generally explained *more* variation in their respective univariate regression tree. For example, a linear regression of longitudinal distance downstream explained on average ~24% of variation (Table 5.2); in contrast, a univariate regression

¹³ distance-related variables and elevational change

tree utilizing longitudinal distance downstream as its sole explanatory variable explained on average ~60% of variation (Table 33.2, following page).

Table 3.2: Percent variation explained for each regression tree.

Regression Tree Design	Clay	Silt	Sand	Explanation of Regression Tree Design
ALL METRICS	58.95%	68.73%	69.21%	Sediment accretion rates; flow conditions (both velocity and shear stress) for all 6 conceptual periods; unfiltered and filtered landform classifications; distance from the main channel; longitudinal distance downstream.
NO DISTANCE METRICS	55.31%	63.32%	65.34%	Sediment accretion rates; flow conditions (both velocity and shear stress) for all 6 conceptual periods; unfiltered and filtered landform classifications.
ONLY DISTANCE METRICS	53.84%	63.76%	64.16%	Distance from the main channel; longitudinal distance downstream.
NO FLOW METRICS	61.88%	60.26%	61.31%	Sediment accretion rates; unfiltered and filtered landform classifications; distance from the main channel; longitudinal distance downstream.
ONLY FLOW METRICS	55.40%	62.36%	64.41%	Flow conditions (both velocity and shear stress) for all 6 conceptual periods.
ONLY SPLAYING VELOCITY	19.72%	13.09%	15.47%	Sediment accretion rates; flow conditions (both velocity and shear stress) for all 6 conceptual periods; distance from the main channel; longitudinal distance downstream.
ONLY (EARLIER) DRAINAGE VELOCITY	44.44%	51.28%	51.38%	Flow velocity during the splaying conceptual period.
ONLY (LATER) DRAINAGE VELOCITY	30.24%	42.42%	42.45%	Flow velocity during the earlier drainage conceptual period.
ONLY DISTANCE DOWNSTREAM	51.13%	65.27%	65.49%	Flow velocity during the later drainage conceptual period.
ONLY CHANGE IN ELEVATION	34.69%	37.49%	37.26%	Longitudinal distance downstream.
ONLY DISTANCE FROM CHANNEL	46.31%	52.01%	54.31%	Sediment accretion rates.
NO LANDFORMS	56.44%	68.73%	69.21%	Distance from the main channel.

Chapter 4: Discussion

Section 1: Quantifying and Mapping Post-Flooding Sediment Accretion

Critical information about the spatial arrangement and magnitude of sediment deposits following a major storm event was revealed by aerial LiDAR topographic differencing. Large deposits (>0.38 m in depth) were reliably detected according to regional estimates of surface representation uncertainty. Regional estimates identified deposits that trended predominantly sand-based according to field texture-by-feel observations and later particle size analysis. Such deposits were identified primarily near areas of presumed high magnitude flow events (i.e., channel-adjacent), later confirmed by the hydraulic model. Similarly, large deposits of comparable composition were detected by regional uncertainty estimates in areas featuring distinct, highly-recognizable broad-scale (>100 m²) topography (e.g. levees).

In contrast, localized estimates detected both predominantly sand *and* predominantly silt deposits according to field observations and particle size analysis results. In addition to large-magnitude deposits detected by regional estimates, localized estimates detected low-magnitude deposits (<0.38 m) in the floodplain interior. Low-magnitude deposits detected by localized estimates were found in areas of presumed low-magnitude flood activity and subtler topography, later confirmed by the hydraulic model and landform characterization analysis. These low-relief, gentler-

flow areas contrasted with areas of pronounced topography and high-magnitude modeled flows near large-magnitude deposits detected by the regional estimate.

The above qualitative assessments suggest a relationship between particle size and elevational change, along with further potential relationships to topographic and hydrogeomorphic conditions. This is reinforced by the multivariate regression tree analysis results, and mirrors results reported by Marriott (1992) and especially Steiger & Gurnell (2002). Marriott observed a distinct gradient in sediment texture as distance from the channel increases; similar results were observed by Steiger & Gurnell, with an additional (albeit weak) relationship identified linking larger deposits to coarser sediments.

Steiger & Gurnell's 2002 study reported R^2 values of 0.320 when developing a linear regression between sediment texture and mean dry weight deposition (effectively sediment accumulation from a single-storm event). This study reported similar R^2 values ranging from 0.2 to 0.48 during exploratory logarithmic regression analyses (Table 5.2), and nearly identical R^2 values to Steiger and Gurnell's when sediment accretion was used univariately to predict sediment texture via a regression tree analysis (Figure 4.1, following page). This is despite that Steiger & Gurnell's study was located nearly four thousand miles away in south-central France, and that the drainage area of their study's river was an order of magnitude greater than the Patapsco's.

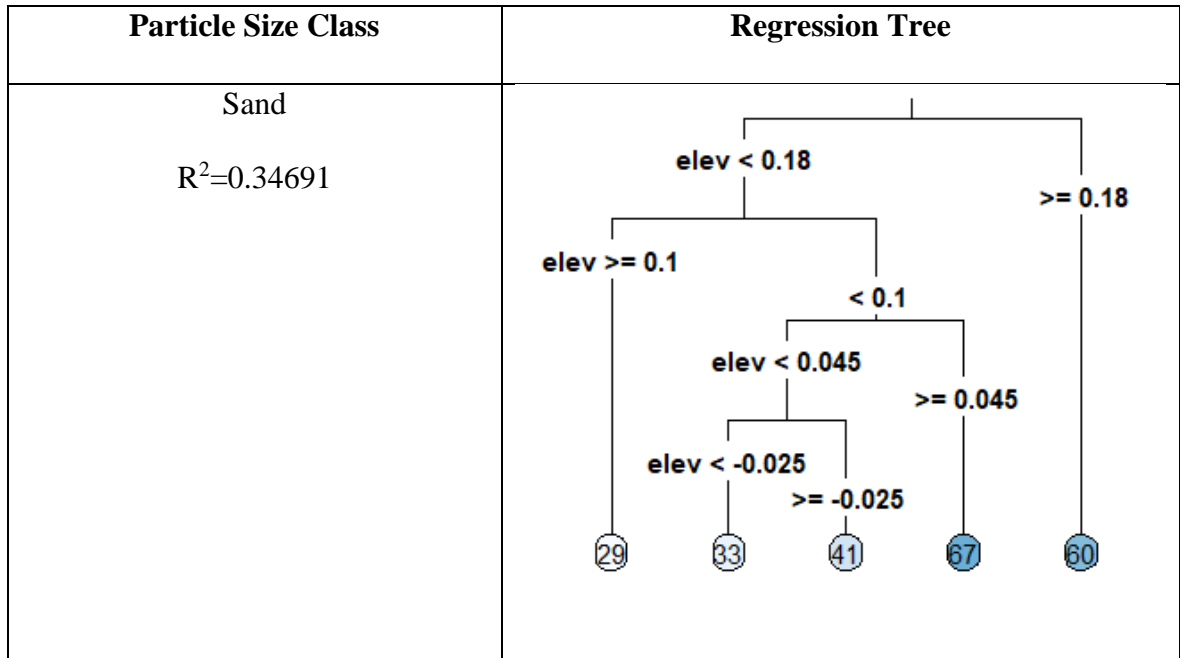


Figure 4.1: Univariate regression tree predicting sand proportions in sediment samples, generated from the explanatory variable set of only sediment accretion rates. Trees predicting clay and silt proportions explained approximately 37% and 35% of spatial variation for their respective sediment size classes.

As documented in Figure 4.1 this relationship was not strong, and better sole predictors of floodplain sediment texture distribution exist (such as flow hydraulics or geometric measures). This assessment was further reinforced by variable importance plots for each sediment texture size class, where several explanatory variables (including those used by Steiger and Gurnell in 2002) are shown to be selected for over sediment accretion patterns (Figure 4.2, following page).

Variable Importance Plot, Sand

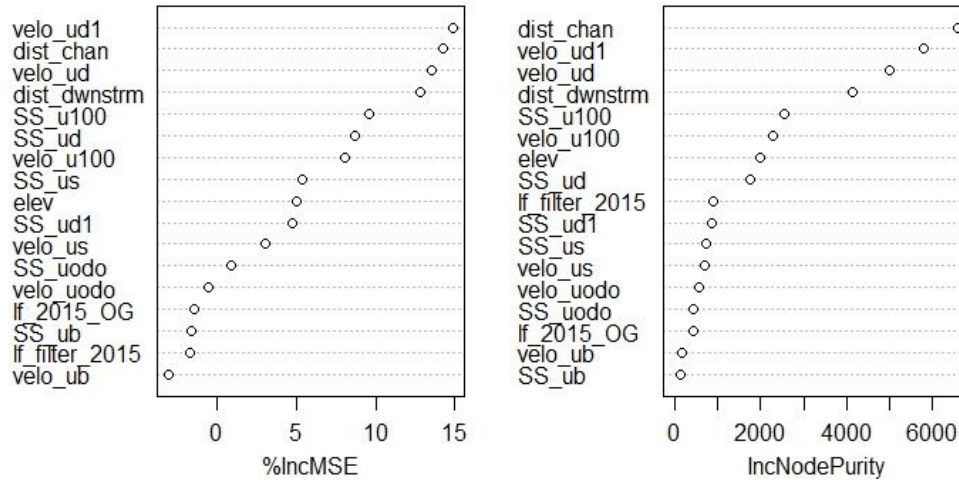


Figure 4.2: Sand variable importance plot generated from a randomforest regression tree algorithm.

Of note is that nearly the same results as Steiger and Gurnell (2002) were obtained without controlling for just deposition associated with a single-flooding event; deposit depths detected by topographic differencing for Tropical Storm Lee ranged from 0m to >1m but sediment cores were collected to a depth of 6" (0.15m). It is possible that some sample cores, particularly those in high-magnitude depositional areas, sampled solely from deposits associated with Tropical Storm Lee. For others in low-magnitude depositional areas, several years-to-decades of storm deposits may have been included in the sample taken. This suggests that floodplain sediment texture sampled this way, barring extreme events, can be a function of long-term hydrogeomorphic and/or geometric conditions just as much as single-storm events.

Finally, localized estimates of surface representation uncertainty provided valuable supplemental information. Low-magnitude depositional patterns¹⁴ depicted by localized estimates mimicked low-magnitude deposits theorized to occur on floodplain interiors during floods by ecologists and hydro-geomorphologists (Walls et al., 2005; Unger & Muzika, 2008; Minnesota Department of Natural Resources, 2016). As such, deposits that previously would have gone undetected in comparable literature's methodologies (Wheaton et al., 2010; Milan, 2012; Thompson & Croke, 2013; Bangen et al., 2014) could now arguably be estimated. The localized methodology used for this study is uncorroborated by the literature, and likely unrealistic given that it sampled unvegetated roads instead of vegetated areas presumed to not change in elevation. Further research is needed to assess its validity.

However, similar depositional patterns to those observed with the localized methodology were observed within the two intermediary DEMs of Difference ($\text{minLOD} = 0.1\text{m} \ \& \ 0.2\text{m}$; Figures 3.2 & 3.3) that fell between the localized and regional minLODs . This suggests that depositional patterns documented by the localized methodology may in fact exist, and with higher-accuracy LiDAR surveys low-magnitude deposits may be indisputably identified. Researchers should consider supplementary estimates of surface representation uncertainty when estimating low-magnitude topographic change for study areas considerably smaller than county-wide LiDAR datasets.

¹⁴ Defined here as deposits less than 10cm in depth per event.

Section 2: Characterizing Floodplain Landforms

This study's characterization of floodplain topography hinted at the role landforms play in directing flow. Broad-scale ($>100\text{m}^2$) drainage networks formed of pronounced concave macro-topographic features were regularly identified along plausible flow routes expected to exist during flooding (Figure 3.5, grid cell B2). These results were corroborated by flow routes observed in the hydraulic model. Likewise, convex macro-topography (e.g. levees) were regularly identified adjacent to the Patapsco main channel; these aligned with field observations of levee features thought to influence overbanking events during storms (e.g., Gergel et al., 2002).

Landforms were effectively negligible when explaining spatial patterns of sediment texture, as shown by multivariate regression tree analyses. The all-inclusive regression tree only selected landforms for a single, tertiary node. This nodal split was also logically nonsensical, featuring the group "hollows, slopes, and spurs" on one branch and "ridges, summits, and valleys" on the other (Figure 3.17). When landforms were removed from the full explanatory variables set, only the regression tree predicting clay sediment texture proportions was affected; it saw a marginal 2% decrease in percent variation explained (Table 3.2). To summarize, *qualitative* interpretations of landform characterization bolstered evidence of hypothesized flow routes later observed in the hydraulic model; flow routes suggested by the literature (Hupp & Osterkamp, 1985; Gergel et al., 2002; Song et al., 2014) to be important for predicting floodplain particle size distribution. In contrast, *quantitative* assessments

of landform characterization via multivariate regression analysis showed little to no evidence of a relationship between landforms and sediment texture. This suggests that the utility of landforms as classified here is context-dependent in a way not represented by the regression tree models used. Alternatively, these results suggest that landforms, as characterized by aerial LiDAR, are most useful when utilized qualitatively to analyze floodplain topography.

Landforms, as discussed in the introduction, historically have been surrogates for qualitatively assessing theorized flow conditions (Bishop et al., 2012). When included in predictive models that also featured simulated flow conditions as explanatory variables, the more direct approximator (flow conditions) may have been logically selected over the less direct (landforms). As Hupp & Osterkamp (1985) stated, "...it is the hydrogeomorphic processes operating differently on the landforms that actually affect plant patterns [as stated earlier a result of a sediment deposit's texture, nutrient content, and deposit depth], **not the landforms themselves.**¹⁵". As their *localized* effect on hydraulic conditions varies spatiotemporally during a flood event as observed within the hydraulic model, this seems likely. This study suggests further research is needed at fine scales (<10m²) to identify relationships between floodplain particle size distribution and landform characterization.

¹⁵ Boldness added for emphasis

Section 3: Modeling Representative Flow Conditions on the Floodplain

By utilizing a high-resolution floodplain topography, more detailed information on spatiotemporal variation in flow routing throughout a storm was provided relative to similar studies using lower-resolution terrain (Woltemade & Potter, 1994; Gergel et al., 2002; Shelly et al., 2015). Qualitative evidence from the hydraulic model strongly suggested that both macro- and micro-topography play major roles in directing floodwaters at all periods of flooding; further evidence from the model suggested the relative importance of macro- and micro-topography in influencing flow patterns changes throughout a storm's hydrograph.

During the rising limb both macro- and micro-topography played significant roles in the flood model. Macro-topography, especially broad convex topography near the main channel (i.e. levees), governed where simulated floodwaters first entered the floodplain during backfilling, overbanking, and splaying periods. Micro-topography consequently controlled what fine-scale directions floodwaters took upon entering the floodplain interior and decreasing in velocity. As the storm progressed into peak flow conditions, micro-topography's influence on flow directionality waned. Instead, macro-topography was observed directing flow down the same concave networks (now recognized as ephemeral drainage networks) identified in the landform characterization analysis.

During the falling limb micro-topography's influence on flow directionality increased again. Micro-topography governed much of the fine-scale (<10m²) flow direction changes of slowly draining waters. Both micro- and macro-topography restricted where modeled floodwaters pooled during drainage periods as well, e.g. the standing water confined between the bisecting tributary and the pipeline road on the downstream section (Figure 3.11, grid cells E4 & E5). Macro-topography also constrained where floodwaters could drain off the floodplain, lengthening flow travel times in many cases. Qualitatively, floodplain topography's role in influencing flow directionality (and consequently flow length) at both fine and broad scales was clearly observed in the hydraulic model.

The quantitative relationship between flow conditions and sediment texture was also clearly established by this study. Flow velocity and shear stress at various periods moderately-to-strongly correlated with floodplain sediment texture spatial patterns during multivariate regression tree analysis. The all-inclusive regression tree series regularly selected for flow conditions during drainage periods and explained large amounts of sediment texture spatial variation. When regression trees were generated from an explanatory variable set of just flow-related variables, similar degrees of predictivity were observed.

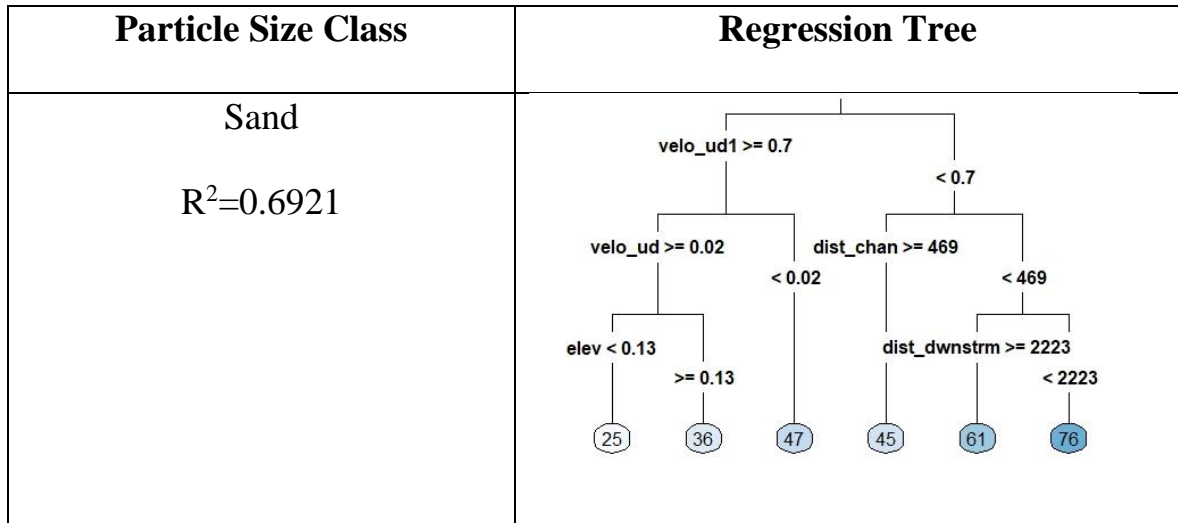


Figure 4.6: Regression tree predicting sand proportions in sediment samples, generated from the all-inclusive explanatory variable regression tree design set. For explanations on what variable each abbreviation references, refer to Table 3.1. Trees predicting clay and silt proportions explained approximately 59% and 69% of spatial variation for their respective sediment size classes.

Flow conditions during the drainage periods were selected for in regression trees at higher frequencies than others; similarly, flow conditions during these same periods regularly explained moderate to substantial amounts of variation when used to predict sediment texture patterns univariately. As such, I hypothesize that flow conditions during drainage periods were considered relatively more important than other periods of flooding for two likely-overlapping reasons. The first is that floodwaters are found in some areas of the floodplain but not others. This may lead to a “split” in the dataset that regression tree algorithms identify as a prime candidate for a nodal split (i.e. a regression tree “logic gate”). The second is that these periods may be geomorphically

important flood stages; drainage time periods may directly correlate with depositional processes, particularly for finer particles such as silts or clays.

Floodwaters during drainage periods are either slowly moving or virtually stagnant. Floodwaters need to be effectively stagnant for at least a 4-6-hour period for silts to settle out of suspension, and longer for clays (Marriott, 1992; Asselman & Middelkoop, 1995). Areas with longer drainage flow routes, or water ponded in topographic depressions such as those identified by the landform characterization, should in theory see increased silt and clay proportions. Both flow conditions were observed in the floodplain interior during the later flooding stages (Figure 3.10 & 3.11). Patterns confirming this theory were observed in the ternary plot and interpolation results, and correlate with spatial patterns identified in the literature (Marriott, 1992; Asselman & Middelkoop, 1995).

The hydraulic flow model was not without its faults. The land cover dataset that was used to approximate Manning's N values across the floodplain was a coarse approximation of actual roughness conditions. Given the much-criticized sensitivity of HEC-RAS's resistance equation in the literature (Pappenberger et al., 2005; Parhi et al., 2012; Parhi, 2013; Song et al., 2017), this dataset may have been insufficiently detailed. Future studies of similar natures should strive to incorporate a more advanced, higher-resolution land cover dataset before considering hydraulic modeling.

Section 4: Assessing the Relative Importance of Hydrogeomorphic, Topographic, and Geometric Conditions in Explaining Spatial Patterns of Floodplain Sediment Texture

The spatial arrangement and magnitude of sediment deposition from a single flooding event, identified from LiDAR topographic differencing, proved to be a poor predictor of floodplain particle size distribution. Similarly, landform characterization accounted for little in terms of explaining particle size distribution. In contrast, flow-related explanatory variables during both drainage periods, particularly velocity, exhibited moderate-to-strong predictive capabilities of floodplain sediment texture patterns. This was observed in the multivariate regression tree analyses, variable importance plots, and correlation matrix (Figure 5.1). Similar results were observed for distance-related explanatory variables, specifically distance from the Patapsco's main channel.

Distance-related and flow-related explanatory variables were regularly utilized nearly interchangeably in primary and secondary regression tree nodes. It may be possible that they function as the primary and secondary drivers of sediment texture spatial patterns at single-floodplain scales. This correlates with existing literature relating distance from the main channel to sediment texture spatial patterns (Marriot 1992; Asselman & Middelkoop, 1995) and literature relating flow hydraulics to sediment texture spatial patterns (Nicholas & Walling, 1997; Nicholas & Walling, 1998).

Marriott (1992) identified nearly identical spatial patterns of sediment texture to this study's (Figure 4.7 & 4.8). Marriott also related such spatial patterns directly to

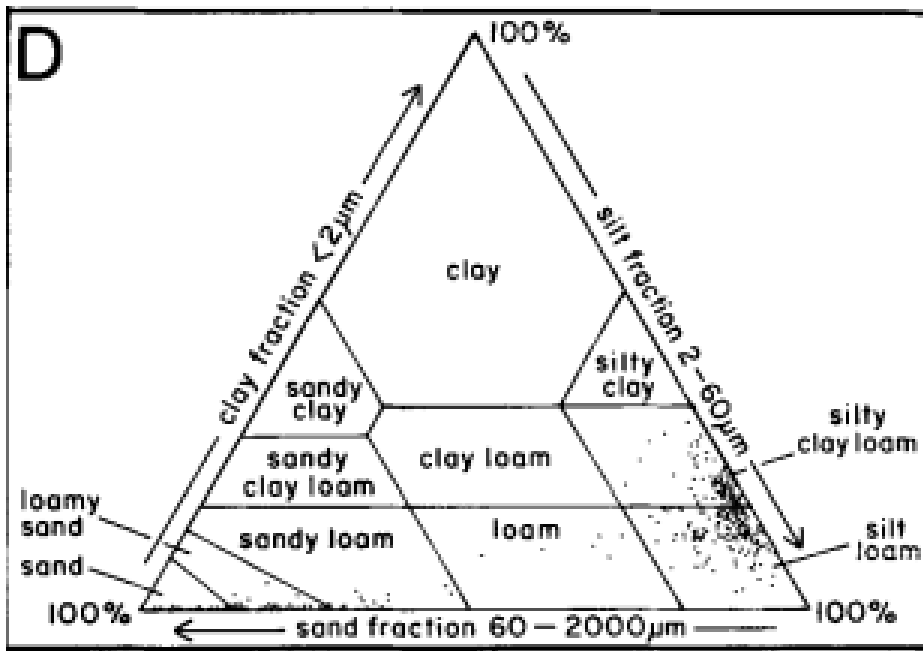
distance from the main channel via James' (1985) numerical model of sediment deposition. James' model, while intended to "simulate the transfer of suspended sediment from a channel to an adjacent floodplain under steady, uniform flow conditions", still predicted Marriott's spatial distribution of sediment texture at her study site. James' model predicted a sharp drop-off in sand proportion as one travels inland with Marriott's data, a trend mirrored in this study's regression analyses and spatial interpolations of sediment texture. This was confirmed by both the spatial interpolations of sediment texture, landform patterns, and the regression tree design set that excluded flow-related explanatory variables. When flow-related variables were excluded from said design the primary node across all sediment size classes was distance from the main channel, suggesting a strong reduction in internal group variance relative to the full dataset's internal variance.

Similarly, Nicholas & Walling's 1998 study documented similar relationships regarding distance from the main channel and sediment texture, but relative to flow hydraulic conditions modeled on the floodplain. While not modeling a storm hydrograph specifically as they utilized a steady-state hydraulic model, Nicholas and Walling nonetheless identified similar relationships between flow conditions and sediment texture as this study's. As flow exits the channel margins it slows down significantly, depositing coarser sediments, and areas where floodwaters are stored for long periods of time before draining feature finer sediments. Again, this was confirmed by the regression tree design set that excluded distance-related variables; when distance-related variables were excluded, the primary node across all sediment

size classes was flow velocity during the earlier drainage period, suggesting a strong reduction in internal group variance relative to the full dataset's internal variance.

To describe relatively simple hydrogeomorphic conditions on a floodplain with relation to particle size distributions, either flow or distance metrics will suffice as shown in previous studies within the literature (James, 1982; Harris, 1987; Marriott 1992; Asselman & Middelkoop, 1995; Nicholas & Walling, 1998; Barker et al, 2009).

To describe more complex conditions, this study strongly suggests researchers consider *both* flow- and distance-related explanatory variables when constructing their analyses.



Particle Size Analysis Results, Lower Patapsco Floodplain

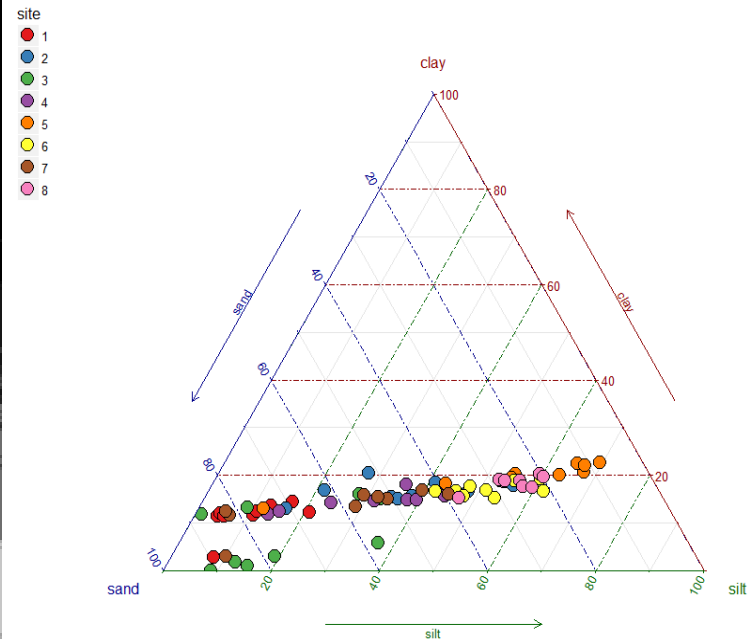


Figure 4.7 (left): Ternary diagram generated by Marriott (1992). Marriott observed a distinct fining gradient as one travels inland, comparable to this study's.

Figure 4.8 (right): Ternary plot of floodplain sediment texture across sites for this study. When compared to the spatial arrangement of sites in the site map (Figure 2.3) and the multivariate regression tree analysis results (Figure 3.17) a trend nearly identical to Marriott's was observed.

Chapter 5: Conclusions and Synthesis

High-resolution aerial LiDAR permitted this study to do a wide variety of topographic and hydrogeomorphic analyses and allowed high-accuracy predictions about sedimentological conditions on the floodplain in question. The purpose of this thesis was to explore what multi-temporal high-resolution aerial LiDAR offers researchers interested in predicting floodplain-scale sediment patterns; in that it succeeded. This study identified areas of significant sediment accretion as small as 2.5cm following a major storm event. This study discerned fine- and broad-scale floodplain landforms from LiDAR in a replicable, scale-, orientation-, and relief-independent manner. This study simulated high-resolution flow conditions during a major storm across the study floodplain. Finally, when paired with a targeted sampling of underlying sedimentology across a range of hydrogeomorphic and topographic conditions, this study successfully generated useful predictions of sediment texture patterns across the study floodplain.

This study's findings imply that flow conditions, namely velocity, across the floodplain during the falling limb (when flows are draining from the floodplain) are stronger predictors of floodplain sediment texture patterns. These findings are consistent with that of previous similar studies (e.g., Nicholas & Walling, 1998) but utilizing a more-representative, high-resolution topographic surface and a more advanced hydraulic model. Further findings imply that distance from the main channel is also a strong predictor of floodplain sediment texture patterns, again

confirming the findings of previous similar studies (Marriott, 1992; Steiger & Gurnell, 2002). Finally, our findings indicate that to comprehensively model complex hydrogeomorphic interactions when predicting floodplain sediment texture, it is necessary to account for both hydrodynamic flow conditions *and* geometric measures.

Concurrent with this study, newer technologies that map topography at even higher resolutions than aerial LiDAR have begun to receive attention and in some cases adoption by federal agencies and the private sector. Many of these technologies, such as terrestrial LiDAR and Structure from Motion (SfM) photogrammetry, offer resolutions an order of magnitude finer than the best aerial LiDAR offers (Mancini et al., 2013; Bangen et al., 2014; Lucieer et al., 2014). In many cases, they also lack many of the issues with vertical accuracy presented by the older aerial LiDAR datasets utilized in this study. Future research should consider the adoption or integration of newer technologies to mitigate some of the technical issues this research faced. The results of this investigation confirm the findings of several historical studies of floodplain sediment dynamics by utilizing a wide variety of study approaches, augmented by high-resolution aerial LiDAR. In so doing, this study has advanced the collective understanding of floodplain sediment dynamics within the context of short-term and long-term interactions among floodplain topography, storm events, and underlying sedimentology. However, it is limited in its scope to describing conditions specific to the lower Patapsco floodplain; future research should consider its applicability to other floodplains undergoing different hydrogeomorphic conditions.

Appendices

Table 5.1: HEC-RAS model times where flow-related variables were exported for use in regression analyses.

Stage of Flood	Upstream Floodplain Time Selected For	Downstream Floodplain Time Selected For
Overbanking	12:08, Sept. 7th 2011	12:08, Sept. 7th 2011
Backfilling	12:00, Sept. 7th 2011	N/A (no backfilling identified)
Splaying	12:12, Sept. 7th 2011	12:16, Sept. 7th 2011
Peak Flow	14:40, Sept. 7th 2011	15:56, Sept. 7th 2011
(Earlier) Drainage Period	13:28, Sept. 8th 2011	15:32, Sept. 8th 2011
(Later) Drainage Period	16:36, Sept. 8th 2011	18:12, Sept. 8th 2011

Table 5.2: Tabulation of the percent variation of floodplain sediment texture spatial variation explained by each numeric explanatory variable univariate relationship assessed. Linear or logarithmic regressions relating each explanatory variable to sediment texture were tested, and the strongest regression type is listed in the rightmost column. Note: the backfilling conceptual period was not assessed due to a lack of flooding for the vast majority of sites sampled for sediment texture, thus is marked “N/A”.

% Variation Explained (R²)	Sand	Silt	Clay	regression type (left to right)
Hydrologic Conditions: Velocity				
Backfilling	N/A	N/A	N/A	N/A
Overbanking	75.2%	14.1%	39.9%	log/linear/log
Splaying	88.0%	83.0%	91.0%	logarithmic
Peak Flow	3.8%	0.7%	26%	linear
(Earlier) Drainage Period	39.3%	50.1%	28.0%	linear
(Later) Drainage Period	60.1%	60.1%	43.0%	logarithmic
Hydrologic Conditions: Shear Stress				
Backfilling	N/A	N/A	N/A	N/A
Overbanking	7.0%	7.0%	0.8%	linear
Splaying	65.8%	62.1%	68.0%	linear
Peak Flow	16.0%	9.0%	49.0%	linear
(Earlier) Drainage Period	0.9%	1.6%	4.7%	linear
(Later) Drainage Period	3.7%	6.0%	7.0%	linear
Geometric Conditions				
Distance from Channel	31.2%	26.3%	47.1%	logarithmic
Distance Downstream	31.4%	36.6%	6.0%	linear
Sediment Accretion				
Change in Elevation	31.2%	48.9%	25.2%	logarithmic

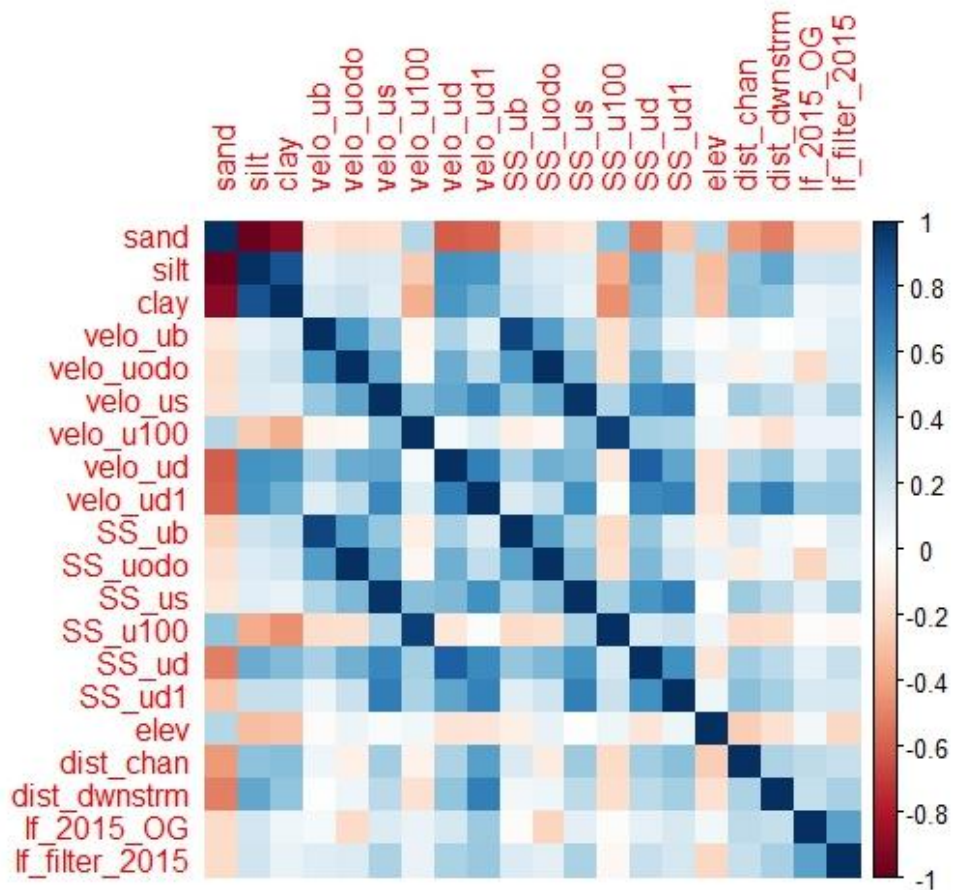


Figure 5.1: Matrix of Spearman's rho rank correlation coefficient values for all explanatory variables. For explanations on what variable each abbreviation references, refer to Table 3.1.

Variable Importance Plot, Silt

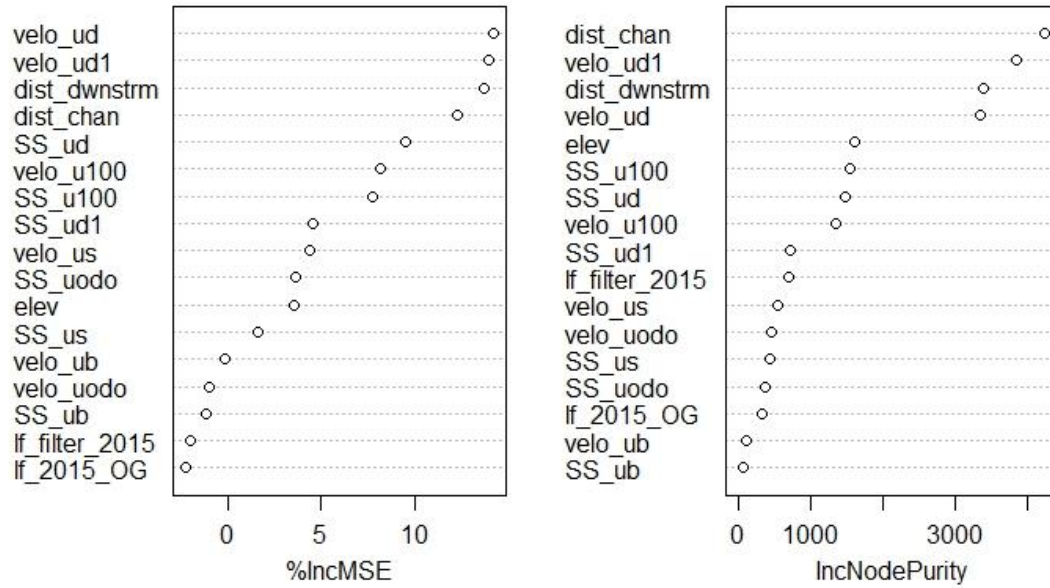


Figure 5.2: Silt variable importance plot generated from a randomforest regression tree algorithm.

Variable Importance Plot, Clay

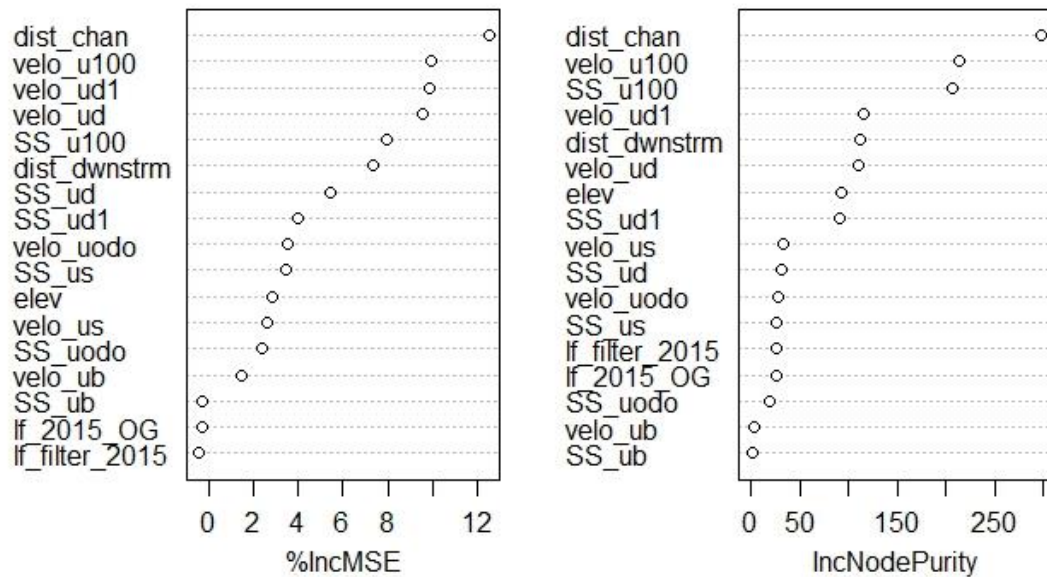


Figure 5.3: Clay variable importance plot generated from a random forest regression tree algorithm.

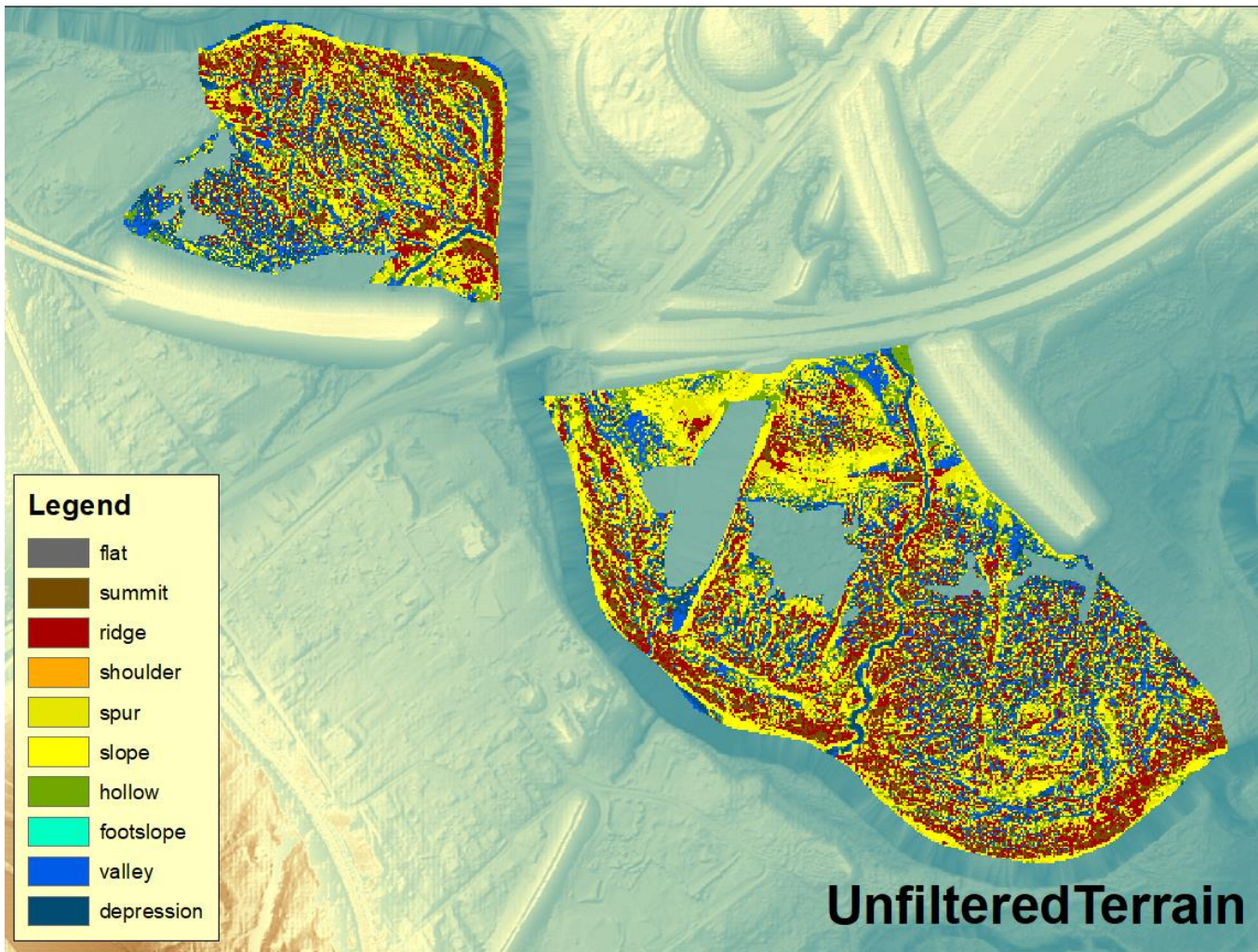


Figure 5.4: Landform Characterization results from unfiltered terrain.

Bibliography

- Asselman, N. E., & Middelkoop, H. (1995). Floodplain sedimentation: quantities, patterns and processes. *Earth Surface Processes and Landforms*, 20(6), 481-499.
- Bangen, S. G., Wheaton, J. M., Bouwes, N., Bouwes, B., & Jordan, C. (2014). A methodological intercomparison of topographic survey techniques for characterizing wadeable streams and rivers. *Geomorphology*, 206, 343-361.
- Barker, D. M., Lawler, D. M., Knight, D. W., Morris, D. G., Davies, H. N., & Stewart, E. J. (2009). Longitudinal distributions of river flood power: the combined automated flood, elevation and stream power (CAFES) methodology. *Earth Surface Processes and Landforms*, 34(2), 280-290.
- Bishop, M. P., James, L. A., Shroder Jr, J. F., & Walsh, S. J. (2012). Geospatial technologies and digital geomorphological mapping: concepts, issues and research. *Geomorphology*, 137(1), 5-26.
- Bouyoucos, G. J. (1951). A Recalibration of the Hydrometer Method for Making Mechanical Analysis of Soils 1. *Agronomy journal*, 43(9), 434-438.
- Carling, P. A. (1987). Bed stability in gravel streams, with reference to stream regulation and ecology. *River channels: environment and process*, 17.
- Carson, E. C. (2006). Hydrologic modeling of flood conveyance and impacts of historic overbank sedimentation on West Fork Black's Fork, Uinta Mountains, northeastern Utah, USA. *Geomorphology*, 75(3-4), 368-383.
- Ernst, J., Dewals, B. J., Detrembleur, S., Archambeau, P., Erpicum, S., & Pirotton, M. (2010). Micro-scale flood risk analysis based on detailed 2D hydraulic modelling and high resolution geographic data. *Natural Hazards*, 55(2), 181-209.
- Fabricius, K. E. (2005). Effects of terrestrial runoff on the ecology of corals and coral reefs: review and synthesis. *Marine pollution bulletin*, 50(2), 125-146.
- Gareth, J., Witten, D., Hastie, T., & Tibshirani, R. (2017). *An introduction to statistical learning with applications in R*. New York: Springer.

- Gellis, A. C., Hupp, C. R., Pavich, M. J., Landwehr, J. M., Banks, W. S., Hubbard, B. E., ... & Reuter, J. M. (2009). Sources, transport, and storage of sediment at selected sites in the Chesapeake Bay Watershed. U. S. Geological Survey.
- Gergel, S. E., Dixon, M. D., & Turner, M. G. (2002). CONSEQUENCES OF HUMAN-ALTERED FLOODS: LEVEES, FLOODS, AND FLOODPLAIN FORESTS ALONG THE WISCONSIN RIVER. *Ecological applications*, 12(6), 1755-1770.
- Gurnell, A. M., Bertoldi, W., & Corenblit, D. (2012). Changing river channels: The roles of hydrological processes, plants and pioneer fluvial landforms in humid temperate, mixed load, gravel bed rivers. *Earth-Science Reviews*, 111(1-2), 129-141.
- Hack, J. T. (1982). Physiographic divisions and differential uplift in the Piedmont and Blue Ridge (No. 1265). USGPO,.
- Halverson, J. (2018, May 28). The second 1,000-year rainstorm in two years engulfed Ellicott City. Here's how it happened. *The Washington Post*. Retrieved from https://www.washingtonpost.com/news/capital-weather-gang/wp/2018/05/28/the-second-1000-year-rainstorm-in-two-years-engulfed-ellicott-city-heres-how-it-happened/?utm_term=.ab809f3762aa
- Hamilton, Nicholas (2017). ggtern: An Extension to 'ggplot2', for the Creation of Ternary Diagrams. R package version 2.2.1.
- Harris, R. R. (1987). Occurrence of vegetation on geomorphic surfaces in the active floodplain of a California alluvial stream. *American Midland Naturalist*, 393-405.
- Hilldale, R. C., & Raff, D. (2008). Assessing the ability of airborne LiDAR to map river bathymetry. *Earth Surface Processes and Landforms*, 33(5), 773-783.
- Homer, C.G., Dewitz, J.A., Yang, L., Jin, S., Danielson, P., Xian, G., Coulston, J., Herold, N.D., Wickham, J.D., and Megown, K., 2015, Completion of the 2011 National Land Cover Database for the conterminous United States-Representing a decade of land cover change information. *Photogrammetric Engineering and Remote Sensing*, v. 81, no. 5, p. 345-354
- Howarth, R. W., Fruci, J. R., & Sherman, D. (1991). Inputs of sediment and carbon to an estuarine ecosystem: influence of land use. *Ecological applications*, 1(1), 27-39.
- Hupp, C. R. (1982). Stream-grade variation and riparian-forest ecology along Passage Creek, Virginia. *Bulletin of the Torrey Botanical Club*, 488-499.

- Hupp, C. R., & Osterkamp, W. R. (1985). Bottomland vegetation distribution along Passage Creek, Virginia, in relation to fluvial landforms. *Ecology*, 66(3), 670-681.
- Hupp, C. R., & Morris, E. E. (1990). A dendrogeomorphic approach to measurement of sedimentation in a forested wetland, Black Swamp, Arkansas. *Wetlands*, 10(1), 107-124.
- Hupp, C. R., Pierce, A. R., & Noe, G. B. (2009). Floodplain geomorphic processes and environmental impacts of human alteration along coastal plain rivers, USA. *Wetlands*, 29(2), 413-429.
- Hupp, C. R., Noe, G. B., Schenk, E. R., & Benthem, A. J. (2013). Recent and historic sediment dynamics along Difficult Run, a suburban Virginia Piedmont stream. *Geomorphology*, 180, 156-169.
- Hutton, C., & Brazier, R. (2012). Quantifying riparian zone structure from airborne LiDAR: Vegetation filtering, anisotropic interpolation, and uncertainty propagation. *Journal of hydrology*, 442, 36-45.
- James, C. S. (1985). Sediment transfer to overbank sections. *Journal of hydraulic research*, 23(5), 435-452.
- Jasiewicz, J., & Stepinski, T. F. (2013). Geomorphons—a pattern recognition approach to classification and mapping of landforms. *Geomorphology*, 182, 147-156.
- Julesz, B. (1981). Textons, the elements of texture perception, and their interactions. *Nature*, 290(5802), 91.
- Kleiss, B. A. (1993). Methods for measuring sedimentation rates in bottomland hardwood (BLH) wetlands. US Army Engineer Waterways Experiment Station.
- Knighton, D. (2014). *Fluvial forms and processes: a new perspective*. Routledge.
- Kochel, R. C., Hayes, B. R., Muhlbauer, J., Hancock, Z., & Rockwell, D. (2016). Geomorphic response to catastrophic flooding in north-central Pennsylvania from Tropical Storm Lee (September 2011): Intersection of fluvial disequilibrium and the legacy of logging. *Geosphere*, 12(1), 305-345.
- Layzer, J. (2002). Ecosystem-Based Management in the Chesapeake Bay. In *The Environmental Case: Translating Values into Policy* (pp. 450-51; 476-77). Washington, D.C.
- Leopold, L. B., Wolman, M. G., & Miller, J. P. (1964). *Fluvial processes in geomorphology*. San Francisco, California, Freeman, 522, 135-163.

- Loh, W. Y. (2011). Classification and regression trees. *Wiley Interdisciplinary Reviews: Data Mining and Knowledge Discovery*, 1(1), 14-23.
- Lucieer, A., Jong, S. M. D., & Turner, D. (2014). Mapping landslide displacements using Structure from Motion (SfM) and image correlation of multi-temporal UAV photography. *Progress in Physical Geography*, 38(1), 97-116.
- Mancini, F., Dubbini, M., Gattelli, M., Stecchi, F., Fabbri, S., & Gabbianelli, G. (2013). Using unmanned aerial vehicles (UAV) for high-resolution reconstruction of topography: The structure from motion approach on coastal environments. *Remote Sensing*, 5(12), 6880-6898.
- Marriott, S. (1992). Textural analysis and modelling of a flood deposit: River Severn, UK. *Earth Surface Processes and Landforms*, 17(7), 687-697.
- Marston, R. A., Girel, J., Pautou, G., Piegay, H., Bravard, J. P., & Arneson, C. (1995). Channel metamorphosis, floodplain disturbance, and vegetation development: Ain River, France. In *Biogeomorphology, Terrestrial and Freshwater Systems* (pp. 121-131).
- Matonse, A. H., & Frei, A. (2013). A seasonal shift in the frequency of extreme hydrological events in southern New York State. *Journal of Climate*, 26(23), 9577-9593.
- MD Dept. of the Environment. (2018). Map of Maryland's 8-Digit Watersheds. Retrieved November 16, 2018, from <http://www.mde.state.md.us/programs/water/tmdl/datacenter/pages/8digitwatershed.aspx>
- MD iMAP (2016). "LiDAR Metadata." MD iMAP | LiDAR Metadata, Maryland iMAP, imap.maryland.gov/Pages/lidar-metadata.aspx.
- Milan, D. J. (2012). Geomorphic impact and system recovery following an extreme flood in an upland stream: Thinhope Burn, northern England, UK. *Geomorphology*, 138(1), 319-328.
- Miller, A. J. (1994). Debris-fan constrictions and flood hydraulics in river canyons: Some implications from two-dimensional flow modelling. *Earth Surface Processes and Landforms*, 19(8), 681-697.
- Minnesota Department of Natural Resources. (2016). "Eastern Broadleaf Forest Province, Floodplain Forest System Summary." *Ecological System Summaries and Class Factsheets – Wetland Forests*, www.dnr.state.mn.us/npc/wetforest.html.
- Mueller, D. K., Helsel, D. R., & Kidd, M. A. (1996). *Nutrients in the nation's waters: too much of a good thing?*. US Government Printing Office.

- Neuman, Y., & Cohen, Y. (2014). A vectorial semantics approach to personality assessment. *Scientific reports*, 4, 4761.
- Nicholas, A. P., & Walling, D. E. (1997). Modelling flood hydraulics and overbank deposition on river floodplains. *Earth Surface Processes and Landforms: The Journal of the British Geomorphological Group*, 22(1), 59-77.
- Nicholas, A. P., & Walling, D. E. (1998). Numerical modelling of floodplain hydraulics and suspended sediment transport and deposition. *Hydrological Processes*, 12(8), 1339-1355.
- Noe, G. B., & Hupp, C. R. (2005). Carbon, nitrogen, and phosphorus accumulation in floodplains of Atlantic Coastal Plain rivers, USA. *Ecological Applications*, 15(4), 1178-1190.
- Noe, G. B., & Hupp, C. R. (2009). Retention of riverine sediment and nutrient loads by coastal plain floodplains. *Ecosystems*, 12(5), 728-746.
- Osterkamp, W. R., & Hupp, C. R. (1984). Geomorphic and vegetative characteristics along three northern Virginia streams. *Geological Society of America Bulletin*, 95(9), 1093-1101.
- Pappenberger, F., Beven, K., Horritt, M., & Blazkova, S. (2005). Uncertainty in the calibration of effective roughness parameters in HEC-RAS using inundation and downstream level observations. *Journal of Hydrology*, 302(1-4), 46-69.
- Parhi, P. K., Sankhua, R. N., & Roy, G. P. (2012). Calibration of channel roughness for Mahanadi River,(India) using HEC-RAS model. *Journal of Water Resource and Protection*, 4(10), 847.
- Parhi, P. K. (2013). HEC-RAS Model for Manning's Roughness: A Case Study. *Open Journal of Modern Hydrology*, 3(03), 97.
- Pennock, D. J., & De Jong, E. (1987). The influence of slope curvature on soil erosion and deposition in hummock terrain. *Soil Science*, 144(3), 209-217.
- Phillips, J. V., & Tadayon, S. (2006). Selection of Manning's roughness coefficient for natural and constructed vegetated and non-vegetated channels, and vegetation maintenance plan guidelines for vegetated channels in Central Arizona. US Department of the Interior, US Geological Survey.
- Pizzuto, J., Schenk, E. R., Hupp, C. R., Gellis, A., Noe, G., Williamson, E., ... & Newbold, D. (2014). Characteristic length scales and time-averaged transport velocities of suspended sediment in the mid-Atlantic Region, USA. *Water Resources Research*, 50(2), 790-805.

- Poppe, L. J., Eliason, A. H., Fredericks, J. J., Rendigs, R. R., Blackwood, D., & Polloni, C. F. (2000). Grain size analysis of marine sediments: methodology and data processing. US Geological Survey East Coast sediment analysis: procedures, database, and georeferenced displays. US Geological Survey Open File Report 00-358. <http://pubs.usgs.gov/of/2000/of00-358>.
- Ritchie, J. C., & McHenry, J. R. (1990). Application of radioactive fallout cesium-137 for measuring soil erosion and sediment accumulation rates and patterns: a review. *Journal of environmental quality*, 19(2), 215-233.
- Schwartz, S. S., & Smith, B. (2016). Restoring hydrologic function in urban landscapes with suburban subsoiling. *Journal of Hydrology*, 543, 770-781.
- Scown, M. W., Thoms, M. C., & De Jager, N. R. (2015). An index of floodplain surface complexity. *Hydrology & Earth System Sciences Discussions*, 12(4).
- Sharp, H. K. (2001). *The Patapsco River Valley: Cradle of the Industrial Revolution in Maryland*. Maryland Historical Society.
- Shelley, J., Gibson, S., & Williams, A. (2015). Unsteady flow and sediment modeling in a large reservoir using HEC-RAS 5.0. In *Federal Interagency Sediment Conference*.
- Shokory, J. A. N., Tsutsumi, J. I. G., & Sakai, K. (2016). Flood modeling and simulation using iRIC: a case study of Kabul City. In *E3S web of conferences (Vol. 7, p. 04003)*. EDP Sciences.
- Snead, D. B., & Maidment, D. R. (2000). *Development and application of unsteady flood models using geographical information systems (Doctoral dissertation, Center for Research in Water Resources, University of Texas at Austin)*.
- Soil Survey Staff, Natural Resources Conservation Service, United States Department of Agriculture. *Web Soil Survey*. Available online. Accessed 11/15/2018.
- Song, S., Schmalz, B., & Fohrer, N. (2014). Simulation and comparison of stream power in-channel and on the floodplain in a German lowland area. *Journal of Hydrology and Hydromechanics*, 62(2), 133-144.
- Song, S., Schmalz, B., Xu, Y. P., & Fohrer, N. (2017). Seasonality of Roughness-the Indicator of Annual River Flow Resistance Condition in a Lowland Catchment. *Water Resources Management*, 31(11), 3299-3312.

- Sparks, R. E., & Spink, A. (1998). Disturbance, succession and ecosystem processes in rivers and estuaries: effects of extreme hydrologic events. *River Research and Applications*, 14(2), 155-159.
- Steiger, J., & Gurnell, A. M. (2003). Spatial hydrogeomorphological influences on sediment and nutrient deposition in riparian zones: observations from the Garonne River, France. *Geomorphology*, 49(1-2), 1-23.
- Stepinski, T. F., & Jasiewicz, J. (2011). Geomorphons—a new approach to classification of landforms. *Proceedings of Geomorphometry 2011*, 109-112.
- Sun, X., Rosin, P., Martin, R., & Langbein, F. (2007). Fast and effective feature-preserving mesh denoising. *IEEE transactions on visualization and computer graphics*, 13(5).
- Suro, T. P., Roland, M. A., & Kiah, R. G. (2015). *Flooding in the Northeastern United States, 2011* (No. 1821). US Geological Survey.
- Taylor, J. (1997). *Introduction to error analysis, the study of uncertainties in physical measurements*.
- Terrain 360. (2018). Patapsco River. Retrieved November 15, 2018, from <https://www.terrain360.com/map/patapsco-river/visual#10.38/39.2019/-76.5295>
- Thompson, C., & Croke, J. (2013). Geomorphic effects, flood power, and channel competence of a catastrophic flood in confined and unconfined reaches of the upper Lockyer valley, southeast Queensland, Australia. *Geomorphology*, 197, 156-169.
- Unger, I. M., & Muzika, R. M. (2008). Influence of microtopography on soil chemistry and understory riparian vegetation. In *Proceedings of the 16th Central Hardwoods Forest Conference GTR-NRS-P* (Vol. 24, p. 565).
- USACE [1], (2016). *HEC-RAS River Analysis System, Version 5.0, Hydrologic Engineering Center User Manual*. U.S. Army Corps of Engineers.
- USACE [2], (2016). *HEC-RAS River Analysis System, Version 5.0, HEC-RAS Hydraulic Reference Manual*. U.S. Army Corps of Engineers.
- US Climate Data. (2018). *Climate Maryland - Baltimore*. Retrieved November 15, 2018, from <https://www.usclimatedata.com/climate/maryland/united-states/1872>

Walls, R. L., Wardrop, D. H., & Brooks, R. P. (2005). The impact of experimental sedimentation and flooding on the growth and germination of floodplain trees. *Plant Ecology*, 176(2), 203-213.

Wheaton, J. M., Brasington, J., Darby, S. E., & Sear, D. A. (2010). Accounting for uncertainty in DEMs from repeat topographic surveys: improved sediment budgets. *Earth Surface Processes and Landforms*, 35(2), 136-156.

Wolman, M. G., & Miller, J. P. (1960). Magnitude and frequency of forces in geomorphic processes. *The Journal of Geology*, 68(1), 54-74.

Woltemade, C. J., & Potter, K. W. (1994). A watershed modeling analysis of fluvial geomorphologic influences on flood peak attenuation. *Water Resources Research*, 30(6), 1933-1942.

Yokoyama, R., Shirasawa, M., & Pike, R. J. (2002). Visualizing topography by openness: a new application of image processing to digital elevation models. *Photogrammetric engineering and remote sensing*, 68(3), 257-266.

